Chapter FF (Fluid Flow Modeling)

STRATIGRAPHIC, HYDROGEOLOGIC, AND THERMAL EVOLUTION OF THE CANNING RIVER REGION, NORTH SLOPE, ALASKA

by Daniel O. Hayba[1], David W. Houseknecht[1], and Elisabeth Rowan[2]

in The Oil and Gas Resource Potential of the 1002 Area, Arctic National Wildlife Refuge, Alaska, by ANWR Assessment Team, U. S. Geological Survey Open File Report 98-34.

1999

1 U.S. Geological Survey, MS 956, Reston, VA 20192
2 U.S. Geological Survey, MS 969, Menlo Park, CA 94025

TABLE OF CONTENTS

FIGURES

TABLES

ABSTRACT

Numerical modeling of the Canning River region provides an integrated analysis of the stratigraphic, thermal and fluid migration history along the western margin of the Arctic National Wildlife Refuge 1002 area. The 2-D model, which spans 160 km, incorporates the essential aspects of the sedimentary and tectonic evolution of the basin. The model also includes details about the primary lithologies and their matrix characteristics. We calibrated the fluid flow and thermal characteristics of the model against pressure and temperature data obtained from wells. The resulting model satisfactorily honors existing geologic, geophysical and geochemical data.

Pressure data show extensive geopressure zones offshore, but they are present only over a limited depth interval in the Point Thomson area and are nonexistent farther south. Modeling indicates that compaction of thick Brookian muds offshore began generating geopressures at about 37 Ma. Fluids driven southward out of these compacting sediments transmit geopressures into the Point Thomson area. Present geothermal gradients also differ across the region. In the Point Thomson and offshore wells, thermal gradients are fairly linear at about 32 °C/km. However in the south, advective heat flow causes steep gradients (~58 °C/km) directly beneath the permafrost, which give way to rather flat gradients (~23 °C/km) at greater depths. Modeling results match these thermal gradients when we use a heat flux value of 50 mW/m^2 and define an upper boundary that accounts for the permafrost. Predicted vitrinite reflectance profiles also agree with measured values, suggesting heat flow throughout the region has been relatively constant since at least 130 Ma.

The predicted maturation history for the likely source rocks within the Canning River section indicates that hydrocarbon generation began about 56 Ma in the Shublik Formation and about 50 Ma in the Hue Shale in the southern portion of the region. The level of maturity decreases to the north in both units to the point that they probably continue to generate oil at their respective northern extents. The youngest likely source rock, the Mikkelsen Tongue of the Canning Formation, is immature at least over its known extent from the Point Thomson area south. Any oil generated from this unit would have had to come from offshore, north of the Barrow Arch. Results of fluid migration modeling suggest that prior to about 24 Ma oil generated in the undeformed area of the ANWR 1002 area initially migrated northward toward the crest of the Mikkelsen high. Since that time, most migration has

been southward, driven by compaction offshore. This change in hydrodynamic drive may have caused oil previously trapped on the crest or flanks of the Mikkelsen high to remigrate southward. This scenario may explain the occurrence of "older", Hue-type oil in young traps.

INTRODUCTION

The Canning River region lies along the western margin of the Arctic National Wildlife Refuge (ANWR) 1002 area. Due to the absence of wells within ANWR, exploration wells in the Canning River region, along with additional wells offshore, provide much of the data used to assess the hydrocarbon potential of the 1002 area. As a part of this assessment, we developed an integrated model of the geologic, hydrologic, and thermal history of the Canning River region utilizing this well data. Our model predominantly covers the undeformed portion of the 1002 area, extending from just within the deformed zone in the south to approximately 80 km offshore in the north, for a total section length of 160 km.

In this paper, we present the results of numerical modeling of fluid flow and heat transfer during the stratigraphic evolution of the Canning River region. The main purpose of this model is to help evaluate the timing of oil generation and migration. We use a two-dimensional model to simulate the subsidence, sedimentation, compaction, uplift, erosion and thermal evolution of basin strata and the flow of fluids driven by compaction and topographic relief.

CANNING RIVER CROSS SECTION

Figure FF1 shows the location of the cross section used in our numerical model. This is the same location as the geologic section portrayed by Bird and Magoon (1987, Plate 1) and revised by Bird (Plate GG3). We relied on these geologic sections for stratigraphic control for the model, particularly for the units below the lower Cretaceous unconformity (LCU). For the younger units, we used the sequence stratigraphy developed by Houseknecht and Schenk (Chap. BS).

Along the length of the cross section, there are 10 wells, seven on land, one (Alaska State D-1) on Flaxman Island just off the coast, and two farther offshore. From south to north, these wells are (1) Canning River Unit A-1, (2) Canning River Unit B-1, (3) Beli Unit 1, (4) Alaska State J-1, (5) E De K

Leffingwell 1, (6) West Staines State 2, (7) Point Thomson 1, (8) Alaska State D-1 (9) Hammerhead 1, and (10) Galahad 1. Additional information used in this report also came from a number of other wells in the vicinity of the 1002 area (Fig. FF1). Wells from the southern Canning River area include Kavik 1, Kavik 3, Kemik 2, Fin Creek 1, and Gyr 1; wells in the general Point Thomson area include: Point Thomson 3, West Staines 18-9-23, Alaska State A-1, Badami 1, and East Mikkelsen Bay State 1; offshore wells include: Aurora 1, Kuvlum 1, Kuvlum 2, Belcher, and Corona 1.

Seismic sections also helped in determining stratigraphic relations in the offshore portion of the cross section. USGS public-domain seismic lines 724, 709, and 740 are located near the cross section (see Grantz and others 1994). There are also published industry lines in the vicinity (Craig and others, 1985; Scherr and others, 1991). The approximate locations of these seismic lines are shown on Figure FF1.

PREVIOUS MODELING WORK

In a previous study of the ANWR 1002 area, Yu and Lerche (1992) used a combination of 1-D and 2-D numerical models to examine the thermal and flow history along a portion of the Canning River section. They applied their 1-D model to the Canning River B-1 and Beli Unit 1 wells and developed a 2-D model for an 18-km section through 4 wells in the Point Thomson area. Our work differs from theirs in that the cross section we examine extends 160 km, from the deformed region in the south to 80 km offshore. This extended section allows us to better model the development of geopressures (*i.e.*, pressures significantly greater than hydrostatic), which is one of the areas in which our results differ significantly from theirs. The simulations of Yu and Lerche (1992) predicted that sedimentation was sufficiently rapid and fine-grained at Point Thomson to generate geopressures, whereas our model indicates that significant geopressures only developed offshore and that fluids migrating southward up the north flank of the Barrow arch transmitted geopressures into the Point Thomson area. Our results also differ in our estimates of the current heat flux into the basin. Yu and Lerche (1992) estimate fluxes of about 66 mW/m^2 in the Canning River B-1 and Beli wells and about 41-45 mW/m^2 in the Point Thomson area, whereas we estimate heat fluxes of about 50 mW/m^2 throughout the entire Canning River section.

Another previous study relevant to the ANWR 1002 area is the heat flow work of Deming and others (1992) in the National Petroleum Reserve --

Alaska (NPRA). In that study, they proposed that topographically driven ground water flow advectively transports heat from the south in the foothills of the Brooks Range to the north along the coast. They developed an analytical model of this scenario and determine that effective basin-scale permeability must be on the order of 10^{-14} m^2 (10 md) for their conceptual model to work. In addition, they inferred that the flow system extends to depths of 10,000 - 20,000 ft below sea level. Although a similar flow system would appear to be a reasonable situation for the Canning River region, our numerical modeling indicates that topographically driven flow to the north only reaches depths of about 5,000 ft below sea level. At greater depths, flow is dominantly driven to the south by compaction of the thick muds being deposited offshore.

Rowan (1997, Chap. BE) also numerically modeled the stratigraphic, tectonic, and thermal evolution of the Canning River region. In a preliminary study, she examined the thermal history and source rock maturation of the region assuming a conductive thermal regime and hydrostatic pressures (*i.e.*, conductive heat transport without thermal perturbations due to fluid flow). The present study builds on and augments Rowan's numerical modeling work in a number of important ways. First, we expand the cross-section from 90 to 160 km and include data from several additional wells. Second, we incorporate the thermal effects of permafrost. Third, our simulations include groundwater flow and its effects on the temperature and pressure regimes. These additions allow our model to address the development of geopressures observed in the Point Thomson and offshore wells. Rowan and others (1998) also investigated overpressures and topographically driven flow, but did not calibrate the model using the detailed surface and bottom-hole temperature data included in the present study.

BASIN2 NUMERICAL SIMULATION PROGRAM

Description of Basin2

We simulated the geologic, hydrologic, and thermal evolution of the Canning River region with the computer program Basin2 (Bethke 1985; Bethke 1989; Corbet and Bethke, 1992; Bethke and others, 1993). Basin2 calculates in two-dimensions the groundwater flow within evolving sedimentary basins due to sediment compaction, buoyancy, and topographic relief as well as the transport of heat and the thermal maturation of petroleum source rocks. The program solves finite difference

approximations to coupled partial differential equations describing continuity of the medium, fluid flow, and heat transfer. The program can also account for the transport of dissolved mass and its effect on groundwater salinity, but here we assume a groundwater of constant concentration of 0.5 molal NaCl (~3 wt.%). Bethke (1985) described the formulation of equations and the numerical procedure for solving them. For the purposes of this paper, we include an overview of the conceptual basis of our model.

As with any initial-boundary value problem, values for the unknown variables (in this case the distribution of pressure and temperature) must be specified (1) over the domain at the beginning of the simulation and (2) along the boundaries of the domain over the course of the simulation. In addition to the initial and boundary conditions, the simulation requires information on the amount, type, and physical and hydrologic properties of the sediments filling the basin through time.

The domain changes in size at each step in the simulation as sediment accumulates along the depositional surface or is removed by erosion. During deposition, the increasing weight of the sediment pile causes sediments to compact. Settling (*i.e.*, compaction) velocity of the sediments, which is greatest at the top of the pile, is at any point in the cross-section the sum of the rate of basement subsidence or uplift and the velocity contributed by the compaction of underlying sediments. During erosion, the loss of overburden allows the sediments to rebound somewhat; we assume that rebounding sediments may regain up to 10 - 20 % of the porosity that they lost during compaction.

Basin2 determines the compaction rate from the change in stress on sediment at each point in the cross-section, using empirical functions relating porosity to effective depth. Effective depth, Z_E, is burial depth corrected for deviation of fluid pressure from hydrostatic; it is proportional to effective stress, as commonly employed in rock mechanics. As the sediment compacts, Basin2 recalculates the permeability and thermal conductivity of the medium, again using empirical correlations. Table FF1 shows the forms of the empirical correlations used in Basin2 to determine for each rock type the porosity, permeability, and thermal conductivity. As suggested by Bethke and others (1993), we modified the Basin2 default correlations that were developed and used in studies of interior basins in

North America. Our choice of parameters for the empirical correlations will be justified below.

Having determined the rate of compaction and estimated the permeability across the domain, Basin2 calculates the distribution of fluid pressure, and the rates and directions of fluid migration. The program, given a surface temperature and basal heat flow, next solves a heat transfer equation that accounts for conduction and groundwater advection. The solution gives the distribution of temperature over the cross-section. Using the temperature distribution, the program determines the extent to which petroleum source rocks have matured over the time step using the Arrhenius method. At this point, the program returns to make a new time step. It continues to march through time in this manner until it reaches the end of the simulation.

Limitations to the Model

Although Basin2 is a state-of-the-art program for modeling the evolution of sedimentary basins, there are two aspects of the Canning River section that are difficult to simulate with this software. First, it is not possible in Basin2 to include the growth faults that occur in the northern, offshore portion of our model, nor the thrust faults in the deformed area to the south. In the northern offshore portion of our model, Tertiary growth faults certainly contributed to the increase in sediment thickness. Although we have not been able to include the displacement along these faults in our modeling, we have incorporated accurately the thickness of the sediment pile. The thrust faults in the deformed area pose a greater problem to the model. We specifically chose to model primarily the undeformed portion of the 1002 area by placing the southern boundary of the model just south of the Canning River A-1 well. However, by excluding most of the deformed portion of the basin, our model ignores the effects that basinal shortening and thickening had on the hydrology of the undeformed portion. The reconstructed section by Cole and others (Chap. SM) illustrates the extent to which thrust faults contributed to the evolution of the basin. Also, because topographic relief increases to the south, this boundary influences the model by limiting the topographic drive for fluid flow during the later stages of the simulation. We address these limitations in the discussion of the model results.

The other significant limitation of Basin2, in terms of the Canning River model, is its inability to handle temperatures less than 0.5 °C. This of course

made it impossible, *per se*, to simulate the development of permafrost within the last 1 - 2 m.y. However, we were able to work around this limitation and mimic the thermal and hydrologic effects of permafrost by treating it as a separate stratigraphic horizon with special lithologic properties. The procedure we employed was to assume that the stratigraphic section has not changed (except for the addition of permafrost) in the last 1.0 m.y. We simulated the development of permafrost at that time by rapidly removing (by erosion) the thickness of sediment that corresponds to the present thickness of permafrost, and then replacing it by the "deposition" of the "permafrost unit". For modeling purposes, the important characteristics of this unit are 1) high thermal conductivity, 2) very low permeability, and 3) compaction and density characteristics similar to the sediment that it replaced. We also set the temperature along the surface to 0.5 °C, which, combined with the high thermal conductivity, forced the model to hold temperatures close to freezing along the base of the permafrost. This approach worked quite satisfactorily and allowed us to calibrate the model using down-hole temperature data from the base of the permafrost and below.

Lastly, it is only possible to simulate two-dimensional models with this software. For the Canning River section, this is adequate for most of our purposes, but it is important to remember when analyzing fluid migration paths.

NUMERICAL MODEL SET UP

Grid and Time Frame

The numerical model represents a two-dimensional cross-section 100 miles (160 km) long with a maximum thickness of 38,000 ft (11.5 km). There are 50 nodes in the X direction, each with a length of 2 miles (3.2 km). In the vertical direction, there are initially only 2 nodes representing a 2000-foot thick continuous section of pre-Mississippian basement rocks. The number of nodes increases as the simulation progresses to accommodate the deposition of additional sediment. The thicknesses of the nodes varies in time and space in relation to the thickness of the stratigraphic unit; however, the maximum thickness of any node is approximately 1,300 ft (400 m). When the thickness of a unit exceeds this value the model adds an additional row of nodes.

The model spans the time period of 355 Ma to the present. We have divided this time into 19 intervals, with each interval related to the deposition and (or) erosion of a time-stratigraphic unit (Table FF2). The pre-Mississippian basement rocks are the first time-stratigraphic unit in the model. This unit is present at the beginning of the model with specified initial conditions for pressure and temperature (as discussed below). The transient simulation begins with the deposition of Endicott sediments onto the basement. The last "unit" in the simulation is the formation of the permafrost. We discuss the evolution of the stratigraphy in a later section.

As the numerical simulation progresses, the model steps forward in time and solves the finite difference equations describing the continuity of the medium, fluid flow and heat transfer. The duration of each of these "time steps" can vary significantly depending upon the conditions that exist in the model. Basin2 automatically determines the time step based on a number of parameters, including the velocity of fluid flow, and changes in pressure and temperature. Many of the Canning River simulations required 75,000 time steps or more and a few required over 300,000 time steps.

Initial and boundary conditions

The initial conditions for the simulation are a hydrostatic pressure distribution and a conductive temperature gradient within the pre-Mississippian basement rocks. We could have chosen to begin the model using steady-state pressure and temperature conditions, but because of the duration of the simulation and the relatively low permeability of the basement rocks, the initial conditions have little influence upon the evolution of the model.

The boundary conditions stipulate the environment along the edges of the model. In our Basin2 simulations, we specify boundary conditions for both temperature and pressure, or heat and mass flux; these conditions can vary both in time and in space. The bottom boundary, which is along the base of the 2,000 ft thick basement unit, is always an impermeable barrier to flow with a conductive heat flux. The low permeabilities in the metamorphic basement rocks make this an appropriate horizon to place a no-fluid flow boundary. Basement heat flow would be most accurately simulated if the grid boundary were placed at the base of the crust, at a depth of about 15 km. However, this would be computationally burdensome and for practical reasons we place the bottom boundary beneath 2,000 ft of basement rocks.

As we discuss below in the "thermal calibration" section, a basal heat flux of 50 mW/m^2 gives the best match between predicted and measured values for both present thermal gradients and vitrinite reflectance data. The lateral boundaries are closed to fluid flow and heat transfer.

The top boundary represents the sediment surface. Below, we discuss the temperature and pressure conditions that we apply to this upper boundary over the duration of the simulation. The pressure conditions are determined by the water depth or topographic relief. When the surface is at or below sea level (*i.e.* water depth is greater than or equal to 0), the pressure along the sediment surface corresponds to hydrostatic pressure at that depth. When the surface is subaerial (defined in the model as negative water depths), the upper boundary represents the water table and the pressure remains constant at 1 atm.

Surface Temperatures

Present surface temperatures average approximately -5 ° to -12 °C (Lachenbruch and Marshal, 1986, Brewer, 1987, Lachenbruch and others, 1988). These subfreezing surface temperatures have existed for the last several million years on the North Slope and have led to the development of permafrost at approximately 1-2 Ma. As discussed previously, we compensated for Basin2's lower temperature limit of 0.5 °C, by applying a surface temperature of 0.5 °C and assigning special lithologic properties to the permafrost. This approach allowed our model to closely approximate the temperature (about -1 °C) at the base of the permafrost.

Prior to approximately 5 Ma, surface temperatures were above freezing based on paleoclimate reconstructions (Habicht, 1979; Parrish and Barron, 1986). Table FF3 lists the surface temperatures used in our model at the conclusion of each of the 19 time intervals. In the simulation, the surface temperatures change linearly with time from the end of one time period to the next.

Water Depths and Topographic Relief

Houseknecht and Hayba (Chap. HG) inferred water depths for each Brookian depositional sequence based on the facies interpretations of Houseknecht and Schenk (Chap. BS). We incorporated their estimated water depths in our model (Table FF3). The accuracy of these estimates is not

critical to the simulation because subsea depths only increase pressure along the hydrostatic gradient and thus provide no drive for flow. The increased pressure added by an overlying water column may slightly modify the effective depth-porosity and permeability-porosity calculations, but the impact on the simulation is minimal.

Subaerial topographic relief, however, is a significant driving force for flow. Based on evidence from fission track analysis (O'Sullivan and others, 1993), we estimated that subaerial topography began to develop in the southern portion of the modeled cross section shortly after 24 Ma and continued to the present (Table FF3). Except for the present topography, our estimates for the amount of paleorelief are rather poorly constrained. We chose values that were both consistent with the present day relief and with the estimated amount of section that has been removed by erosion (Table FF2). However, topography could have been significantly greater in the past than the maximum elevation of 1,500 ft assumed for the southernmost end of the section.

GEOLOGIC MODEL

Sequence Stratigraphy

Time-stratigraphic contacts are the primary input parameters to a Basin2 numerical model. Each contact depicts how the modeled section appears at the end of a given time period. For the Canning River model, we defined 19 time-stratigraphic units. The first unit (the uppermost 2,000 ft of the basement) defines the initial conditions for the transient simulation which begins at 355 Ma. In other words, the simulation begins with the deposition of the second unit (the Endicott sediments) onto the basement which is already incorporated into the model. The last time-stratigraphic unit includes the formation ("deposition") of the permafrost. For each time-stratigraphic unit, the model requires input concerning the time at the end of the period and the thickness and type of sediment deposited (or amount eroded) at a number of control points or "wells" along the section. We defined the stratigraphic contacts at the 10 wells located along the cross-section and at two synthetic, or "pseudo" wells, one at each end of the section. For each of the 19 periods, Table FF2 lists the age and the thickness of sediment either deposited or eroded at each well. Because the thicknesses of the units change with time due to differential compaction, the values listed for periods of deposition refer to compacted (present-day) thicknesses. The amount of

sediment actually deposited is greater than the observed stratigraphic section; the thickness of sediment deposited depends upon the functions that describe the compaction of each rock type through the collapse of pore space (*i.e.*, Basin2 "decompacts" the observed stratigraphic section). For periods of erosion, the values listed in Table FF2 indicate the thickness of sediment actually removed during that time period. Because during unloading the sediment regains a portion of its porosity lost during compaction, the "eroded thickness" of a unit that is completely removed will be slightly greater than its depositional "compacted thickness".

As noted above, we used the stratigraphic interpretation prepared by Bird (Chap. GG, Plate GG3) to define the contacts for the geologic units below the LCU. To simplify the model, we combined the Sadlerochit Group, the Shublik Formation and the Sag River Sandstone into one stratigraphic unit. Above the LCU, we incorporated the time-stratigraphic contacts from the sequence stratigraphy developed by Houseknecht and Schenk (Chap. BS).

At the southern end of the section, erosion has removed much of the Brookian section. To model the evolution of the Canning River section, it is not only necessary to assess the total thickness of missing section, but to estimate the original thicknesses of each of the stratigraphic units. As we discuss later, the vitrinite reflectance data help determine the total missing thickness, but not the thickness of the individual units. To help constrain our reconstructed section, we relied on the isopach maps generated by Houseknecht and Schenk (Figs. BSG6-10). Their maps indicate that the thicknesses of sequences E (Paleocene), D (late Paleocene), and C (Eocene) increased toward the south except where these units have been thinned by erosion. Therefore for the southernmost end of the section, we estimated the original thicknesses of these units by extrapolating Houseknecht and Schenk's (Chap. BS) isopach values (see Table FF2).

In contrast to the lower Brookian section, the uppermost units thicken to the north. This reversal corresponds to the uplift of the Sadlerochit Mountains just south of the 1002 area. The isopach maps of Houseknecht and Schenk (Figures. BSG9-10, this volume) suggest that the original thickness of sequence B (Oligocene) was minimal over the southern portion of the section and that sequence A (Miocene) only was deposited to the north of the Alaska State J-1 well. To better simulate the northward migration of the "zero depositional edge" during this time, we split sequence A (Miocene) into a lower and upper portion (see Table FF2). During these time periods

and during the Pliocene, uplift and erosion occur in the southern portion of the section, while deposition and subsidence occur toward the north.

Evolution of the Basin

The series of plots in Figure FF2 illustrates the stratigraphic evolution of the Canning River section. These plots show the results of the Basin2 model at the following 6 times: 1) 134 Ma, following the deposition of the Kingak (just prior to the development of the LCU); 2) 65 Ma, at the basal Tertiary unconformity (BTU); 3) 53 Ma, at the Eocene unconformity; 4) 24 Ma, following the deposition of "sequence B" (Houseknecht and Schenk, Chap. BS), just prior to the development of topography; 5) 1 Ma, approximately the beginning of permafrost development; and 6) at the present time.

Although the model is a necessarily simplified version of reality, it reflects the gross features of the basin evolution. It is consistent with Bird's (Chap. GG) conceptualizations of the evolving basin and with Houseknecht and Schenk's (Chap. BS) sequence stratigraphy. The modeled stratigraphic thicknesses also take into account 1) sediment compaction trends which are congruent with observed porosity-depth relationships, and 2) porosity rebound functions due to unloading. More importantly, the modeled section is also compatible with constraints provided by the vitrinite reflectance, fluid inclusion, and apatite fission track data (as discussed in subsequent sections).

CONSTRAINTS ON MATRIX PARAMETERS

Lithologies

For each of the stratigraphic units defined in the model, Basin2 requires a description of its lithology and how it varies along the length of the section. Basin2 utilizes this lithologic information to estimate the physical properties of the matrix as it evolves through time. Wireline well logs were the primary source for the lithologic data, which were compiled largely by A.C. Huffman, Jr. (U.S.G.S., written commun., 1997). Except for the basement, the lithology for each unit at each well is represented in the model as a compositional mixture of sandstone, shale, and carbonate (Table FF4). For each of these end-member rock types, Basin2 uses empirical correlations (listed in Table FF1 and discussed in the "Description of Basin2" section) to define the functional relationship between porosity and effective depth and

how permeability and thermal conductivity vary as functions of porosity. In the following sections, we justify our choice of functions for effective depth-porosity, porosity-permeability, and porosity-thermal conductivity.

Because Basin2 represents the lithology as mixtures of sandstone, shale, and carbonate, it is necessary to average the values calculated for these end-member rock types to determine representative values for permeability and thermal conductivity at each node of the model. The method of averaging strongly influences these values. In the "Z" direction, we employed harmonic averages, which are commonly used for estimating matrix properties normal to the direction of layering (see Bethke and others, 1993). This method results in an average permeability slightly greater than the lowest value (usually shale) determined for the three rock types. Along layering in the "X" direction, the model used arithmetic averages except when the node contained 30% sandstone or less, in which case geometric averages were used. Arithmetic averages favor the higher permeability values, which are appropriate for continuous sands. We used the geometric averages when the sand percentage was low because it better represents non-continuous (pods) sand lenses and results in lower permeability values in the model. As we discuss in a later section, these lower permeabilities help the model better match predicted pressure distributions.

The basement unit in the model represents strata older than 355 Ma. Porosity and permeability measurements on basement rocks are very low (Nelson, Chap. PP), suggesting that fluid flow through these rocks was minimal during the evolution of the Brookian section. To ensure that the model honored these low values, we defined separate empirical functions to describe the matrix properties of the basement (Table FF1). We also defined special lithologic properties for the permafrost (discussed above) to simulate its unique characteristics.

Depth-Porosity Functions

Although Basin2 has default functions that calculate matrix properties for sandstone, shale, and carbonate, Bethke and others (1993) encourage program users to tailor these functions to their specific applications. For our Canning River model, we used the porosity and permeability data from a number of wells and surface samples in the vicinity of the 1002 area to fit the effective depth-porosity and porosity-permeability functions. As discussed later, we found that these modified functions provided a better fit

between modeled and measured depth-pressure profiles than did the default functions.

Porosity data for the 1002 area come from conventional and mercury-injection-capillary-pressure (MICP) studies of plugs cut from drill core (Tables PP3 and PP4) and from sidewall cores. Nelson (written commun., 1998) cautions that porosity values from sidewall cores are less reliable than data obtained from plugs cut from conventional cores. On a larger scale, there are also porosity determinations from well logs. Nelson (Chap. PP) describes the methods used to compute porosity from logs for those intervals that satisfied criteria for net sand. From these measured and computed porosity values, Nelson compiled cumulative porosity distributions for selected formations for some wells. Because these porosity distributions are biased toward the sand-rich intervals, we used the 50% values (the median values) as an estimate of the mean sand porosity and the 5% values as an approximation of the shale porosity. Figure FF3a shows porosity data for wells in the Point Thomson area and Figure FF3b shows data for the offshore wells. The Point Thomson and offshore wells are ideal for evaluating the decrease in porosity with depth because these regions have received nearly continuous sediment deposition since the late Cretaceous (except for the interval that resulted in the basal Tertiary unconformity). We modified the effective depth-porosity functions used in our Basin2 simulations for sandstone, shale, and carbonate to fit these data, as shown in Figures FF3a and FF3b. It is important to note that when fitting these functions, we plotted the porosity data against vertical "depth" rather than against the adjusted parameter, "effective depth." By doing so, we have ignored the secondary effect of overpressure on porosity. Given these uncertainties and the paucity of data, Figures FF3a and FF3b indicate that the (effective) depth-porosity functions for sandstone, shale and carbonate listed in Table FF1 are reasonable approximations for the evolution of porosity in the 1002 area.

If we apply these same effective depth-porosity functions to wells in the southern portion of the Canning River section, it is possible to approximate the amount of uplift these areas have experienced. These estimates are minimum values because unloading can result in an increase in porosity. Also, no attempt has been made to estimate what percentage (if any) of the total porosity is secondary porosity. As shown in Figure FF3c, fitting our effective depth-porosity curves to the Canning River A-1, Canning River B-1, Beli, Gyr, and Alaska J-1 wells suggest uplifts of at least 18,000 ft, 9,000

ft, 6,000 ft, 6,000 ft, and 0 ft, respectively. These estimates, which have uncertainties of at least 25%, are in reasonable agreement with the geologic estimates for erosion in this area (see the isopach maps in Houseknecht Schenk's Chap. BS, Figs. BSG5-10). Our Basin2 model incorporates uplift amounts of 17,900 ft at Canning River A-1, 11,600 ft at Canning River B-1, 6,600 ft at Beli, and 200 ft at Alaska J-1 well (Table FF2). We chose to use these values because they result in the best fit between the modeled and measured vitrinite reflectance data (presented in a later section).

Porosity-Permeability Functions

A number of samples with porosity measurements also had permeability measurements. Data came from both conventional and mercury-injection-capillary-pressure (MICP) studies of drill core and surface samples (Table PP4). Figure FF4a shows these data along with permeability values estimated from sidewall cores. It is important to note that the permeability values from sidewall cores are not from direct measurements but are inferred from the porosity data and grain size observations (P. Nelson, U.S.G.S., written commun. 1998). Figure FF4b shows the data from the conventional and mercury injection studies plotted in terms of the host formation. The porosity-permeability functions that we used in Basin2 for the end-member rock types, sandstone, shale, and carbonate, are also shown (solid color lines). Because the data were collected primarily with the intent of documenting possible petroleum reservoirs, the values are skewed toward the sandy, more permeable intervals. Therefore, we fit the function for sandstone through the data and estimated that the shale values would be approximately 1-2 orders of magnitude lower than the lowest values measured. The carbonate function approximates values measured on the Lisburne Group limestone and dolomite. The maximum permeabilities permitted in our simulations for sandstone and carbonate were 10^4 md and 10^3 md, respectively.

Porosity-Thermal Conductivity Functions

There are no thermal conductivity data for the 1002 area or for the Canning River wells. Blackwell and Steel (1989, Table 2.2), however, reported typical ranges for *in situ* thermal conductivities for different lithologies at 20 °C. As a first approximation, we modified the default porosity-thermal conductivity functions used in Basin2 so that the calculated values would be consistent with their values (Table FF5).

The only available thermal conductivity measurements on samples from formations included in our model come from the NPRA, more than 300 km to the west of the Canning River. Deming and others (1992) made over 600 measurements of thermal conductivities on drill chips and core from a number of wells in the NPRA (summarized in Table FF5). Most of their measurements were made on drill chips, which yielded matrix conductivities, but they also obtained bulk conductivities using divided bar and needle probe measurements on water saturated core samples. They also estimated *in situ* thermal conductivities for different sample intervals for 21 wells. *In situ* conductivities, (which are bulk conductivities measured in the well) are lower than matrix conductivities because of the effect of porosity and the low thermal conductivity of water (about 0.6 W/m K). Temperature effects also reduce conductivities for sandstone and carbonates, but may increase values for shale (see summary by Robertson, 1979).

For the Lisburne Group, Deming and others (1992) estimate that the *in situ* conductivity is approximately 2.9 W/m K, about 22% lower than the 3.7 W/m K that they measured for the matrix conductivity. They also note that for the Torok formation, which is shale rich and has low thermal conductivity, the *in situ* conductivity is only about 5% less than the matrix conductivity. We used these two estimates of *in situ* conductivity to approximate values proportionally for *in situ* conductivity for the other geologic units with matrix conductivity values (Deming and others, 1992). We then further refined the porosity-thermal conductivity functions used in our Basin2 model (see Table FF1), so that there was reasonably good agreement with these *in situ* approximations (Table FF5).

PRESSURE DATA AND CALIBRATION OF PERMEABILITIES

Pressures

Pressure data are available for a number of the wells in the model area. Most pressure values are estimates derived from logs of the drilling mud weights (densities) and are therefore maximum pressures. There are also some data from hydraulic pressures and shut-in pressures collected during drill stem tests (Nelson, Chap. WL). In general, there is good agreement between hydraulic pressures and calculated mud-weight pressures where both data sources exist (see Fig. FF5). However, shut-in pressures were often much

lower than either the corresponding mud-weight pressures or hydraulic pressures, so we did not include these data in our analysis.

In compiling the pressure data from wells in the study area, it is evident that there are three pressure gradient regimes: 1) offshore, 2) the Point Thomson area, and 3) the southern Canning River wells. Offshore, geopressures (pressure in excess of hydrostatic pressure) increase gradually, but steadily, below about 2000 ft (Fig. FF5a). By 10,000 ft depth, the pressure in all five of the offshore wells (with pressure data) is 1.5 times hydrostatic (~2000 psi above hydrostatic). In the Aurora well, which is the only one of these 5 wells that extends below 10,000 ft, pressures are nearly twice hydrostatic by 18,000 ft, (~7000 psi above hydrostatic). Although there are several possible causes of geopressure, one of the principal causes of geopressure in this type of setting is thought to be the rapid accumulation of fine-grained sediments (see review by Graf, 1982).

In the Point Thomson area (Fig FF5b), pressures are generally only slightly greater than hydrostatic at depths less than about 9,000 ft. However, at greater depths, geopressures increase significantly, and at 14,000 ft, pressures in most wells are about 1.8 times hydrostatic (~5,000 psi above hydrostatic). In fact, pressures in this 10,000 to 14,000 ft depth range are greater than those determined for the Aurora well at comparable depths (Fig. FF5a). However, below 14,000 ft in the Leffingwell well, the only Point Thomson well to reach such depths, there is a substantial drop in pressure as indicated by a decrease in mud-weights. These lower mud-weights appear to reflect a true decrease in pressure because drilling records show that casing was set at this point in the well. The Leffingwell well encountered these low pressures, which are only slightly greater than hydrostatic, when it entered the Kekiktuk Conglomerate. This underlying low pressure region indicates a lateral (rather than vertical) source for the geopressures in the Point Thomson area. As we will demonstrate later in this paper, the offshore geopressures are a likely source of this pressure.

The wells at the southern end of the Canning River section do not have any significant geopressured zones. Pressure-depth profiles in these wells (Figure FF5c) exhibit very gradual increases. By 14,000 ft, pressures are only about 20% above hydrostatic. This relatively small amount of over-pressure is equivalent to approximately a 3,000 ft hydraulic head, which could be the result of topographically driven flow from the Brooks Range to

the south. It is also likely that these modest geopressures represent the distal remnants of the offshore and Point Thomson geopressures.

Calibration of Permeabilities

As shown previously in Figure FF4, there are ample permeability data from plugs and sidewall cores from wells in the Canning River region. However, most of these data were collected from the more permeable, sand-rich portions of the section while relatively few data are from mudstones and shale. In addition, it is difficult to judge how well these plug-size samples represent permeability on a basin scale. Although these data are helpful, particularly for sandstone and carbonate rocks, they leave some latitude in formulating an appropriate porosity-permeability function for shale.

Fluid pressure data (presented above) provide the best means of evaluating, on a basin scale, the appropriate permeability values to use in the Canning River model. The geopressure zones in the offshore wells (Fig. FF5a) suggest that in this area the sediments must have fairly low permeabilities. Bethke (1986) modeled this type of environment and found that geopressured zones are likely to form in shaly basins accumulating sediments at rates greater than about 0.1 to 1 mm/yr. Considering the thickness of the offshore Brookian section, sediment accumulation rates in the vicinity of the Galahad well are on the order of about 0.5 mm/yr since the Eocene. Therefore, the model should predict the development of the observed geopressured zones offshore for appropriately low values of permeability. In addition, this buildup of fluid pressure offshore should give rise to the geopressured zones that are present in the Point Thomson area over a relatively narrow depth interval (Fig. FF5b).

Through a number of simulations, we found that the porosity-permeability function for shale shown in Figure FF4 leads to the development of geopressured zones offshore and in the Point Thomson area (Figs. FF5a and FF5b). However, we were not able to simulate pressures as high as those observed in the wells, even though this function predicts shale permeabilities at least an order of magnitude lower than the few mudstones (10^{-4} md) analyzed from the Canning Formation. These simulated permeabilities are, however, within the range of values (as low as 10^{-5} md) measured by Neglia (1979) on Triassic-Pliocene shales. Using even lower permeabilities in the model produced geopressures more in line with observed values, but we felt that employing such low values would be unrealistic. Geopressures in excess

of those that we can account for by rapid, fine-grain sediment compaction may be the result of other possible mechanisms, such as lateral tectonic compression, hydrocarbon generation, or smectite dehydration (and the accompanying reduction in permeability).

THERMAL PARAMETERS: CONSTRAINTS AND CALIBRATION

Overview of Thermal Parameters

Because one of the primary goals of this study is to help evaluate the timing of oil generation, calibrating the thermal aspects of the model are critical. Parameters that influence the thermal modeling are the basal heat flux, thermal conductivity of the matrix, surface temperature, and sediment thickness (present and past). Of these factors, basal heat flux is probably the most important, but least constrained, parameter in our model in terms of data available from direct measurements. Therefore, most of our efforts to calibrate the thermal aspects of the model are directed toward evaluating basal heat flux.

For the most part, the other thermal parameters for the Canning River model are sufficiently well constrained from available data or reasonable inferences. For example, present surface temperatures are well known and the impact of any errors resulting from estimates of paleo-surface temperatures are probably minimal. Also, uncertainties in the original thicknesses of now-eroded sections are probably only a few thousand feet at most. Based on the isopach maps generated by Houseknecht and Schenk (Chap. BS), the greatest uncertainties are along the southernmost portion of the model. The remaining parameter, thermal conductivity, can have a significant impact on the results, given the range of "acceptable" values for each rock type. Fortunately, Deming and others (1992) measured matrix conductivities and estimated *in situ* values on similar geologic units to the west of the 1002 area in the NPRA. We adjusted Basin2's porosity-thermal conductivity functions (Table FF5) to reflect these values. As will be shown below, these functions resulted in reasonably good fits to both the geothermal gradients and reflectance profiles.

The two main constraints that are available to calibrate the thermal results are 1) present geothermal gradients, and 2) vitrinite reflectance profiles. Fluid inclusion data and apatite fission track analyses provide other useful, but more limited constraints. Because geothermal gradients respond

relatively rapidly to changing conditions, fitting the model to these gradients provides an estimate of the present heat flux into the basin. The vitrinite reflectance data add another dimension to the calibration because they represent the integrated effect of temperature over time. The approach we employed was to try to match both sets of data with the least variation in basal heat flux in either time or space.

After several runs testing various heat fluxes and some "fine-tuning" of the matrix conductivity functions and the amount of erosion in the south, we were able to fit the model to both the thermal gradients and the vitrinite reflectance profiles reasonably well with a constant basal heat flux of 50 mW/m^2. In the following sections, we discuss the available thermal data and present the results of the model using this heat flux.

Heat Flux

For our Canning River model, the basal heat flux boundary condition applies to the conductive heat entering the basement rocks at depths ranging from about 7,000 ft in the south to greater than 30,000 ft offshore. Because this boundary condition represents the primary source of heat in the simulations, it has a significant impact on the present thermal gradients and maturation levels predicted by the model. Unfortunately, heat flux has not been determined for any of the wells in the Canning River region. We do, however, anticipate that there is relatively little variation in the conductive heat flux from the basement over the 160 km length of the model.

In the absence of direct heat flux data for the Canning River section, there are some general guidelines to help estimate the basal heat flux. The worldwide average heat flux for continental crust is approximately 60 to 65 mW/m^2 (Gretener, 1981). It is important to note that this deep conductive heat flux can be significantly different than the shallow heat flux. For example in areas of rapid sedimentation, such as the Gulf of Lions basin, shallow heat fluxes are depressed to as low as 41 mW/m^2 (Burrus and Audebert, 1990). Advective heat transport by groundwater can also impact the shallow heat flux as Deming and others (1992) determined for the NPRA, more than 300 km to the west of the Canning River. There, Deming and others (1992) indicate that at shallow levels (depths less than about 2,500 ft) the heat flux increases from less than 30 mW/m^2 near the front of the Brooks Range to 90 mW/m^2 at the coast, a distance of about 250 km. They interpreted this pattern as evidence for advective transport of heat

suggesting that topographically driven fluid flow sweeps heat northward until it is driven up along the Barrow Arch. They also evaluated the heat flux at greater depths (from approximately 2,000 to 14,000 ft) and found a similar but less exaggerated pattern, with values increasing from about 45 to 90 mW/m^2. If, as they suggest, advective heat transport is the cause for this range in heat flux values, then these data are not directly applicable to the input requirements for the Basin2 model. Deming and others (1992) note that the average shallow heat flux in the North Slope Basin is 60 mW/m^2. Lachenbruch and others (1966, 1982) estimated an apparent background heat flux of 50 to 60 mW/m^2 at Prudhoe Bay and Cape Thompson. Therefore, our results, which indicate a best fit to the thermal constraints with a basal heat flux of approximately 50 mW/m^2, are not unreasonable.

Down-hole Temperatures

Temperature measurements on a number of wells are reported in Table WL9. T. Collett of the U.S. Geological Survey corrected (when possible) these values using the procedure of Dowdle and Cobb (1975) to eliminate the effects of drilling. Because of the paucity of data, we compiled the data from all wells in the general vicinity of our cross-section into the same three groups that we used to evaluate pressure: 1) offshore wells, 2) wells in the Point Thomson area, and 3) wells in the vicinity of the southern Canning River (Figs. FF6a-FF6c). This approach also allowed us to better determine thermal trends along the cross-section. Because of the lack of data, we included down-hole temperature measurements that could not be corrected (indicated by open symbols on Figs. FF6a-FF6c), with the understanding that non-corrected values from shallow depths probably overestimate true formation temperatures while deeper measurements probably underestimate temperatures due to the effects of drilling (T. Collett, pers. commun., 1998). For each of the three groups, we estimated the thermal gradient beneath the permafrost by fitting (by eye) a line through the data.

In the Point Thomson area, the down-hole temperature data define a thermal gradient of about 32 °C/km (Fig. FF6a). The base of the permafrost in this area is at approximately 2200 ft. There is surprisingly little scatter in the data, except as expected in the uncorrected data.

Thermal data from the offshore wells indicate a thermal gradient of about 26 °C/km (Fig. FF6b). However, there is at least a 20 % uncertainty in this estimate because of the limited data and the spread in temperatures at

shallow depths. In fact, if the two shallow data points from the Kuvlum 1 well are excluded (which are about 15 °C higher than shallow measurements from the nearby Kuvlum 2 well), the thermal gradient for the offshore wells is nearly identical to that of the Point Thomson area. The spread in these shallow measurements may reflect differences in the thickness and depth of the permafrost as it thins to zero within about 15 km of shore (T. Collett, pers. commun., 1998), or the effects of drilling were not completely removed from these samples.

Compared to the Point Thomson and offshore wells, the temperature data from wells in the southern portion of the study area indicate a somewhat different thermal regime (Fig. FF6c). The most noticeable difference is the steep thermal gradient (~58 °C/km) directly beneath the permafrost, which varies in thickness in this area from about 1,000 to 2,000 ft. At depths of 3,000 to 5,000 ft, temperatures in these southern wells are about 20 - 30 °C higher than the expected temperatures in the Point Thomson area at comparable depths. At greater depths, the thermal gradient in the southern wells decreases sharply to about 23 °C/km, and at depths greater than about 11,000 ft, temperatures are essentially the same as those found in the Point Thomson area. What is the reason for this apparent thermal "bulge" beneath the permafrost in the southern wells, and is it real?

The most compelling evidence for a shallow thermal anomaly in the south is the Red Hill thermal spring. Temperatures of about 30 °C have been measured at this spring (Childers and others, 1977; Wang, Chap. SA), which is located at the western end of the Saddlerochit Mountains, less than 5 km east of Canning River B-1 well (Fig. FF1). In addition to its proximity, the 30 °C temperature of this spring is close to the projected surface temperature (approximately 20 °C) of the deep thermal gradient (Fig. FF6c). The source area of these thermal waters is not known, but stable oxygen and hydrogen isotope ratios demonstrate that the water originated as precipitation and that little rock-water interaction has occurred (Wang, Chap. SA). Tritium analyses indicate that the spring water is younger than 40 years old and that it may be only a few years old (Wang, Chap. SA). Although no other thermal springs have been found, Childers and others (1977) note ground water discharges in the form of icings along the Canning, Kavik and Shaviovik Rivers in the general vicinity of the southern wells.

Therefore, we suggest that the thermal anomaly, or "dog leg" in the thermal gradient depicted in Figure FF6c is the result of advective heat flow. One

possible scenario is that topographically driven fluids from the Franklin Mountains to the south circulate to depths of at least 5,000 - 6,000 ft. These fluids are then heated and flow up along low angle thrust fault zones. In most areas, the permafrost prevents these warm waters from reaching the surface, forcing them to flow laterally beneath the permafrost where they quickly cool. Although the origin of the thermal anomaly is speculative, it is doubtful that the thermal regime has existed sufficiently long to affect the thermal maturation of the sediments in the southern portion of the cross section.

Figure FF6 also shows the Basin2 simulated thermal gradients along with the measured data from the three main regions of the cross section: 1) offshore, 2) the Point Thomson area, and 3) the southern Canning River. These simulated gradients fit the measured gradients reasonably well in the Point Thomson and offshore regions. (The vertical simulated temperature gradient at 0.5 °C reflects the method we devised, described earlier, to simulate the temperature at the base of the permafrost because of Basin2's inability to model temperatures less than 0.5 °C.) However, for the southern Canning River wells, the fit is rather poor when the surface temperature is held at 0.5 °C. As discussed above, we believe that the "dog-leg" in the geothermal gradient reflects advective heat transport as evidenced by the thermal spring at Red Hill. Although it was not possible to include these fluids in the present Canning River model, we can account for this heat in a crude way by increasing the surface temperature to about 20°C at the southern end of the model during the last million years of the simulation. With this approach, the simulated gradient matches the measured values at depths greater than about 3000 ft (about -2000 ft elevation), again indicating a heat flux of about 50 mW/m^2.

Vitrinite Reflectance

Vitrinite reflectance data are widely used to gauge the maturation level of petroleum source rocks. In addition, these data provide a critical constraint for the Basin2 modeling on the thermal evolution of the region. Because vitrinite reflectance integrates the effects of temperature over time, it is an important tool for helping calibrate several parameters, such as basal heat flux, depth of burial, and thermal conductivity. Basin2 uses the parallel reaction model of Sweeney and Burnham (1990) (also known as the LLNL vitrinite model) to predict the evolution of vitrinite reflectance. By comparing the predicted values to the measured values, we can evaluate how

well the model matches the thermal evolution of the basin. Unfortunately, the data set for some wells contains a significant amount of scatter. Bird and others (Chap. VR) and Houseknecht and Hayba (Chap. HG) have evaluated the vitrinite data and discuss both data quality and interpretation issues.

Houseknecht and Hayba's (Chap. HG) interpretation of recycled vitrinite helps explain much of the scatter in the depth - vitrinite reflectance profiles for many of the wells. In the Point Thomson area, they suggest that recycled vitrinite extends to depths of about 8,000 ft (Fig. HG3). To the south, the maximum depth of recycled vitrinite decreases to approximately 3,500-4,000 ft at the Beli well. In calibrating the numerical model, we found that we could much better match the reflectance data when we ignored values that appeared to be from recycled vitrinite.

The depth - vitrinite reflectance profiles shown by Bird and others (Chap. VR) illustrate some of the other problems with the data. Since most of the data were obtained by industry and then released to the public domain, we have little information concerning the methods of data collection. In particular, there is an unusually large amount of scatter in the West Staines 2 data. Also the two data sets collected on the Canning River A-1 well are quite disparate.

Figure FF7 shows the simulated vitrinite reflectance profiles plotted against the measured values at several wells. Assuming that the data from the shallow portions of the wells represents recycled vitrinite as proposed by Houseknecht and Hayba (Chap. HG), there is a good fit between the simulated and measured values for most of the wells, considering the scatter in the Ro data. The fit is probably the poorest for the Canning River B-1 well, where the simulated values are somewhat low. This difference could indicate that we have underestimated the thickness of sediment removed by erosion. The data from the Canning River A-1 well are problematic because of the disparity between the two sets of measurements. Although the GMC data look like a more reasonable data set in terms of the increase in Ro with depth, we were not able to match this trend with any heat flux value. In fact it appears that these data would require significantly lower matrix thermal conductivities and higher heat flux values than are reasonable for other portions of the cross section. Therefore, we included on Figure FF7g the data from the Kavik 1 well, which is only about 5 km to the east of the Canning River A-1 well. For the most part, the Kavik 1 data plot midway

between the other two data sets, and our simulations match best to these data.

Fluid Inclusion Data

In the general vicinity of the Canning River section, the only temperature data from fluid inclusion analyses come from the Kavik 3 well, which is approximately 5 km west of the Canning River A-1 well. Burruss (Chap. FI) analyzed fluid inclusions in quartz and calcite from the Sag River and Shublik Formations at depths of 4,946 to 5,069 ft. He reports homogenization temperatures of 175-180 °C for inclusions in quartz and 180-185 °C for inclusions in calcite (Table FI2). Burruss also reports that these inclusions contain methane-rich gas and a blue fluorescent liquid and gas, which suggests the presence of a high API gravity, gas-rich petroleum.

Figure FF8 shows the temperature history of the model node that corresponds to the Sag River and Shublik Formations in the Canning River A-1 well. The maximum temperature experience by that node is about 165°C. Temperatures of adjacent nodes suggest an error of about ±10 °C. Given the uncertainty in representing the location of the fluid inclusion data by a node in the model, the model matches the fluid inclusion data reasonably well. To better match the 175-185 °C temperatures that Burruss (Chap. FI) reports, higher heat fluxes and (or) greater burial depths are required in the southern portion of the model. It is also possible that the fluid inclusion data do not represent true formation temperatures, and that these data record a short-lived pulse of warm water that traversed the area. Because of the disparity in the vitrinite reflectance data, it is impossible to evaluate which scenario is the more appropriate representation.

Apatite Fission Track Analyses

O'Sullivan and others (1993) analyzed fission tracks in apatite from outcrop samples in the vicinity of the Canning River A-1 and B-1 wells. Their analysis provides thermal data and tectonic constraints for our numerical model. Their uppermost stratigraphic sample (87POS22B) was from the Sagavanirktok sandstone, above the Eocene unconformity and north of the Canning River B-1 well. Fission tracks in this sample indicate that this formation has never been heated above 80 °C. In contrast, samples from the underlying Canning Formation have been totally annealed and thus must have been heated to temperatures greater than 110 °C. O'Sullivan and others

(1993) interpret that uplift and cooling of these samples occurred at about 45 Ma and again at about 23 Ma. Figure FF9 shows the time-temperature history for the nodes that correspond most closely to these apatite sample localities. Although there is a fair amount of uncertainty in locating the nodes relative to the data, it appears that the maximum predicted temperatures agree well with the apatite fission track analyses.

O'Sullivan (1993) also examined apatite fission tracks in Late Cretaceous to Tertiary sediments from the Alaska State C-1 well in the Point Thomson area. He determined that these strata are currently at their maximum temperatures (*i.e.*, they do not show evidence of elevated paleotemperatures after deposition). The model is in agreement with this situation.

TIMING OF PETROLEUM GENERATION

Source Rocks and Geochemical Parameters of Oil Generation

One of the primary purposes for developing a numerical model of the Canning River section was to evaluate the timing of oil generation from potential source rocks. Magoon and others (Chap. PS) have identified three petroleum systems within and adjacent to the 1002 area. The likely source rocks and the "oil-type" name are as follows for these three systems: 1) the Shublik Formation sourced the Prudhoe oil-type found in the Ellesmerian(!) system; 2) the Hue Shale sourced the Jago oil-type found in the Hue-Thomson(!) system; and 3) the Mikkelsen Tongue of the Canning Formation and its lateral, offshore equivalent likely sourced the Manning oil found in the Canning-Sagavanirktok(!) system. All three of these source rocks are present along at least portions of the Canning River section. The Jurassic Kingak Shale and the Lower Cretaceous pebble shale are also organic-rich units found along the Canning River section; however, these units are gas-prone source rocks within and adjacent to the 1002 area (Magoon and others, 1987, and Keller and others, Chap. SR).

For each source rock, Basin2 evaluates the timing of oil generation by estimating the fraction of oil produced by a source rock using the Arrhenius method of Lewan (1985). To employ this method effectively, it is necessary to input values for the activation energy, E_A, and frequency factor (also called the pre-exponential factor), A_o, for each source rock. These kinetic constants are derived from a series of hydrous pyrolysis experiments. Lillis and others (Chap. OA) ran such experiments on samples of the Shublik

Formation and Hue Shale. They determined that the kinetics for these units are similar to the "slow" Type IID kerogens, such as the Woodford Shale. Their recommended values for E_A and A_o are listed in Table FF6. Although they did not determine kinetic constants for the Manning oil type, they state that this oil type appears to come from a mixed type III and type II organic source. Lillis and others (Chap. OA) also note that the Manning oil is very similar in composition to oils in Paleogene reservoirs from the Mackenzie Delta - Beaufort Sea area. Issler and Snowdon (1990) ran a series of pyrolysis experiments and determined that they could best fit the hydrocarbon generation characteristics of the Beaufort-Mackenzie basin oils by modeling them with 10 to 11 parallel first-order reactions. The activation energies, E_A, for these reactions range from 190 to 290 kJ/mole with the major contribution to hydrocarbon generation occurring at 230 kJ/mole. We use this value and the associated frequency factor, A_o, to estimating the fraction of Manning oil generated by the Mikkelsen Tongue of the Canning Formation (Table FF6).

Timing of Source Rock Maturation

Figure FF10 illustrates the predicted maturation histories for the likely source rocks located along the Canning River section. Each plot tracks the predicted maturation values for a series of nodes within the appropriate formation. It is important to note that because each node represents a given thickness [up to 1,300 ft (400 m)] the plots just show the history of the midpoint of the unit. The error associated with this discretization of the model is fairly minimal and does not impact our conclusions on the timing of petroleum generation.

The oldest likely source rock is the Shublik Formation. Its predicted maturation history is shown in Figure FF10a. The Shublik extends from the southern margin of the model northward to somewhere between the Beli 1 and Alaska J-1 wells where it is truncated by the LCU. Along this rather limited extent, the maturity ranges from over-mature in the south to immature at the Alaska J-1 well, if the unit extends that far north. South of the Canning River B-1 well, the Shublik was in the main phase of hydrocarbon generation from approximately 58 Ma to about 40 Ma. Slightly north of that well, hydrocarbons have been generated since about 50 Ma and are probably still being generated.

The Hue Shale extends from the southern margin of the model northward to at least Point Thomson. As shown in Figure FF10b, the maturity of the Hue increases from over-mature south of the Canning River B-1 well to the early phase of generation near the Beli well. To the north of Beli and extending to the Mikkelsen High, the Hue Shale is immature. The earliest main phase petroleum generation began in the south (at approximately 50 Ma at the Canning A-1 well), and the unit continues to generate oil in the vicinity of the Canning River B-1 and Beli wells. Although the Hue is only known to extend as far north as Point Thomson, it is possible that it is present north of the Mikkelsen High. If so, any Hue Shale north of Hammerhead 1 well would have generated all of its potential petroleum between about 35 and 25 Ma (Fig. FF10c).

The Mikkelsen Tongue of the Canning Formation is the youngest possible source rock found along the Canning River section. It extends from north of the Beli 1 well to at least the Point Thomson area. North of that point, the extent of the lateral equivalents of the Mikkelsen Tongue is unclear. As shown in Figure FF10d, any possible oil sourced from the Mikkelsen Tongue would have to have come from north of the Mikkelsen High because all points to the south never became mature.

Although there are slight differences, these results are consistent with the timing of onset and end of main phase of oil generation estimated with one-dimensional modeling of Houseknecht and Hayba (Chap. HG) and with the two-dimensional conduction modeling of Rowan (Chap. BE).

RESULTS OF FLUID FLOW MODELING

Fluid Flow and Geopressure Development

The results of fluid flow modeling for the Canning River section are shown in Figure FF11 for six time slices: 53, 37, 24, 15, 5, and 0 Ma. Each illustration shows the pressure distribution via a color cross-section and the temperature distribution by contours. Arrows show the direction of water migration.

For most of the evolution of the basin, the dominant force driving fluid flow was compaction. Prior to the Tertiary, flow was dominantly to the north because most of the sediment accumulation was in the south. Beginning in the Paleocene with the deposition of sequence E, flow directions reversed

north of the Mikkelsen high. Throughout the Paleocene and Eocene, compaction drove flow up the flanks of the Mikkelsen high from both the north and south sides. Beginning in the Oligocene, fluid flow throughout the region was dominantly to the south in response to the thick accumulation of sediments north of the Mikkelsen high. Subsequent to thrusting and uplift in the south, beginning at about 24 Ma in our model, topography became a significant force driving fluids northward. If our model had extended farther south, the impact of topography on flow would have occurred earlier (see Cole and others, Chap. SM). However, regardless of the exact timing, the influence of topography appears to be restricted to the shallower portions of the basin. At depths greater than about 5000 ft, compaction still dominates, driving fluids that were expelled from the offshore sediments further south. The geopressured zones at Point Thomson provide evidence that fluids are moving south out of the compacting offshore basin.

Previously, we documented the presence of geopressure zones both offshore and in the Point Thomson area (Figs. FF5a and FF5b). Although there are several possible causes of geopressure, one of the principal causes of geopressure in this type of setting is thought to be the rapid accumulation of fine-grained sediments (see review by Graf, 1982). With the rate and type of sediment deposition offshore, this description appears directly applicable for the offshore portion of the Canning River section. As seen on Figure FF11, geopressures began to develop during the rapid Eocene deposition and they continue to evolve presently. It is also apparent from Figure FF11 that compaction-driven flow has transmitted these geopressures from offshore to the Point Thomson area. Geopressures in excess of those predicted by the simulation suggest that either the shale permeability used in the model is not quite low enough, or there are other sources of geopressure as discussed by Graf (1982). It is also important to note that the mudweight pressures are maximum values.

The dominance of compaction-driven flow at depths greater than about 5,000 ft suggests that the conceptual model that Deming and others (1992) proposed for the NPRA area is not appropriate for the Canning River region. In an extensive heat flow study of the NPRA, Deming and others (1992) determined that at depths of 2,000 to 14,000 ft, heat flux increases from less than 45 mW/m^2 near the front of the Brooks Range to 90 mW/m^2 at the coast, a distance of about 250 km. They interpreted this pattern as evidence for deep advective transport of heat suggesting that topographically driven fluid flow sweeps heat northward until it is driven up along the Barrow

Arch. Due to the shallow depths that topographically driven flow penetrates in the Canning River area, their model is not feasible here. It is possible that a shallower, smaller version of their conceptual model does impact heat flow in the Canning River region, although the sparse down-hole temperature data do not indicate that such is the case.

The inferred differences in subsurface pressure and advective flow regimes between NPRA and ANWR may not be surprising considering the geologic contrasts between the two areas. The width of the foreland basin, between the thrust front on the south and the crest of the Barrow arch on the north, is about 250 km in NPRA, and only about 60 km along our Canning River section. In NPRA, the Barrow arch remained a prominent positive element throughout deposition of Brookian strata as indicated by marked thinning of the Brookian sequence onto the arch (Bird, 1988, Fig. 16.22). In ANWR, the Barrow arch (Mikkelsen high) diminished as a prominent positive element in the Eocene and exerted little influence on sediment thickness thereafter (Houseknecht and Schenk, Chap. BS). These contrasts likely are the result of timing between the tectonic evolution of the Arctic Ocean and deposition of the Brookian sequence. In NPRA, deposition of Brookian strata, which are middle through late Cretaceous in age, followed closely the early Cretaceous rift opening of the Arctic Ocean. The Barrow arch, considered to represent the uplifted shoulder associated with that rifting event, was a relatively young feature that remained positive throughout Brookian deposition. In contrast, Brookian strata in ANWR are Paleocene through Miocene in age and their thickness patterns over the Mikkelsen high (Houseknecht and Schenk, Chap. BS) suggest they span the interval of time during which the coastal area evolved from a rift shoulder to a rapidly subsiding continental margin. We suggest that these contrasts in width of the foreland basin and prominence of the Barrow arch as a positive element resulted in significant contrasts in advective fluid flow in ANWR and NPRA.

Implications for Hydrocarbon Migration

Modeling of hydrocarbon generation suggests that the onset of main phase oil generation from the Hue Shale or other potential source rocks near the base of the Brookian section occurred at or slightly before 50 Ma in the southern portion of the undeformed area. Since that time, the area of main phase generation has continually progressed northward (Fig. FF10a, b; see also Houseknecht and Hayba, Chap. HG). Prior to about 24 Ma, (Fig. FF11a, b), most fluid flow was northward in the area south of the crest of the

Mikkelsen high (*i.e.*, most of the undeformed part of the ANWR 1002 area). Therefore, it is likely that any oil generated beneath the undeformed area initially migrated northward and upward toward the crest of the Mikkelsen high in response to both buoyancy and the hydrodynamic drive. In contrast, after ~24 Ma most fluid flow was southward in that same area, a consequence of the compaction-driven flow resulting from deposition of thick Brookian muds north of the crest of the Mikkelsen high. Despite this hydrodynamic drive to the south, it is likely that oil continued to migrate to the north due to the buoyant force of oil. More importantly, oil previously generated and trapped on the crest or flanks of the Mikkelsen high may have remigrated southward as a consequence of the reversal of flow vectors.

These preliminary interpretations regarding the influence of advective fluid flow on oil migration may explain an otherwise puzzling observation. Field work revealed the presence of oil stained Brookian sandstones (within sequence E or D of Houseknecht and Schenk, Chap. BS) along the Canning River, apparently in the position of the footwall of the Sadlerochit Mountains frontal thrust fault which is thought to have formed 25-20 Ma. The geochemistry of the oil recovered from those sandstones suggests derivation from the Hue Shale, which is thought to have generated oil beneath this location ~50-30 Ma. Thus, it appears that oil generation beneath this location pre-dated development of the structure that apparently traps the oil by at least 5 million years. However, if oil generated from the Hue Shale ~50-30 Ma initially migrated northward toward the crest of the Mikkelsen high it could have subsequently re-migrated southward toward the mountain front when fluid flow was reversed. This scenario may provide an explanation for “older” oil in a “younger’ trap. If correct, this interpretation also could enhance the probability for oil occurrence in relatively young traps throughout the ANWR 1002 area. It is also important to remember the possibility of water and oil migrating in the third dimension (*i.e.*, to the west along the crest of the Mikkelsen High/Barrow Arch).

CONCLUSIONS

Our modeling provides an integrated analysis of the stratigraphic, thermal and fluid migration history of the Canning River region. In this effort, we have attempted to incorporate in the model the essential aspects of the sedimentary and tectonic evolution of the basin as well as details about the primary lithologies and their matrix characteristics. We also have strived to calibrate the fluid flow and thermal characteristics of the model against

pressure and temperature data obtained from wells located on and near the line of section. The resulting model satisfactorily honors existing geologic, geophysical and geochemical data. Based on the development of, and the predictions derived from this model, we can draw the following conclusions:

Model Set Up and Constraints

1) Along the Canning River section, there are three general pressure regimes: the offshore, the Point Thomson area, and the southern Canning River area. Offshore, geopressures increase steadily with depth, and by 10,000 ft depth, pressure is 1.5 times hydrostatic and nearly twice hydrostatic by 18,000 ft depth. In the Point Thomson area, geopressures exist only over a limited depth interval (mainly 10,000-14000 ft), but are greater than those found at comparable depths offshore. The wells in the southern portion of the region do not have significant geopressured zones, and maximum pressures are roughly equivalent to a 3,000 ft hydraulic head.

2) Present geothermal gradients in the southern Canning River region differ from those measured in the Point Thomson and offshore wells. In these latter areas, the thermal gradients appear fairly linear with a value of about 32 °C/km. In the southern Canning River area, however, the gradients appear high (~58 °C/km) within a few thousand feet of the surface, but are relatively low (~23 °C/km) at greater depths. The cause of this "dog leg" in the gradient appears to be advective heat flow as evidenced by the thermal springs at Red Hill, located at the western end of the Saddlerochit Mountains, less than 5 km east of Canning River B-1 well.

3) Due to temperature limitations within the Basin2 program, we were unable to simulate *per se* the development of permafrost within the last 1 - 2 m.y. We were however able to work around this limitation and mimic the thermal and hydrologic effects of permafrost by treating it as a separate stratigraphic horizon with special lithologic properties, such as a high thermal conductivity, and very low permeability. This approach worked quite satisfactorily and allowed us to calibrate the model using down-hole temperature data from the base of the permafrost and below.

Results and Predictions

4) Using a heat flux value of 50 mW/m^2, the predicted thermal gradients and vitrinite reflectance profiles match reasonably well with measured

values along the entire Canning River section. These results suggest that the deep (basal) heat flux into the Canning River region is presently about 50 mW/m^2, and that it has probably been at about that level throughout the deposition of the Brookian sequence (about the last 130 m.y.). The uncertainty associated with this value is probably about 5 mW/m^2.

5) Geopressures in the offshore wells are the result of the compaction of the thick sequence of fine-grained sediments deposited in this area over the last 40 m.y. Geopressures in the Point Thomson area are a direct result of the offshore geopressures because fluids driven southward out of these compacting sediments transmit these geopressures into the Point Thomson area. Geopressures resulting from these migrating fluids extend south of the Point Thomson area about 50 km and dissipate to the north of the Beli well.

6) Using the "best fit" geochemical constants, the model predicts the maturation history for the three likely source rocks present within the Canning River section: 1) the Shublik Formation, 2) the Hue Shale, and 3) the Mikkelsen Tongue of the Canning Formation. At the southernmost end of the model, the Shublik began generating hydrocarbons at approximately 56 Ma. At its northern extent (in the vicinity of the Alaska J-1 well), it is immature, and near the Beli well it is probably generating hydrocarbons today. For the Hue Shale, the earliest petroleum generation also began in the south at approximately 50 Ma, and it continues to generate oil in the vicinity of the Canning River B-1 and Beli wells. Any possible portions of the Hue Shale north of the Hammerhead 1 well would have generated all its potential petroleum between about 35 and 25 Ma. The youngest likely source rock, the Mikkelsen Tongue, is immature, at least over its known extent from the Point Thomson area south. Any possible oil sourced from the Mikkelsen Tongue would have to have come from an extension of the formation offshore and to the north of the Barrow Arch.

7) For the NPRA area, Deming and others (1992) proposed that topographically driven ground-water flow circulates to depths of 10,000 to 20,000 ft and advectively transports heat from the south in the foothills of the Brooks Range to the north along the coast. Our simulations suggests that this conceptual model is not appropriate for the Canning River region because topographically driven flow in the south only reaches depths of about 5,000 ft below sea level. At greater depths, flow is dominantly driven to the south over the entire length of the model by compaction offshore.

8) Modeling hydrocarbon generation and fluid flow suggests that prior to about 24 Ma any oil generated beneath the undeformed area of the ANWR 1002 area initially migrated northward toward the crest of the Mikkelsen high. In contrast, after ~24 Ma most fluid flow was southward, being driven by compaction of the thick Brookian muds deposited north of the Mikkelsen high. In addition due to uplift in the south, the buoyancy of oil combined with the hydrodynamic drive would force any oil generated subsequent to this time to migrate southward. Therefore oil previously generated and trapped on the crest or flanks of the Mikkelsen high may have remigrated southward (or westward along the crest of the Mikkelsen High/Barrow Arch).

REFERENCES

Bethke, C.M., 1985, A numerical model of compaction-driven groundwater flow and heat transfer and its application to the paleohydrology of intracratonic sedimentary basins: J. Geophysical Research, v. 80, p. 6817-6825.

Bethke, C.M., 1986, Inverse hydrologic analysis of the distribution and origin of Gulf Coast-type geopressured zones, J. Geophysical Research, v. 91, no. B6, p. 6535-6545.

Bethke, C.M., 1989, Modeling subsurface flow in sedimentary basins, *Geologische Rundschau*, v. 78, p. 129-154.

Bethke, C.M., Lee, M. K. Quinodoz H.A.M., Kreiling, W.N., 1993, Basin modeling with Basin2, Hydrogeology Program, University of Illinois, 225 p.

Bird, K.J., 1988, Structure-contour and isopach maps of the National Petroleum Reserve in Alaska: in Gryc, G. (ed.), Geology and Exploration of the National Petroleum Reserve in Alaska, 1974 to 1982. U.S. Geological Suvey Professional Paper 1399, p. 355-377.

Bird, K.J., and Magoon, L.B. (eds.), 1987, Petroleum Geology of the Northern Part of the Arctic National Wildlife Refuge, Northeastern Alaska, U.S. Geological Survey, Bulletin 1778, 329 p.

Blackwell, D.D., and Steele, J.L., 1989, Thermal conductivity of sedimentary rocks: Measurement and significance: in Naeser, N.D., and

McCulloh, T.H. (eds.), Thermal History of Sedimentary Basins, Methods and Case Histories, Springer - Verlag, New York, p. 13-36.

Brewer, M.C., 1987, Surficial geology, permafrost, and physical processes: in Bird, K.J., and Magoon, L.B. (eds.), 1987, Petroleum Geology of the Northern Part of the Arctic National Wildlife Refuge, Northeastern Alaska, U.S. Geological Survey, Bulletin 1778, p. 27-36.

Burrus, J., and Audebert, F., 1990, Thermal and compaction processes in a young rifted basin containing evaporites: Gulf of Lions, France: American Association of Petroleum Geologists, v. 74, p. 1420-1440.

Childers, J.M., Sloan, C.E., Meckel, J.P., and Nauman, J.W., 1977, Hydrologic reconnaissance of the Eastern North Slope, Alaska, 1975: U.S. Geological Survey Open-File Report 77-492, 65 p.

Corbet, T.F., and Bethke, C.M., 1992, Disequilibrium fluid pressures and groundwater flow in the western Canada sedimentary basin, J. Geophysical Research, v. 97, no. B5, p. 7203-7217.

Craig, J.D., Sherwood, K.W., and Johnson, P.P., 1985, Geologic Report for the Beaufort Sea Planning Area, Alaska: Regional Geology, Petroleum Geology, Environmental Geology: U.S. Minerals Management Service, OCS Report MMS 85-0111, 192 p.

Deming, D., Sass, J.H., Lachenbruch, A.H., DeRito, R.F., 1992, Heat flow and subsurface temperature as evidence for basin-scale groundwater flow, North slope of Alaska: Geological Society of America, v. 104, p. 528-542.

Dowdle, W.L., and W.M. Cobb, 1975, Static formation temperature from well logs – an empirical method, J. Pet. Tech., Nov., p. 1326-1330.

Graf, D.L., 1982, Chemical osmosis, reverse chemical osmosis, and the origin of subsurface brines, Geochimica dt Cosmochimica Acta, v. 46, p. 1431-1448.

Grantz, A., May, S.D., and Hart, P.E., 1994, Geology of the Arctic continental margin of Alaska: *in* Plafker, G., and Berg, H.C. (eds.), The

Geology of Alaska, The Geology of North America, Geological Society of America, v. G-1, p. 17-48.

Gretener, 1981 Gretener, P.E., 1981, Geothermics: Using temperature in hydrocarbon exploration: American Association of Petroleum Geologists, Education Course Note Series 17, 170 p.

Habicht, J.K.A., 1979, Paleoclimate, Paleomagnetism, and Continental Drift: American Association of Petroleum Geologists Studies in Geology No. 9, 31 p.

Issler, D.R., and Snowdon, L.R., 1990, Hydrocarbon generation kinetics and thermal modeling, Beaufort-Mackenzie Basin: Bulletin of Canadian Petroleum Geology, v. 38, p. 1-16.

Lachenbruch, A.H., and Marshall, B.V., 1986, Changing climate: Geothermal evidence from permafrost in the Alaskan arctic: Science, v. 234, p. 689-696.

Lachenbruch, A.H., Greene, G.W., and Marshall, B.V., 1966, Permafrost and the geothermal regimes, in Wilimovsky, N.J., and Wolfe, J.N., eds, Environment of the Cape Thompson region, Alaska: Washington, D.C., U.S. Atomic Energy Commission, Division of Technical Information, P. 149-164.

Lachenbruch, A.H., Sass, J.H., Lawver, L.A., Brewer, M.C., Marshall, B.V., Munroe, R.J., Kennelly, J.P., Galanis, S.P., Moses, T.H., 1988, Temperature and depth of permafrost on the Arctic slope of Alaska, in Gryc, G., ed., Geology and Exploration of the National Petroleum Reserve in Alaska, 1974-1982, U.S. Geological Survey Professional Paper 1399, Ch. 28, p. 645-656.

Lachenbruch, A.H., Sass, J.H., Marshall, B.V., and Moses, T.H., Jr., 1982, Permafrost, heatflow and the geothermal regime at Prudhoe Bay, Alaska: J. Geophysical Research, v. 87, p. 9301-9316.

Lewan, M.D., 1985, Evaluation of petroleum generation by hydrous pyrolysis experimentation, Philosophical Transactions of the Royal Society, v. 315, p. 123-134.

Magoon, L.B., Woodward, P.V., Banet, A.C., Griscom, S.B., Daws, T.A., 1987, Thermal maturity, richness, and type of organic matter of source-rock units, *in* Bird, K.J. and Magoon, L.B., eds., Petroleum geology of the northern part of the Arctic National Wildlife Refuge, Northeastern Alaska: U.S. Geological Survey Bulletin 1778, p. 127-179.

Neglia, S., 1979, Migration of fluids in sedimentary basins, Amer. Assoc. Pet. Geol. Bull., v. 63, p. 573-597.

O'Sullivan, P.B., 1993, Late Mesozoic to Cenozoic thermal and uplift history of the North Slope foreland basin, northern Alaska and northwestern Canada, La Trobe University, Bundoora, Australia, Ph.D thesis, 419 p.

O'Sullivan, P.B., Green, P.F., Bergman, S.C., Decker, J., Duddy, I.R., Gleadow, A.J.W., Turner, D.L., 1993, Multiple phases of Tertiary uplift and erosion in the Arctic National Wildlife Refuge, Alaska, revealed by Apatite fission track analysis: American Association of Petroleum Geologists Bulletin, v. 77, p. 359-385.

Parrish, J.T., and Barron, E.J., 1986, Paleoclimates and Economic Geology: SEPM Short Course Notes No. 18, 162 p.

Robertson, E.C., 1979, Thermal conductivities of rocks, U.S. Geological Survey Open-file Report No. 79-356, 31 p.

Rowan, E. L., Bird, K., Hayba, D., Choueiri, W., Wendebourg, J., Rudkiewicz, J.-L., 1998, Hydrogeologic factors affecting oil migration in the Canning River region, eastern North Slope, Alaska: EOS, Transactions, American Geophysical Union, Fall Meeting, v. 79, p. F844-845.

Scherr, J.M., Banet, S.M., and Bascle, B.J., 1991, Correlation study of selected exploration wells for the North Slope and Beaufort Sea, Alaska: U.S. Minerals Management Service, OCS Report MMS 91-0076, 29 p.

Sweeney, J.J., and Burnham, A.K., 1990, Evaluation of a simple model of vitrinite reflectance based on chemical kinetics, American Association of Petroleum Geologists Bulletin, v. 74, p. 1559-1570.

Yu, Z., and Lerche, I., 1992, An integrated quantitative basin analysis study of the northern part of the Arctic National Wildlife Refuge, northeastern Alaska: J. Geodynamics, v. 15, no. 1/2, p. 107-146.

Click here or on this symbol in the toolbar to return.

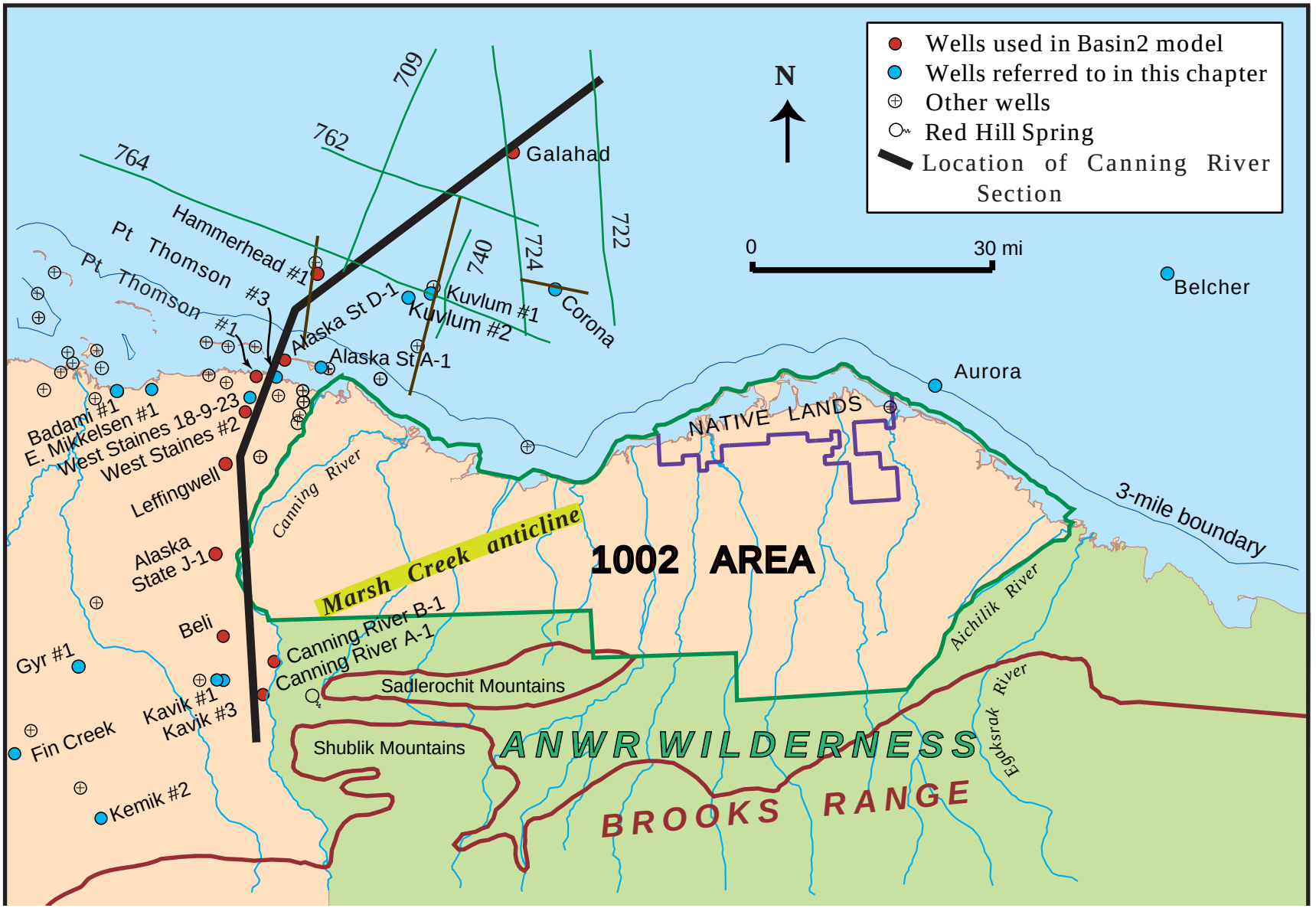

Figure FF1. Regional map showing location of the Canning River Section, the ANWR 1002 Area, seismic lines used in this study, and the locations of key wells (names provided for wells cited in text), Green lines are USGS public domain seismic lines (for provenance of data, see Grantz and others, 1994); and brown lines are published industry lines (Craig and others, 1985; Scherr and others, 1991).

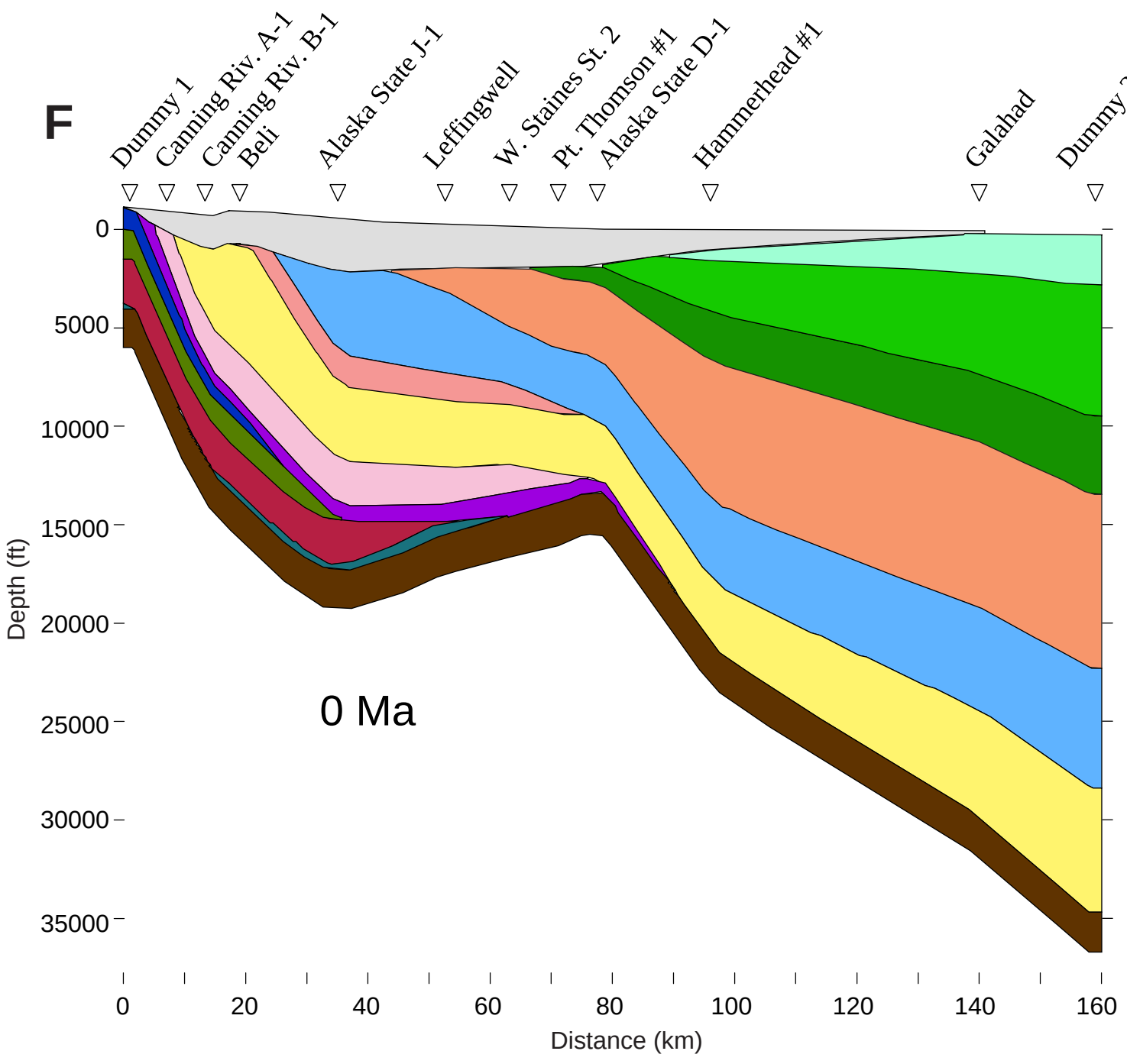

Time-Stratigraphic Units (age at end of deposition)

- Permafrost (0 Ma)
- Pliocene (1Ma)
- Sequence A-up - U. Miocene (5 Ma)
- Sequence A-low - M. Miocene (15 Ma)
- Sequence B - Oligocene (24Ma)
- Sequence C - Eocene (37Ma)
- Sequence D - U. Paleocene (54 Ma)
- Sequence E - L. Paleocene (59 Ma)
- Sequence F - U. Cretaceous (66 Ma)
- Sequence G - Hue, Pebble (74Ma)
- Kingak (134 Ma)
- Sad+Shublik+Sag Riv. (187 Ma)
- Lisburne (275 Ma)
- Endicott (333 Ma)
- Pre- Miss. basement (355 Ma)

Figure FF2 continued.

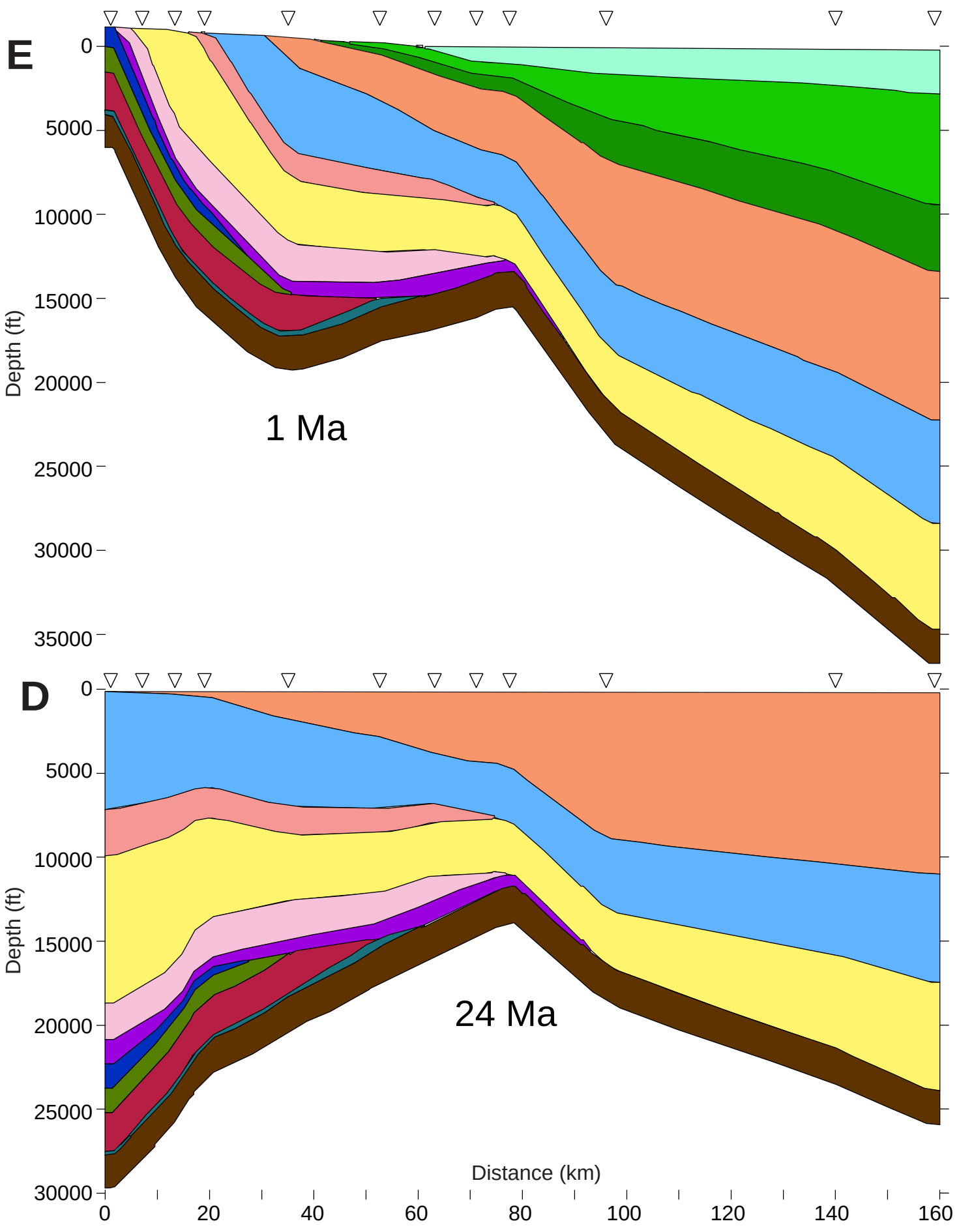

Figure FF2 continued.

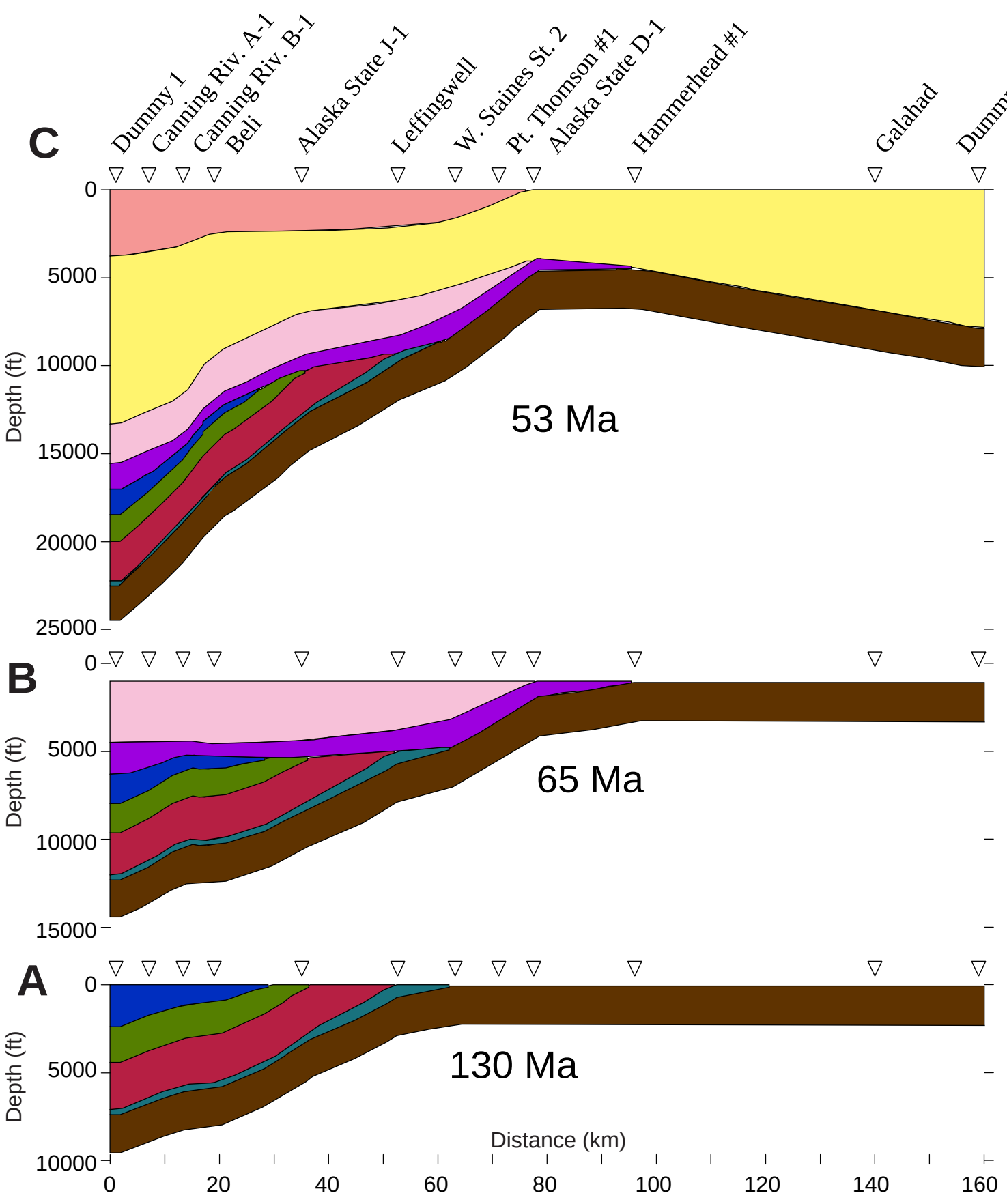

Figure FF2. Stratigraphic evolution of the Canning River Section at six selected times: (A) 130 Ma, (B) 65 Ma, (C) 53 Ma, (D) 24 Ma, (E) 1 Ma, and (F) 0 Ma. See text for discussion and Tables FF2 and FF3 for unit thicknesses and water depths.

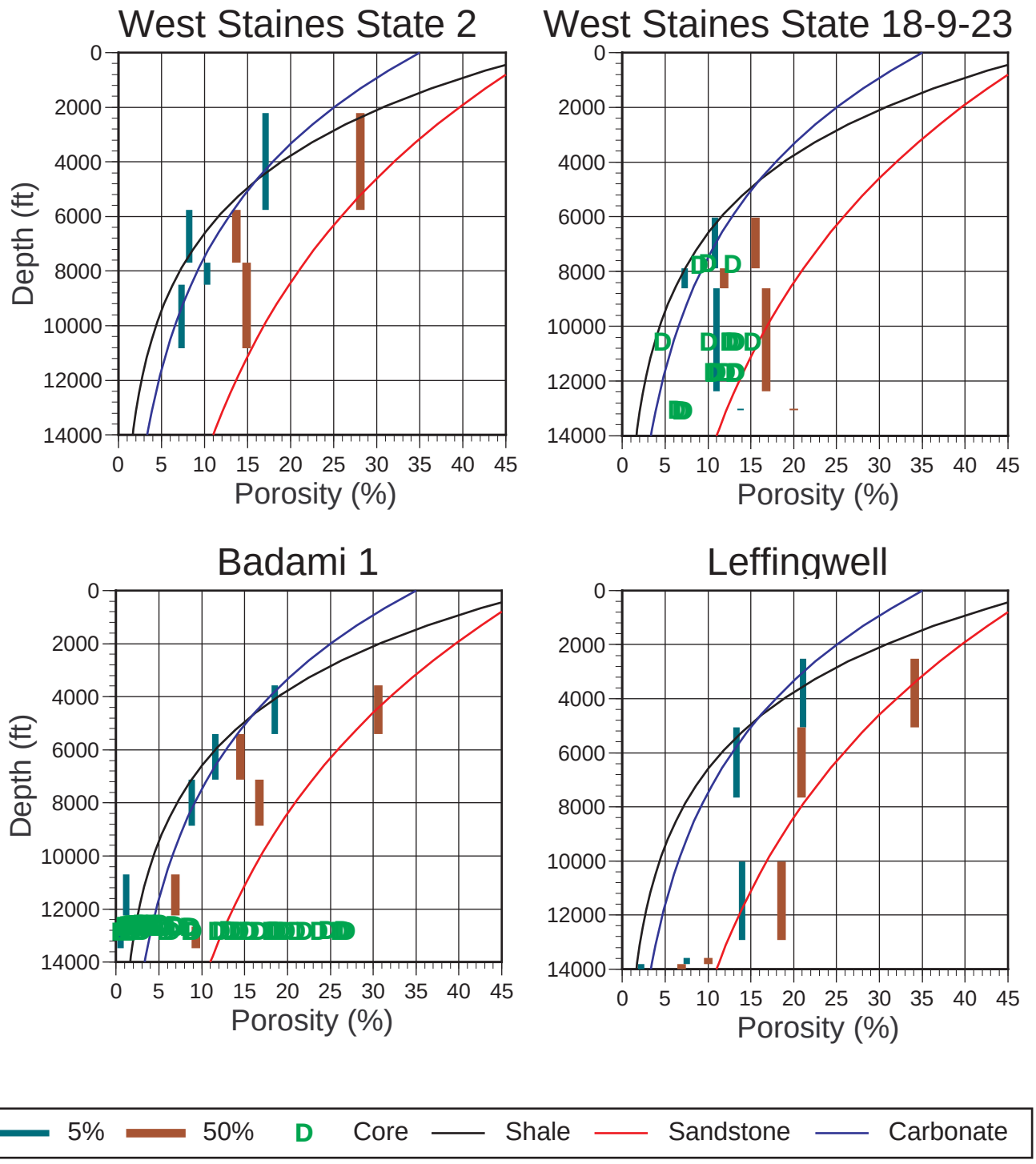

Figure FF3a. Porosity verses depth plots for wells in the Pt. Thomson area. The 5% and 50% bars approximate the shale and sandstone porosities determined from well logs (see text for discussion). The "core" data are from conventional porosity determinations on drill core. The shale, sandstone and carbonate curves show the functions used in our Basin2 model.

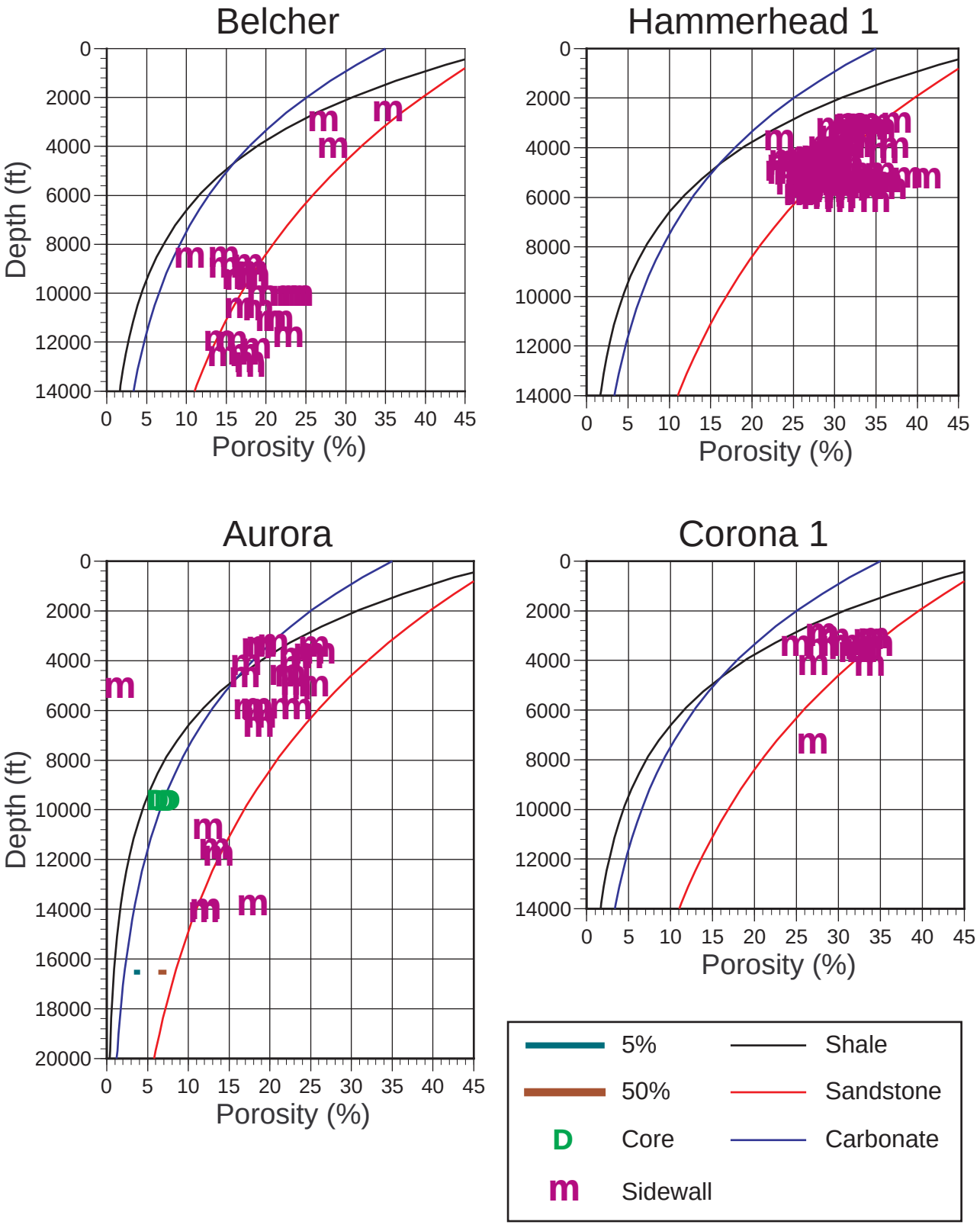

Figure FF3b. Porosity verses depth plots for offshore wells. See Figure FF3a for description of porosity data and Basin2 model parameters.

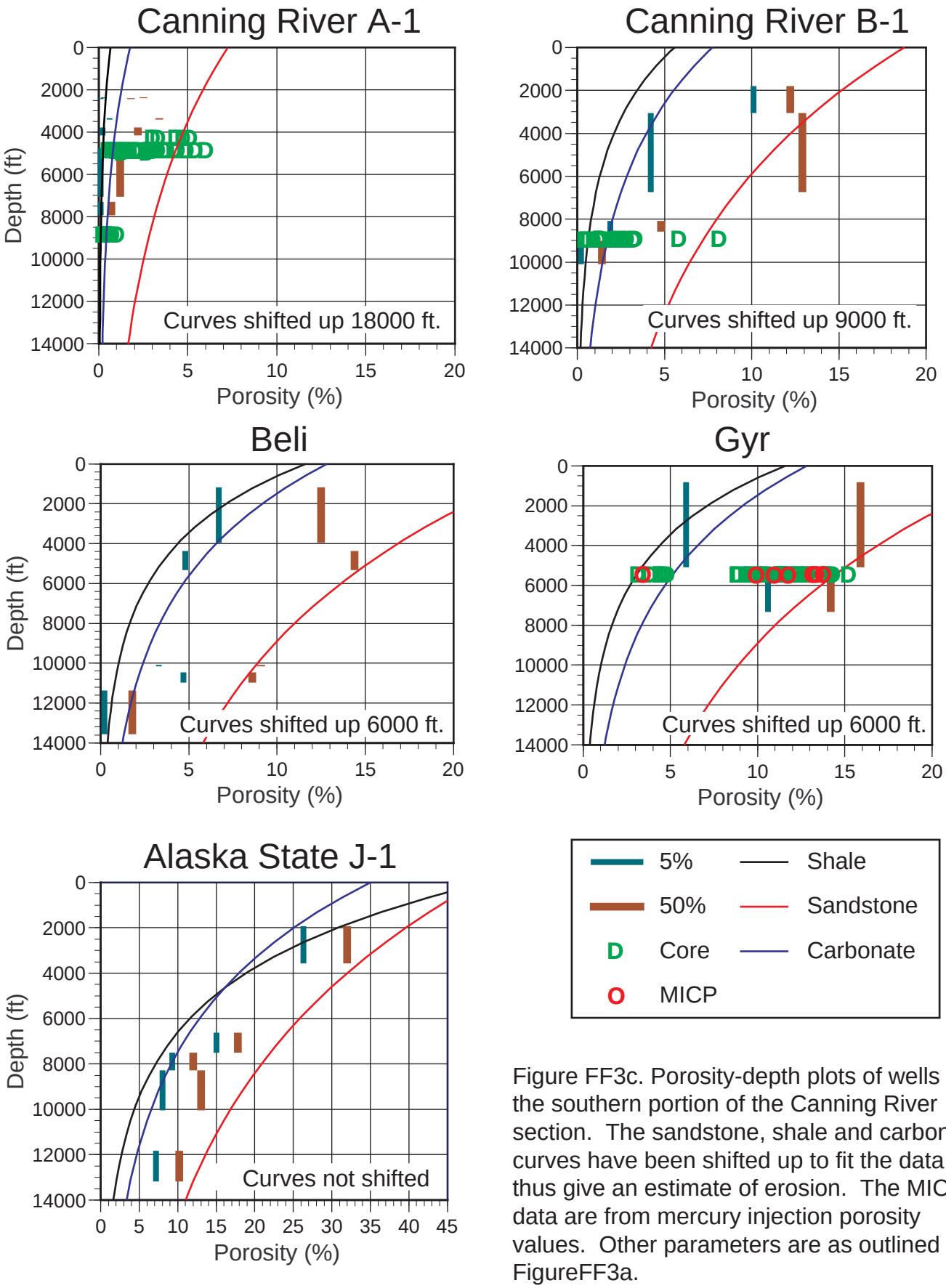

Figure FF3c. Porosity-depth plots of wells from the southern portion of the Canning River section. The sandstone, shale and carbonate curves have been shifted up to fit the data and thus give an estimate of erosion. The MICP data are from mercury injection porosity values. Other parameters are as outlined in FigureFF3a.

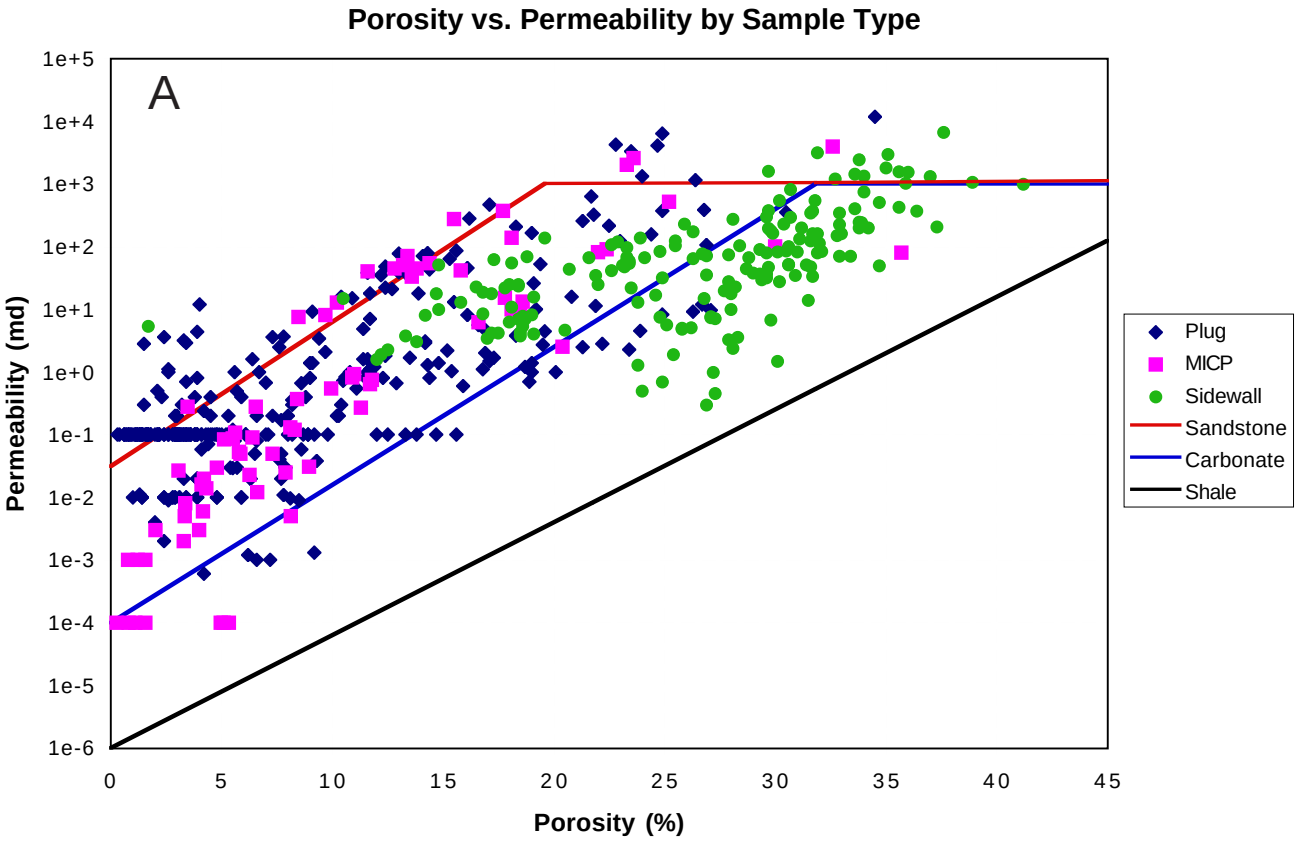

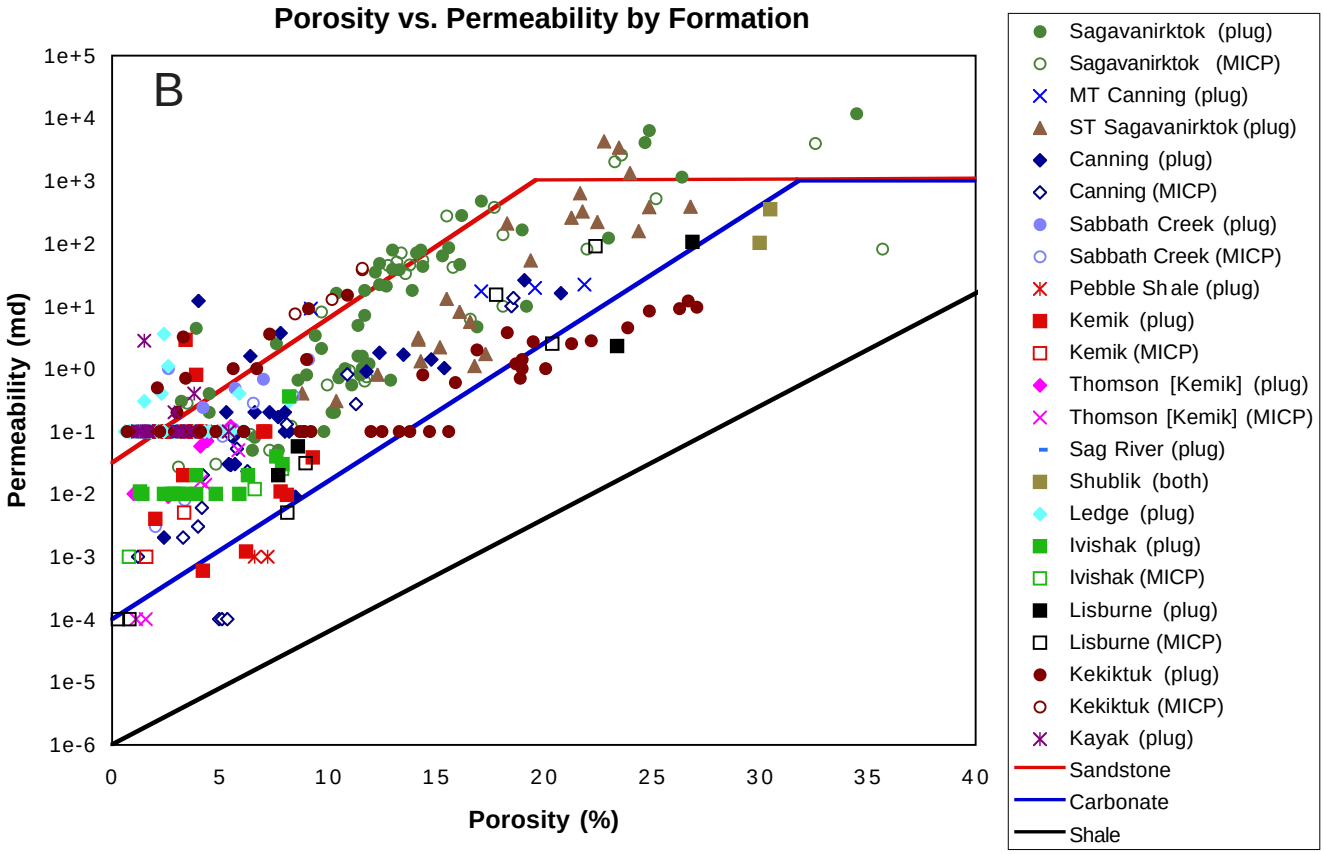

Figure FF4. Porosity versus permeability by (A) sample type and (B) by formation. Note that the data from sidewall cores are not included in the formation plot. The lines represent the functions used in the Basin2 model (see text for discussion).

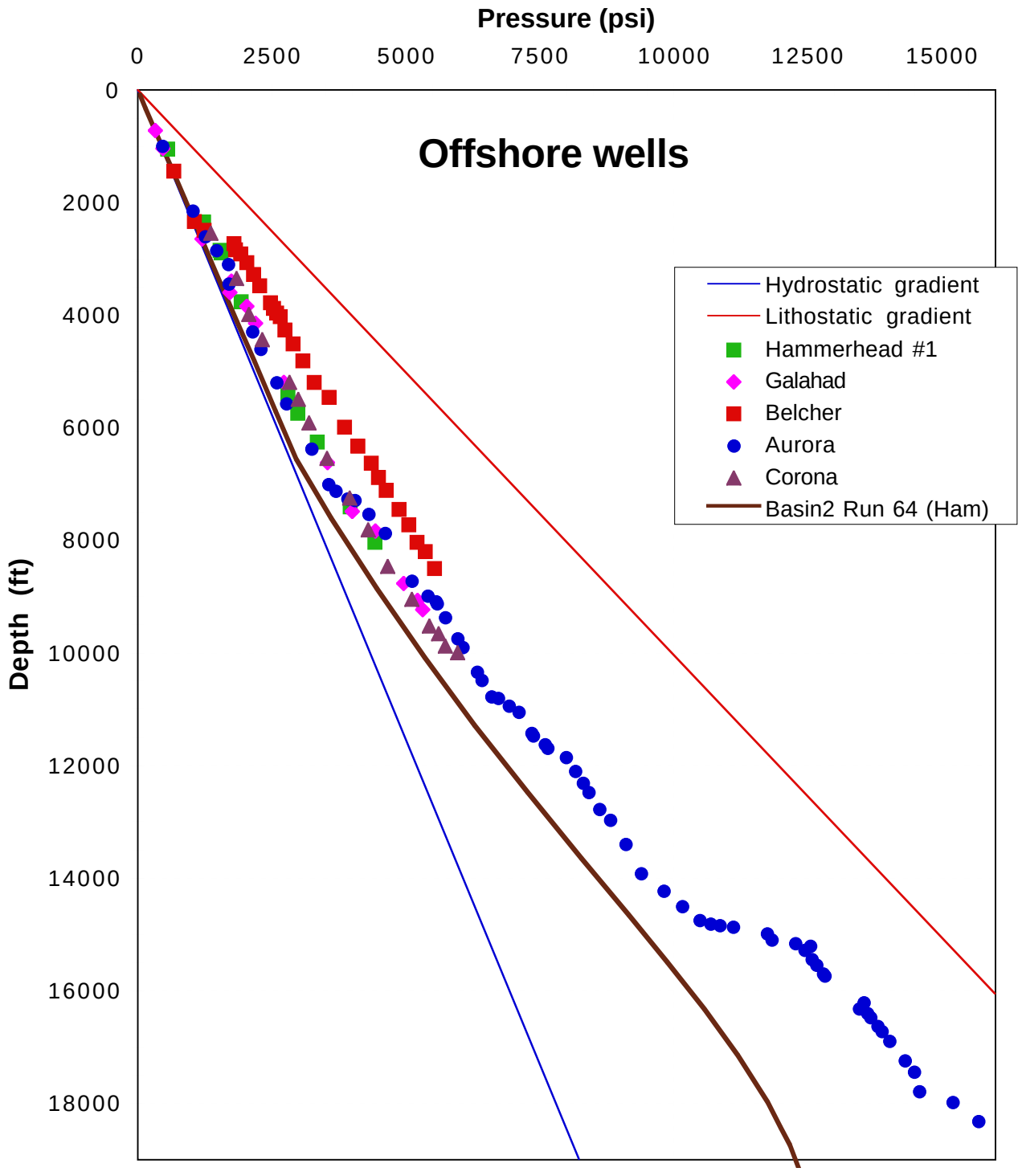

Figure FF5a. Pressure - depth profiles for offshore wells plotted with Basin2 simulated pressure profile for the Hammerhead #1 well. Solid symbols indicate pressure values calculated from drilling mud weights.

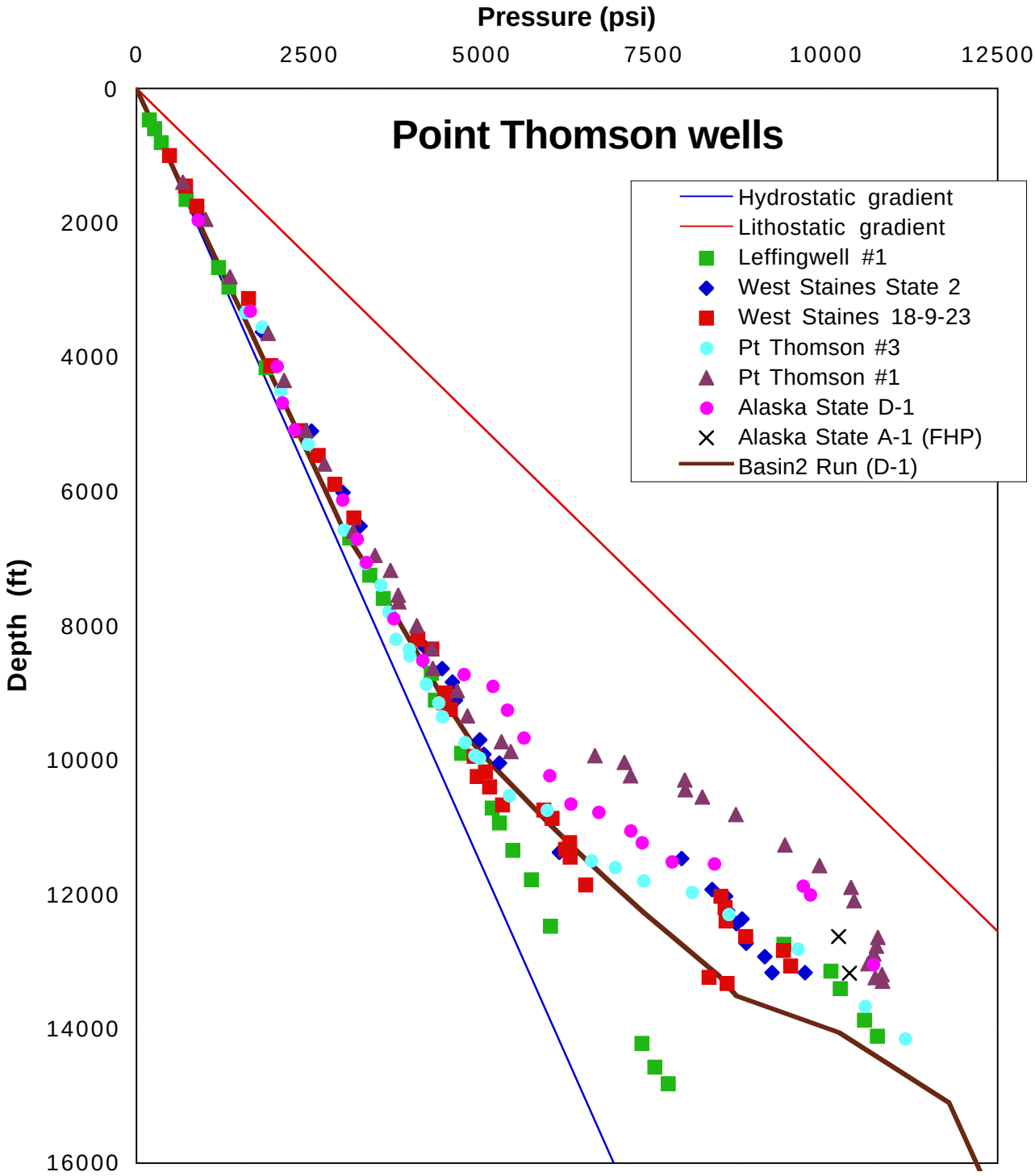

Figure FF5b. Pressure - depth profiles for Point Thomson wells plotted with Basin2 simulated pressure profile for the Alaska State D-1 well. Solid symbols indicate pressure values calculated from drilling mud weights. "FHP" designates that the values are final hydraulic pressures measured during drill stem tests.

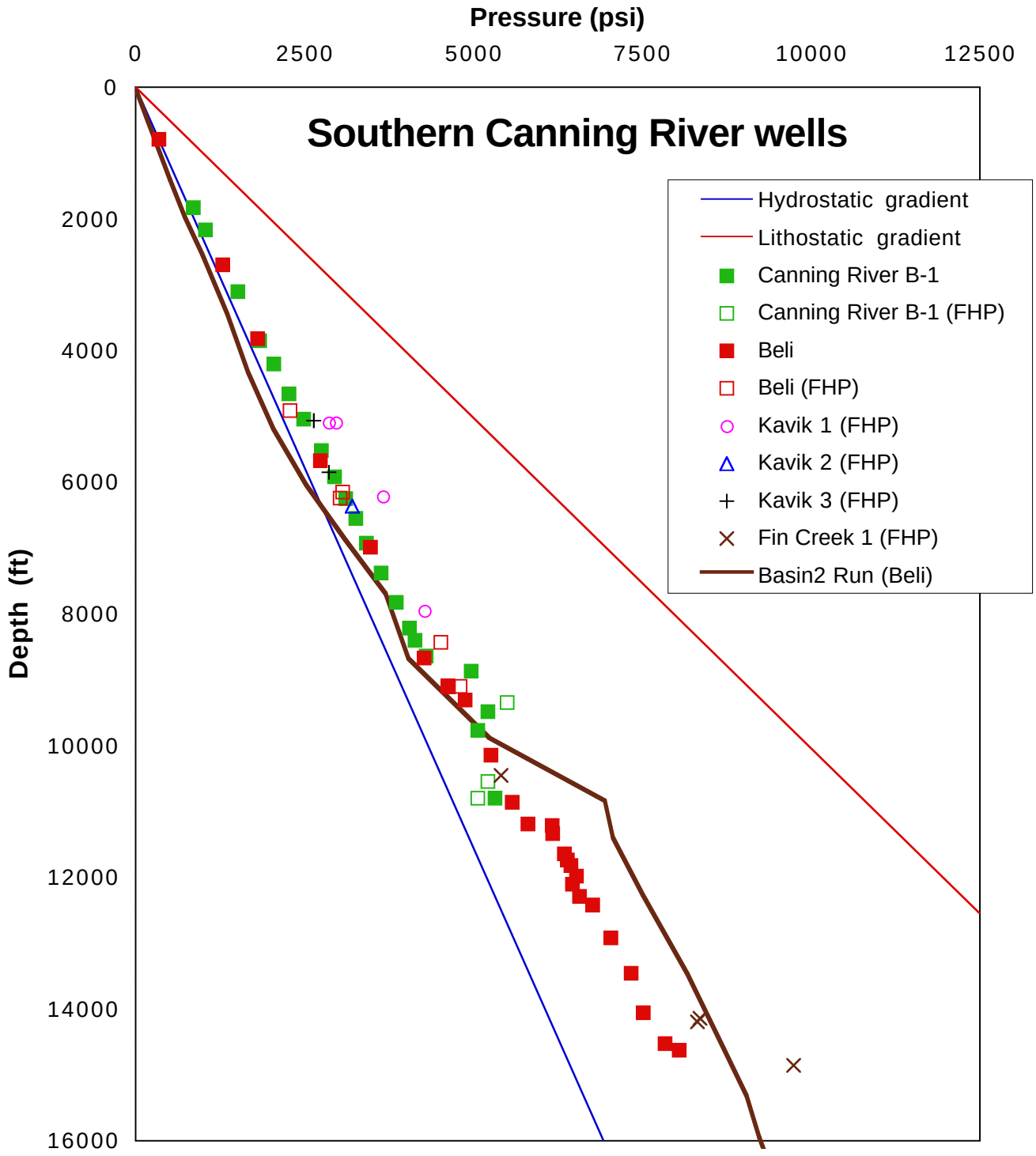

Figure FF5c. Pressure - depth profiles for Southern Canning River wells plotted with Basin2 simulated pressure profile for the Beli well. Solid symbols indicate pressure values calculated from drilling mud weights. "FHP" designates that the values are final hydraulic pressures measured during drill stem tests.

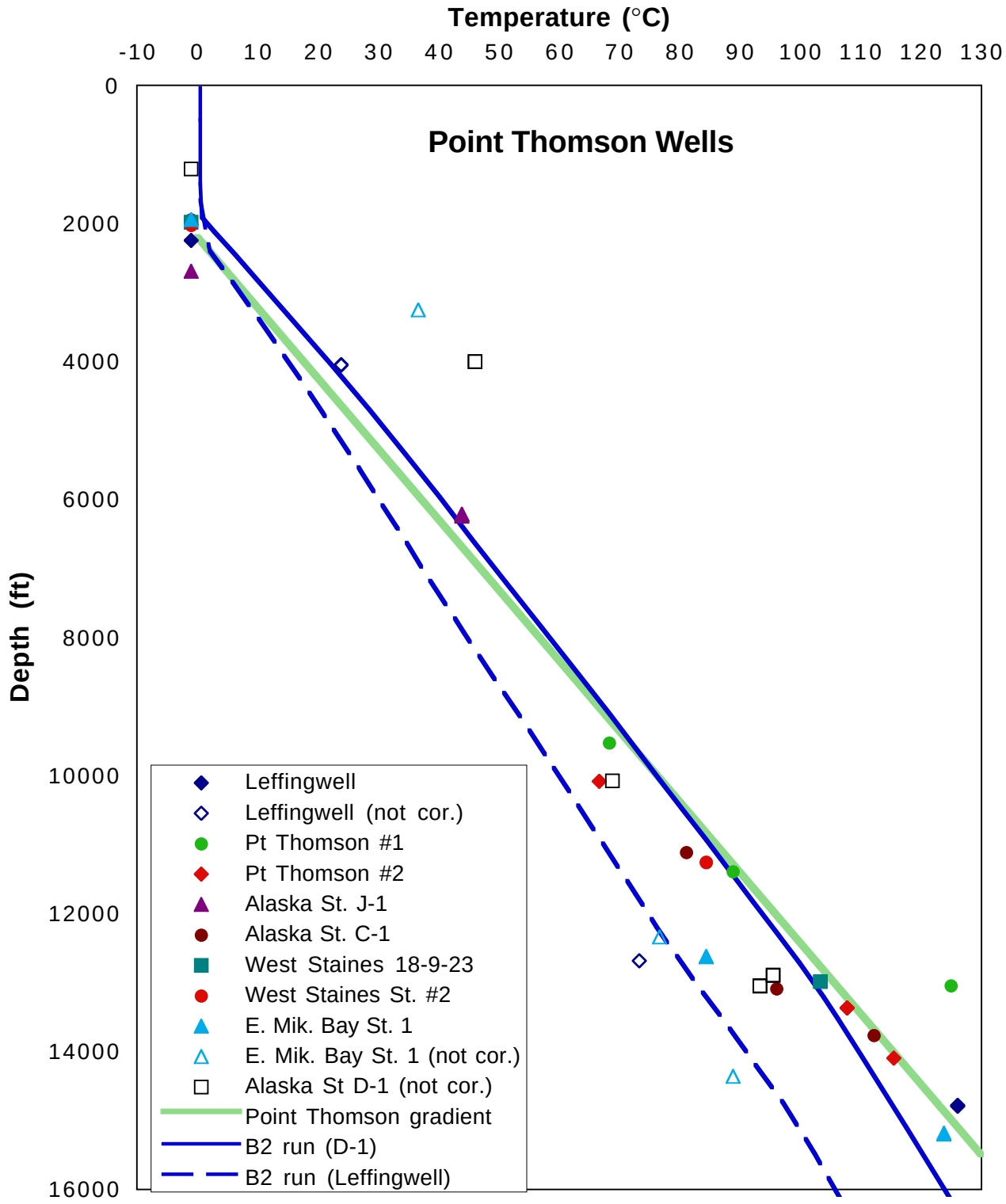

Figure FF6a. Temperature-depth profiles for the wells in the vicinity of Point Thomson. Basin2 simulated temperature profiles are for the Leffingwell and Alaska D-1 wells. Line indicating Point Thomson gradient is an "eye-ball" approximation of data. Open symbols indicate "non-corrected" temperatures.

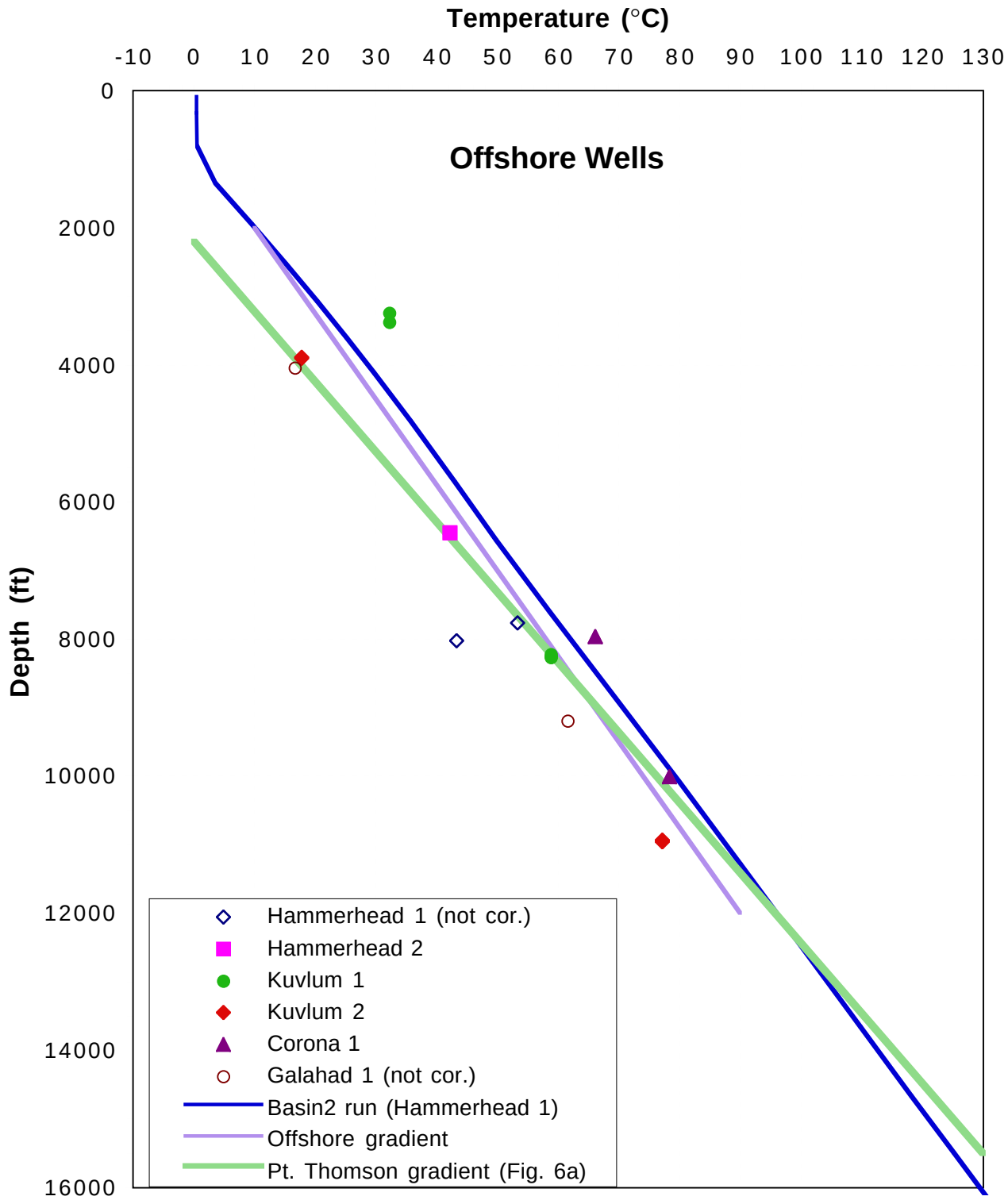

Figure FF6b. Temperature-depth profiles for offshore wells plotted with Basin2 simulated temperatures for Hammerhead #1 well. Line indicating offshore thermal gradient is an "eye-ball" approximation of data. Open symbols indicate "non-corrected" bottom-hole temperature measurements.

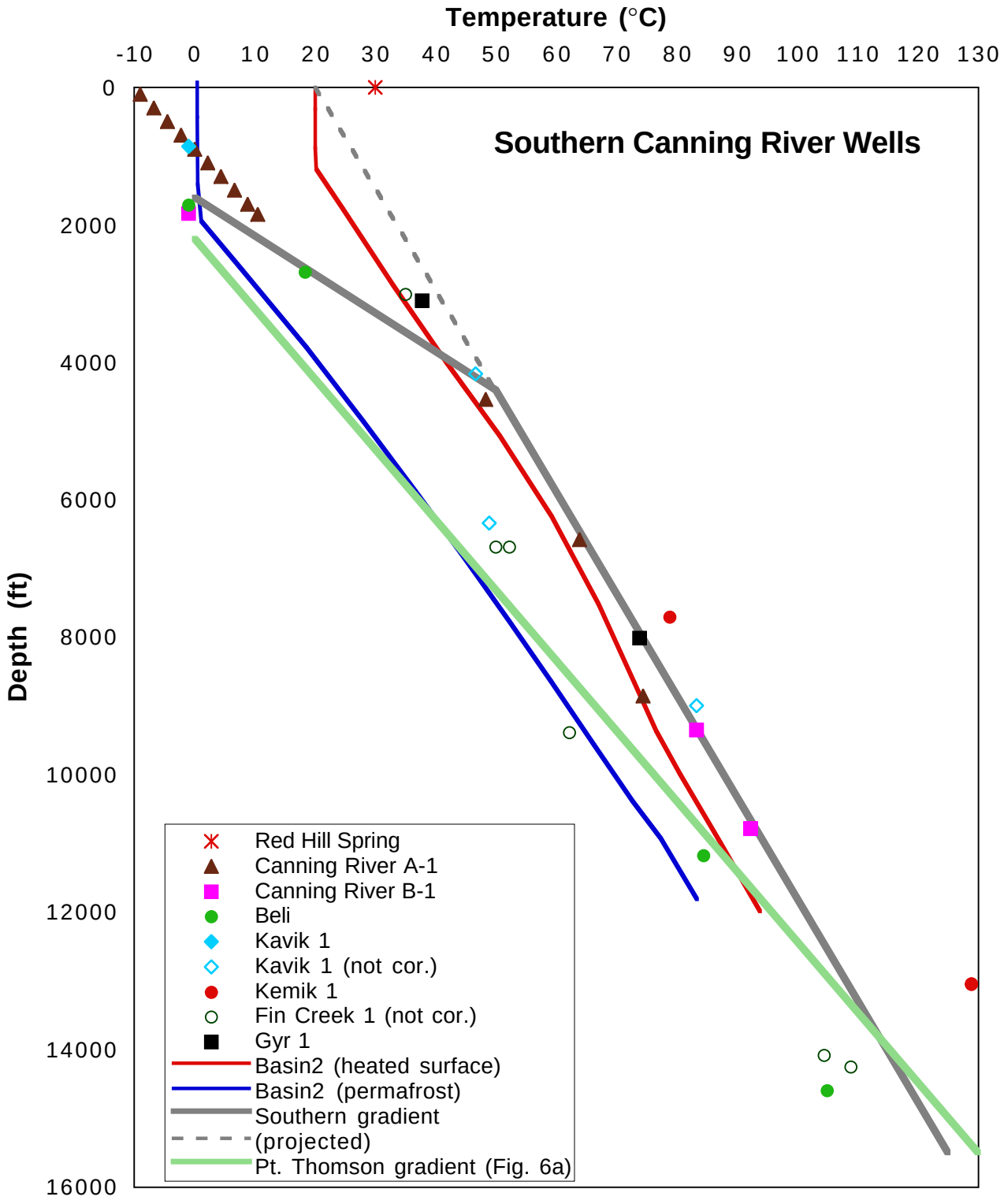

Figure FF6c. Temperature-depth plot for the wells in the Southern Canning River area. Lines indicating thermal gradient are "eye-ball" approximations of the data. Open symbols indicate "non-corrected" down-hole temperature data. See text for discussion of Basin2 results with permafrost and "heated surface" conditions.

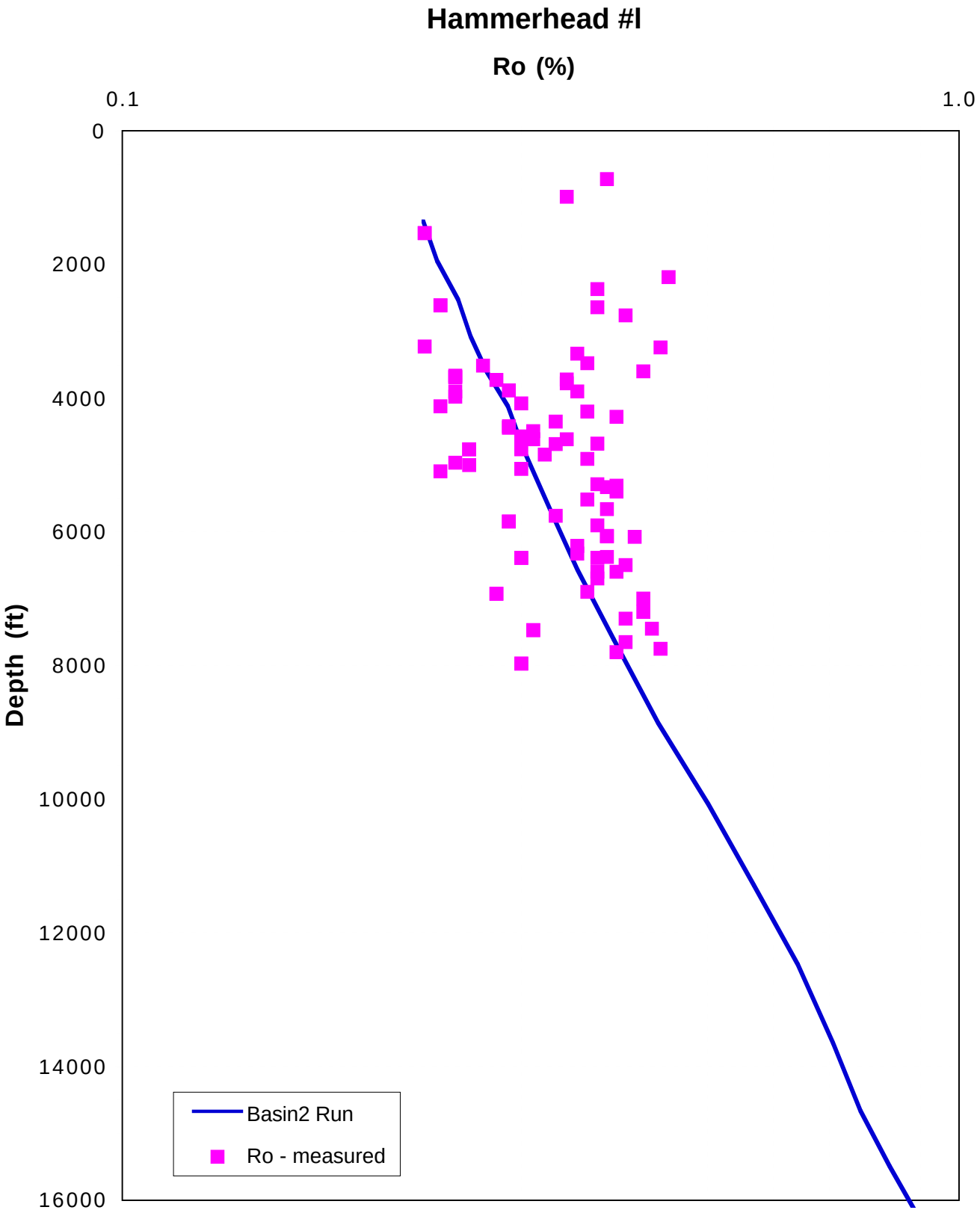

Figure FF7a. Simulated and measured vitrinite reflectance profiles for the Hammerhead #1 well.

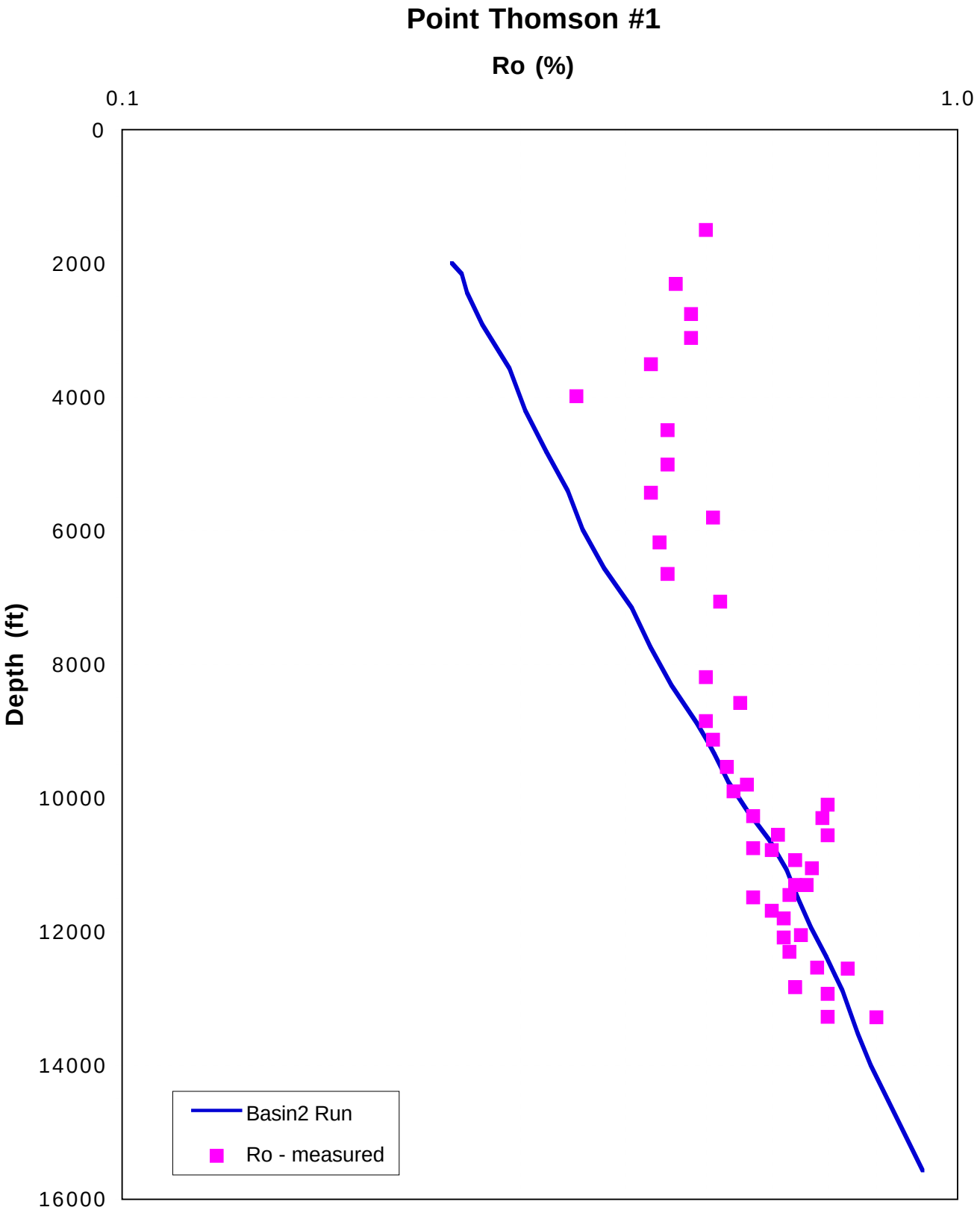

Figure FF7b. Simulated and measured vitrinite reflectance profiles for the Point Thomson #1 well.

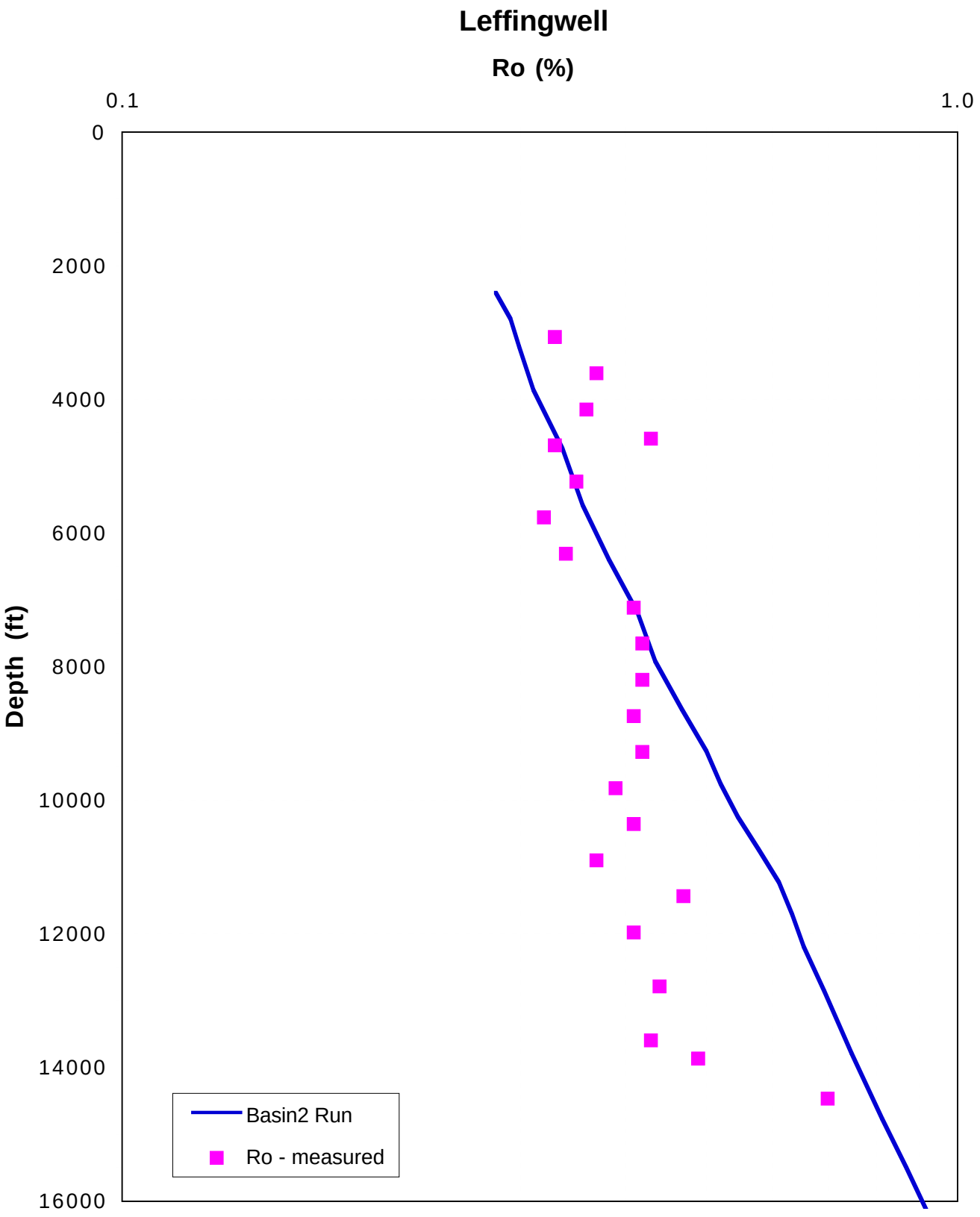

Figure FF7c. Simulated and measured vitrinite reflectance profiles for the Leffingwell well.

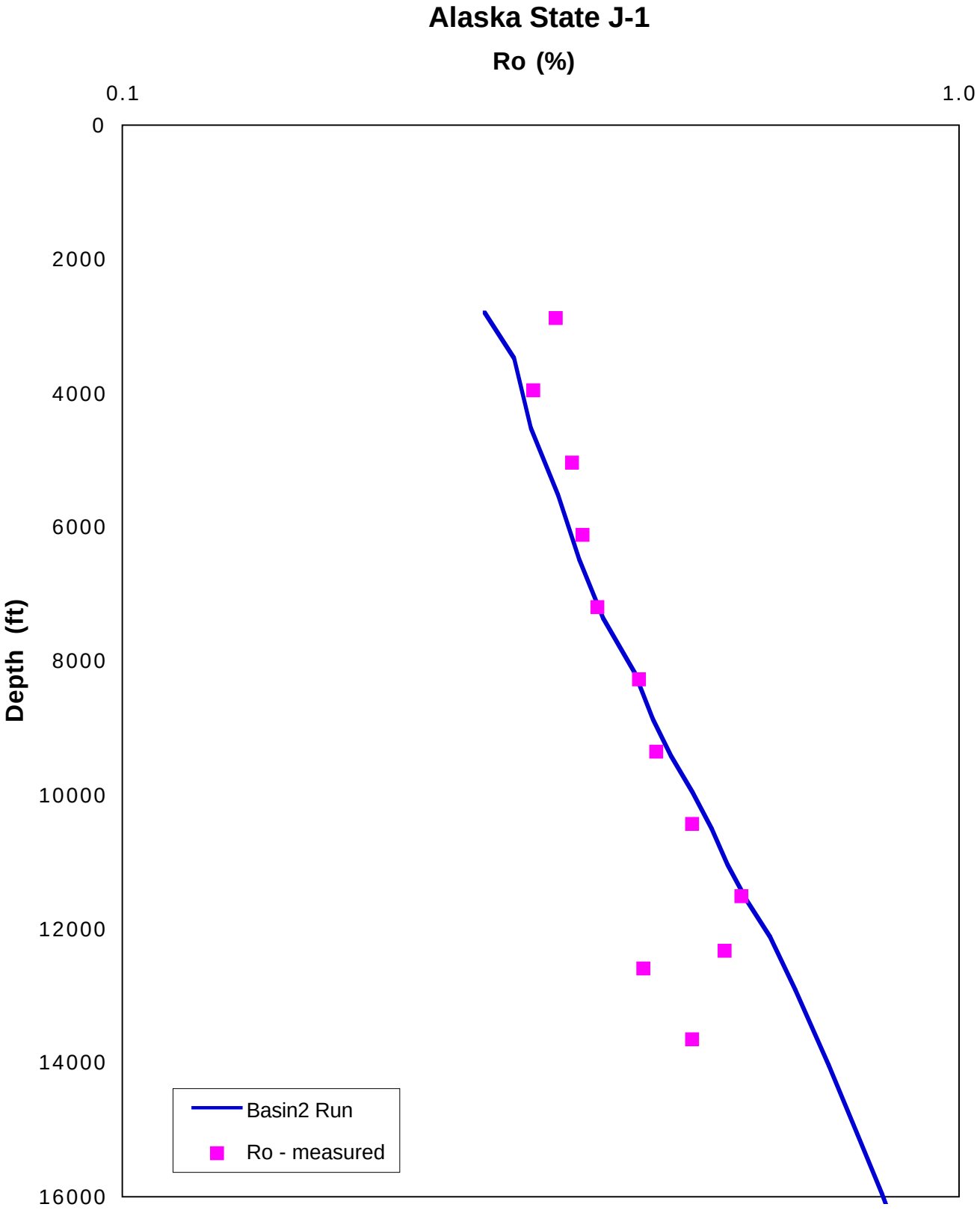

Figure 7d. Simulated and measured vitrinite reflectance profiles for the Alaska State J-1 well.

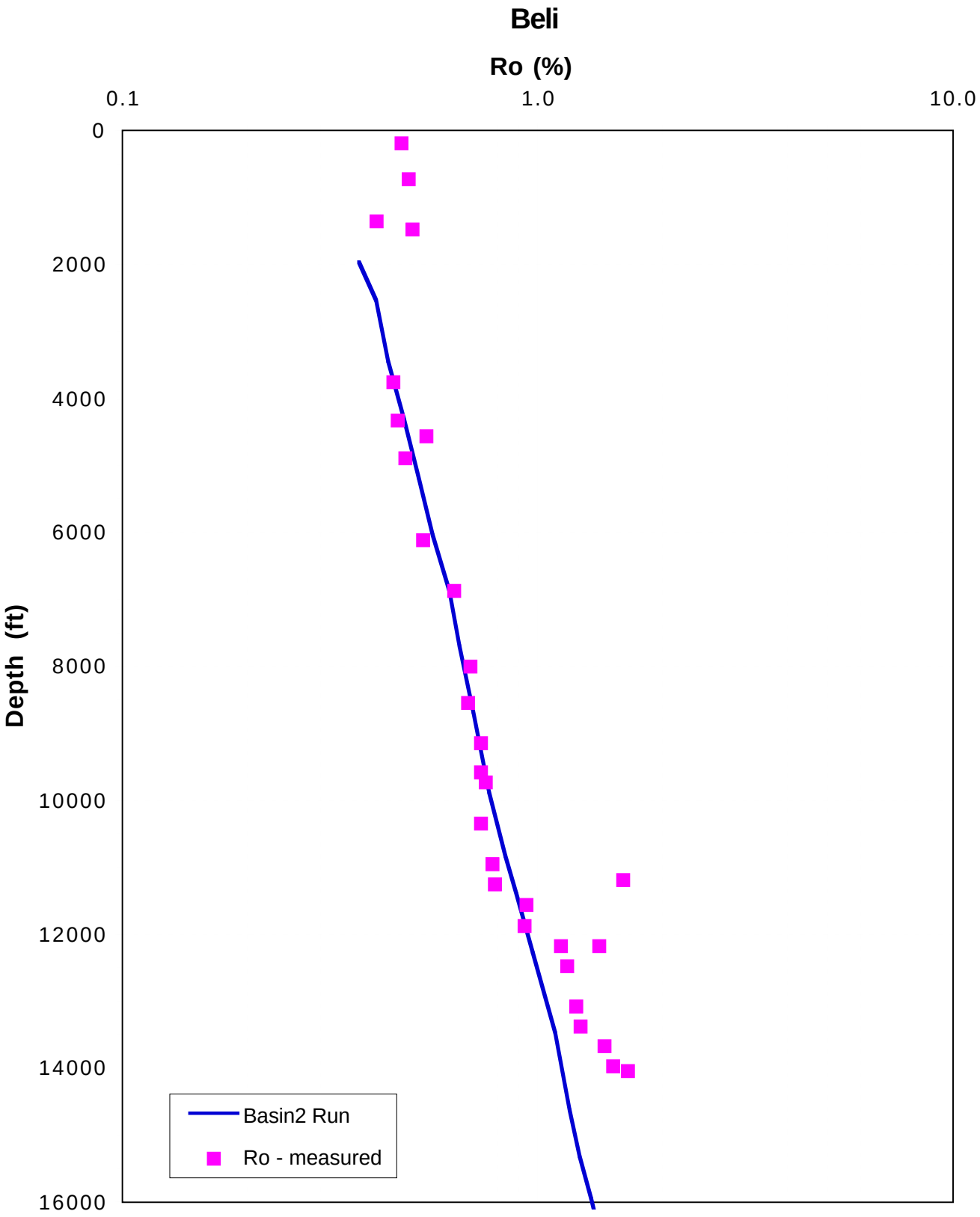

Figure FF7e. Simulated and measured vitrinite reflectance profiles for the Beli well.

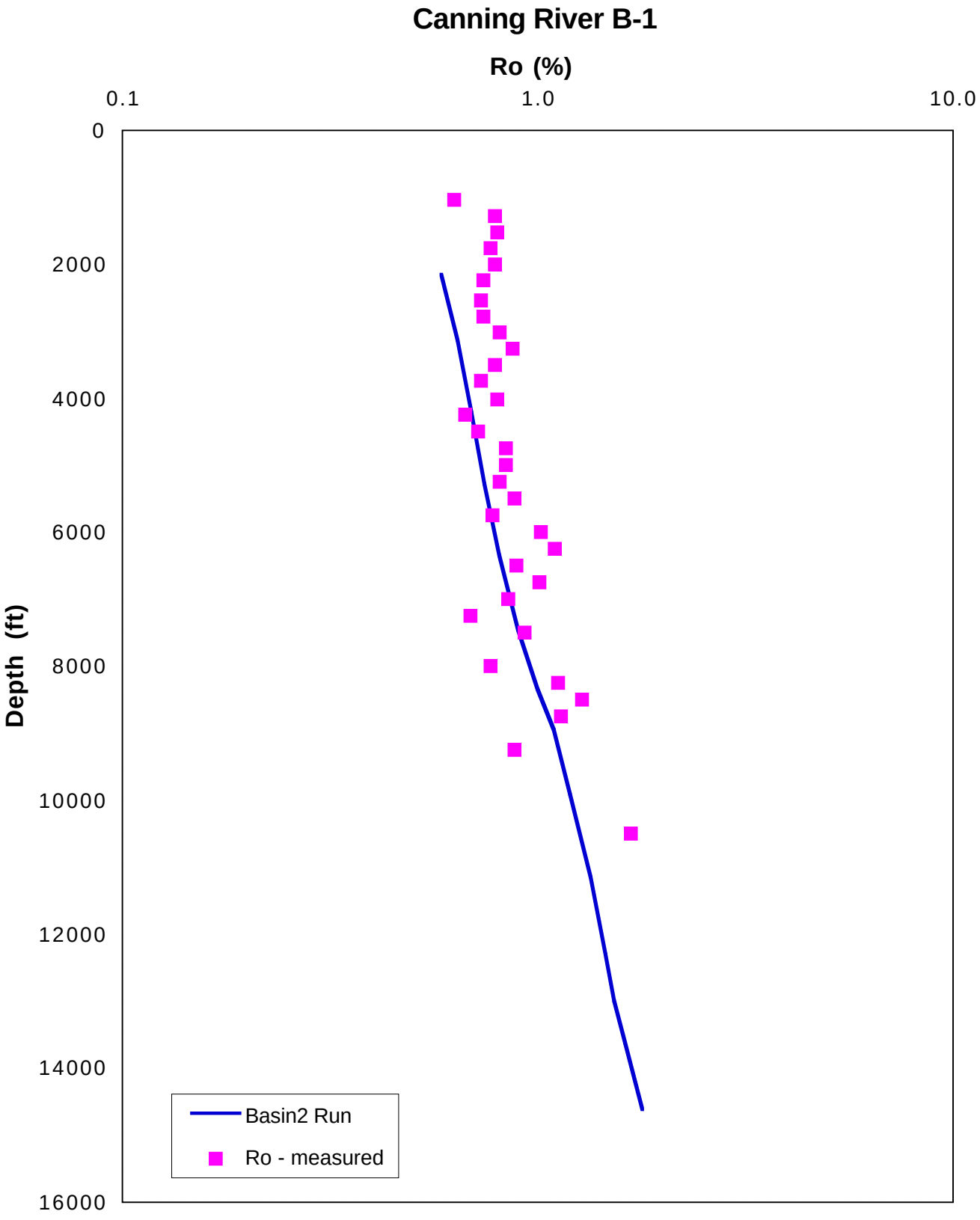

Figure FF7f. Simulated and measured vitrinite reflectance profiles for the Canning River B-1 well.

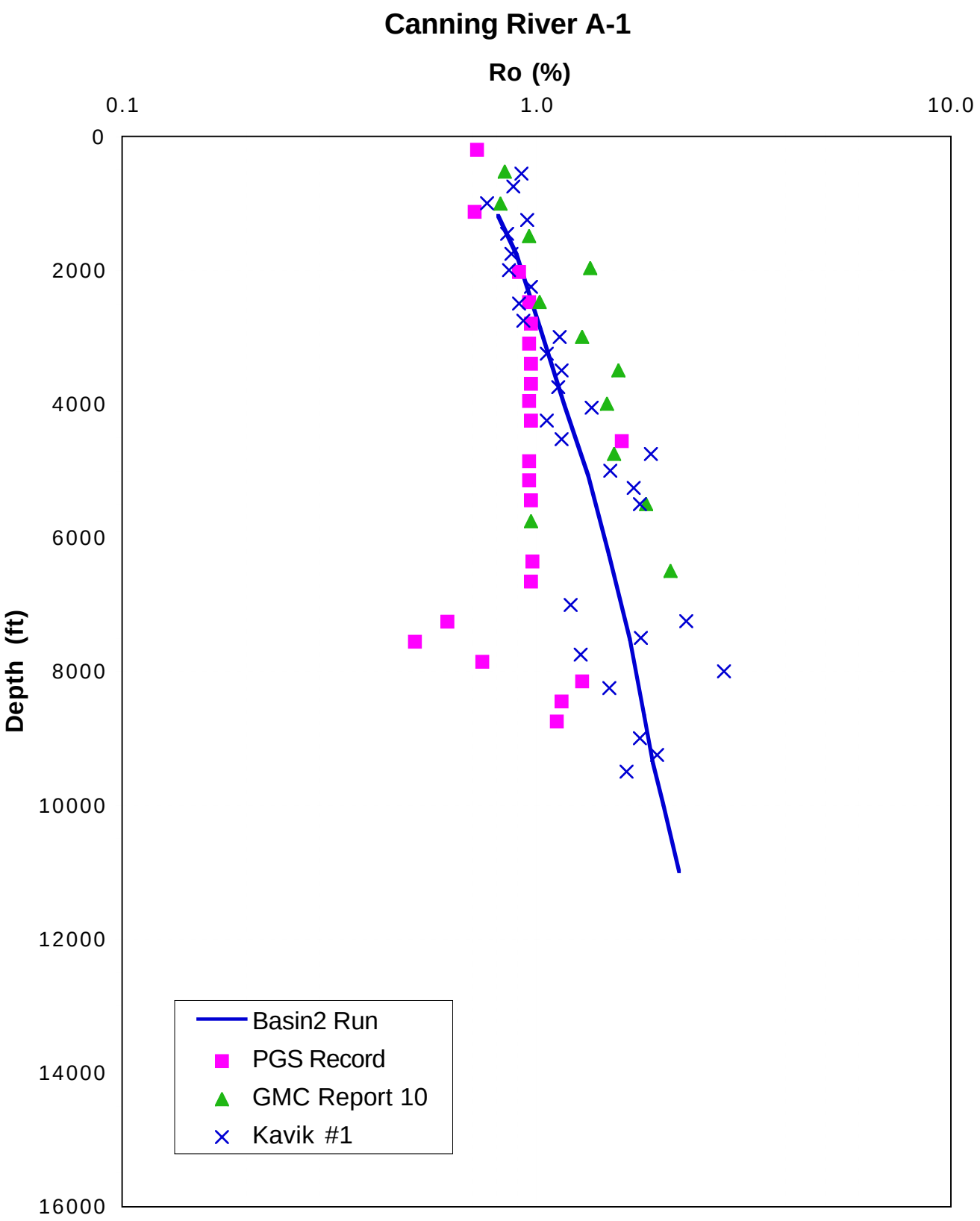

Figure FF7g. Simulated and measured vitrinite reflectance profiles for the Canning River A-1 well. See text for discussion of different data sets.

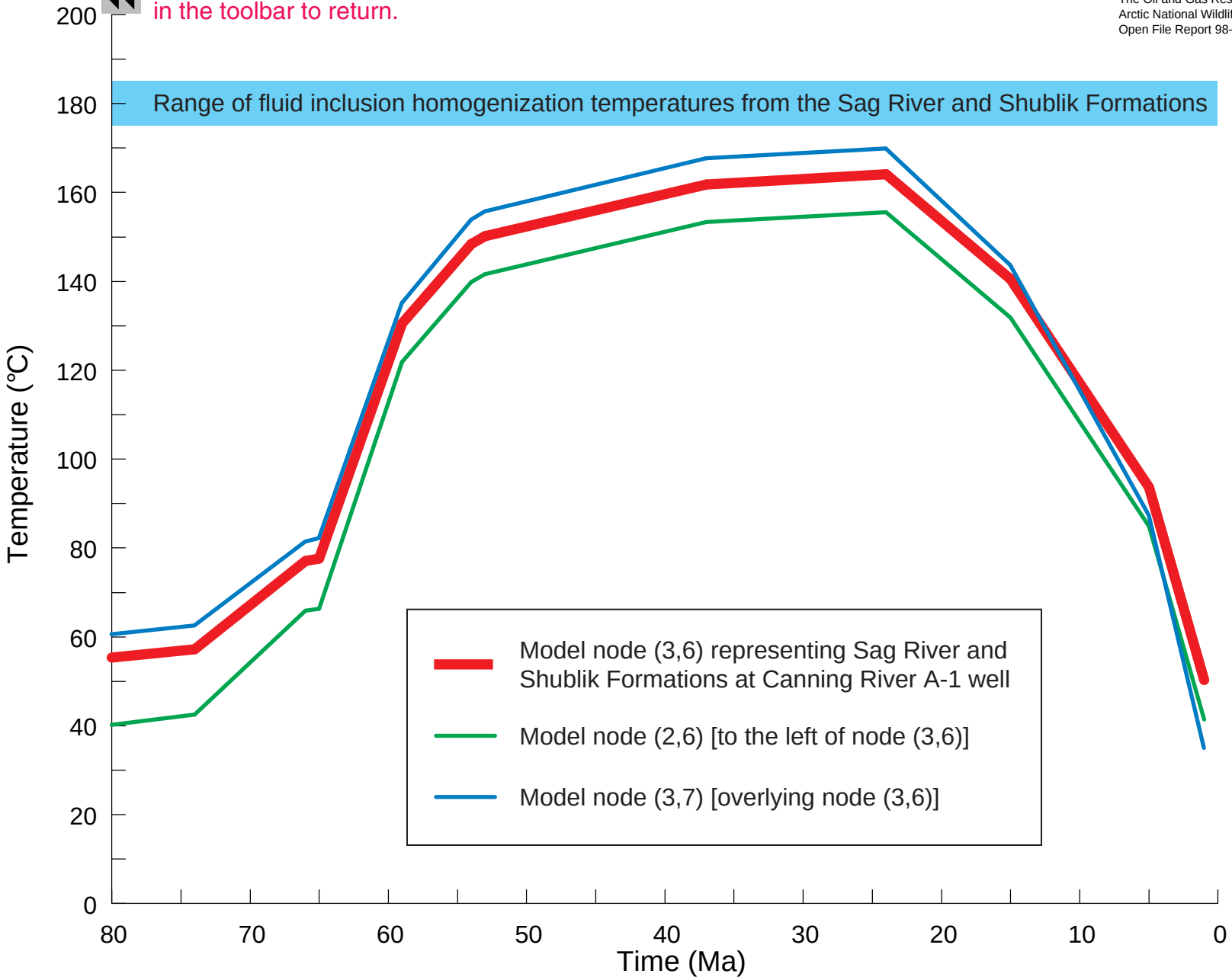

Figure FF8. Thermal history of location (node) in model that roughly corresponds to the fluid inclusion sample localities in the Kavik 3 well. This well is approximately 5 km west of the Canning River A-1 well. Blue field shows temperature range (175-185 °C) of fluid inclusion data from quartz and calcite in the Sag River and Shublik Formations analyzed by Burruss (Chap. FI, Table FI2). Thermal histories of two adjacent nodes represent the approximate uncertainty in temperature due to sample location.

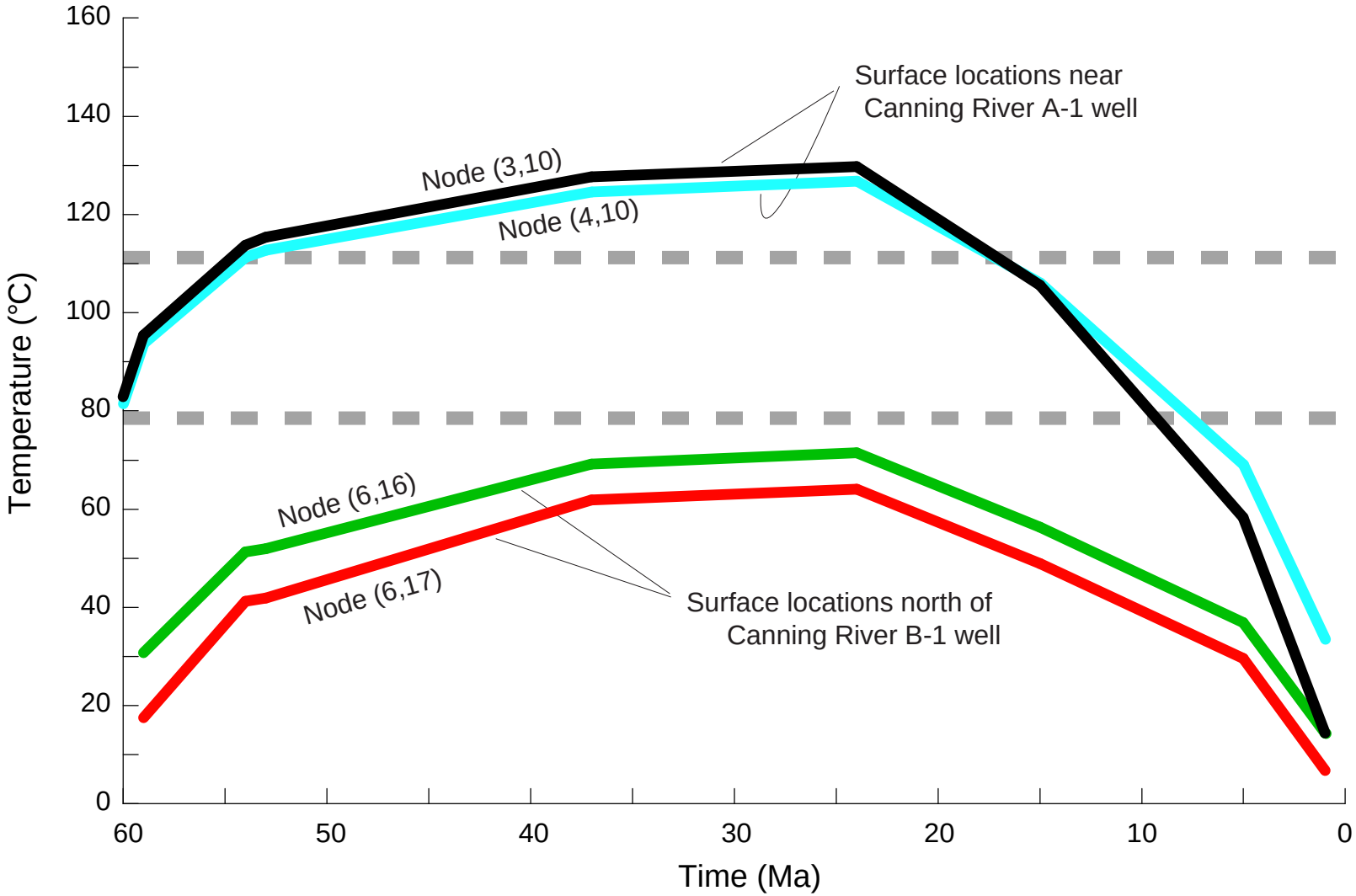

Figure FF9. Thermal histories of locations (nodes) in model that roughly corresponds to the apatite fission track sample localities in the vicinity of the Canning River A-1 and B-1 wells. Analyses by O'Sullivan and others (1993) indicate temperatures of less than 80 °C for a surface sample north of the Canning River B-1 well and temperatures of greater than 110 °C for surface samples near the Canning River A-1 well. See text for discussion.

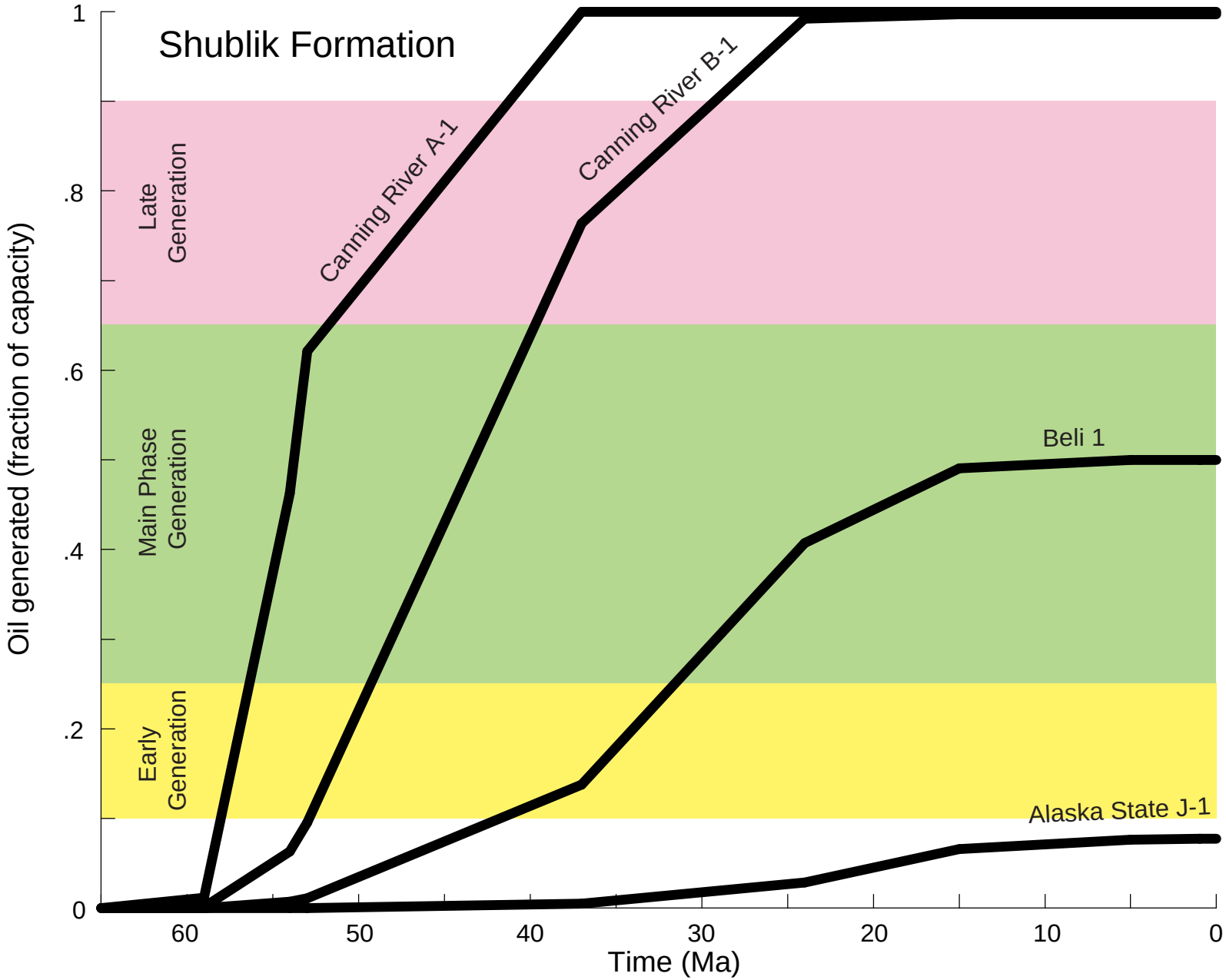

Figure FF10a. Hydrocarbon generation history of the Shublik Formation at 4 selected localities along the Canning River section. Plot shows the fraction of oil generated by the Shublik Formation relative to its capacity. See Table FF6 for the kinetic constants used in the Arrhenius equation described by Lewan (1985). Note that the Alaska State J-1 well does not penetrate this unit and is used only to indicate sample location.

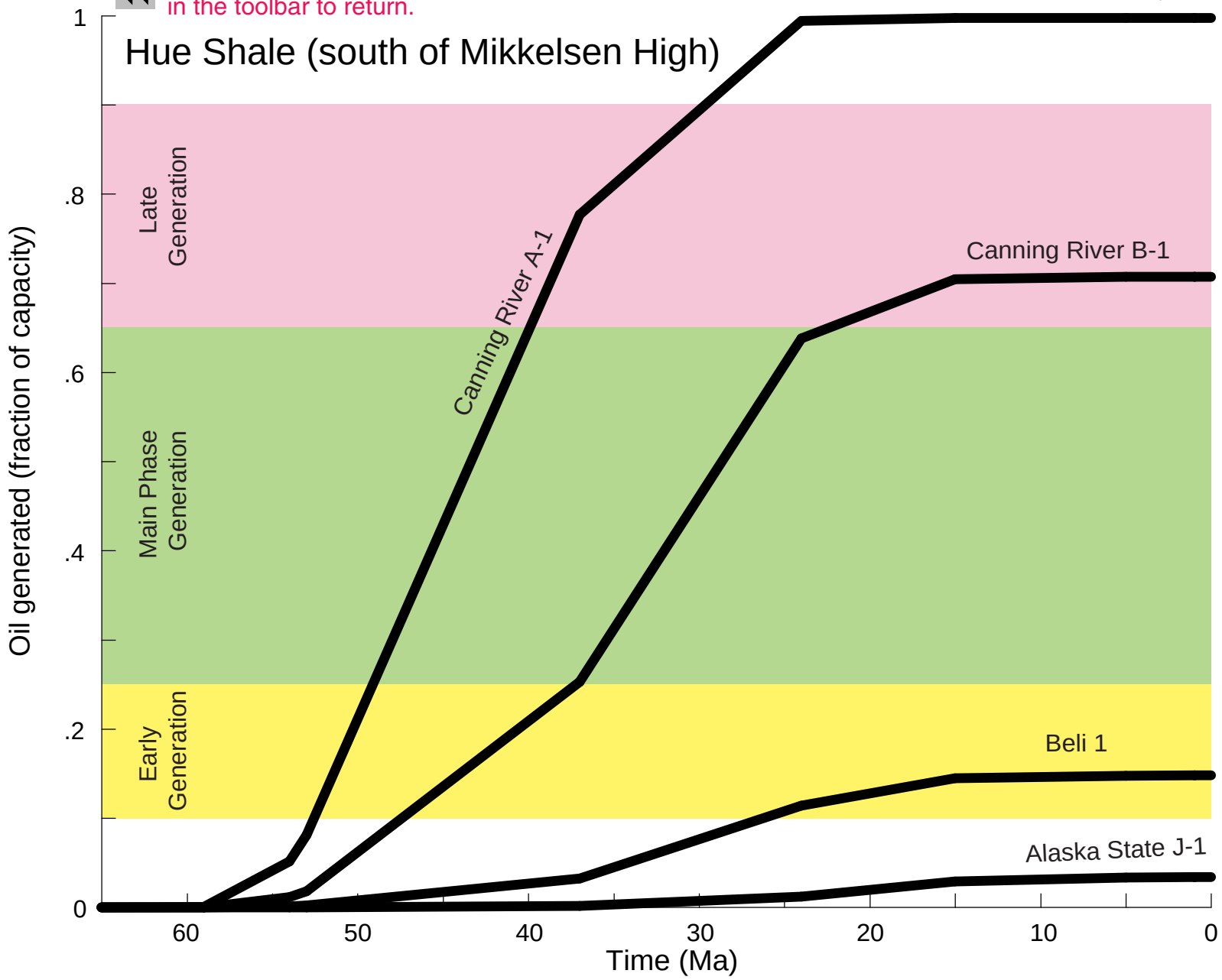

Figure FF10b. Hydrocarbon generation history of the Hue Shale at 4 selected localities south of the Mikkelsen High. Plot shows the fraction of oil generated by the Hue Shale relative to its capacity. See Table FF6 for the kinetic constants used in the Arrhenius equation described by Lewan (1985). Note that the Alaska State J-1 well does not penetrate this unit and is used only to indicate sample location.

Click here or on this symbol
in the toolbar to return.

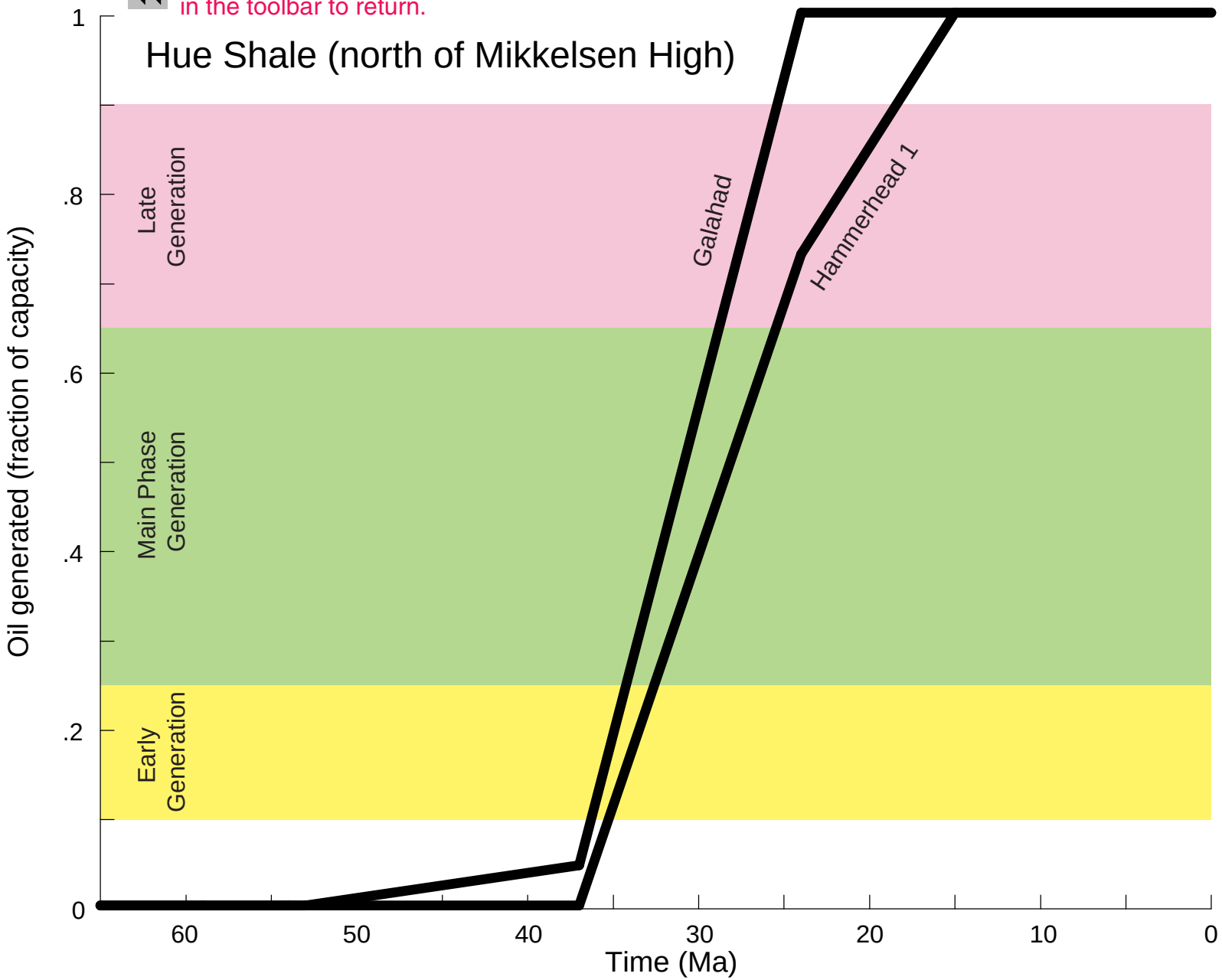

Figure FF10c. Hydrocarbon generation history of the Hue Shale at 2 selected localities north of the Mikkelsen High. Plot shows the fraction of oil generated by the Hue Shale relative to its capacity. See Table FF6 for the kinetic constants used in the Arrhenius equation described by Lewan (1985). Note that the wells do not penetrate this unit offshore and are used only to indicate sample location.

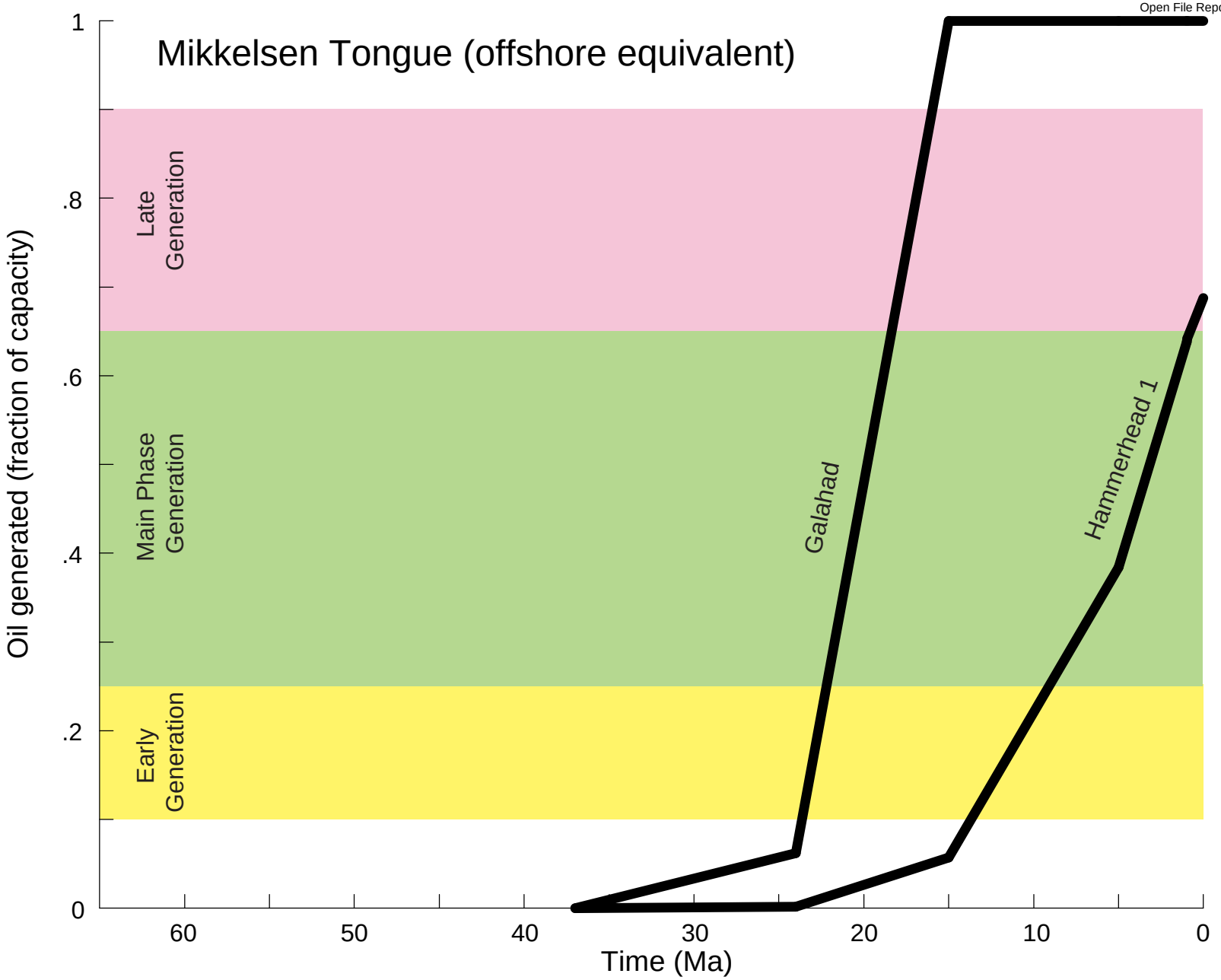

Figure FF10d. Hydrocarbon generation history of the lateral offshore equivalent of the Mikkelsen Tongue of the Canning Formation at 2 selected localities. Plot shows the fraction of oil generated by the Mikkelsen Tongue relative to its capacity. See Table FF6 for the kinetic constants used in the Arrhenius equation described by Lewan (1985). Note that the wells do not penetrate this unit offshore and are used only to indicate sample location.

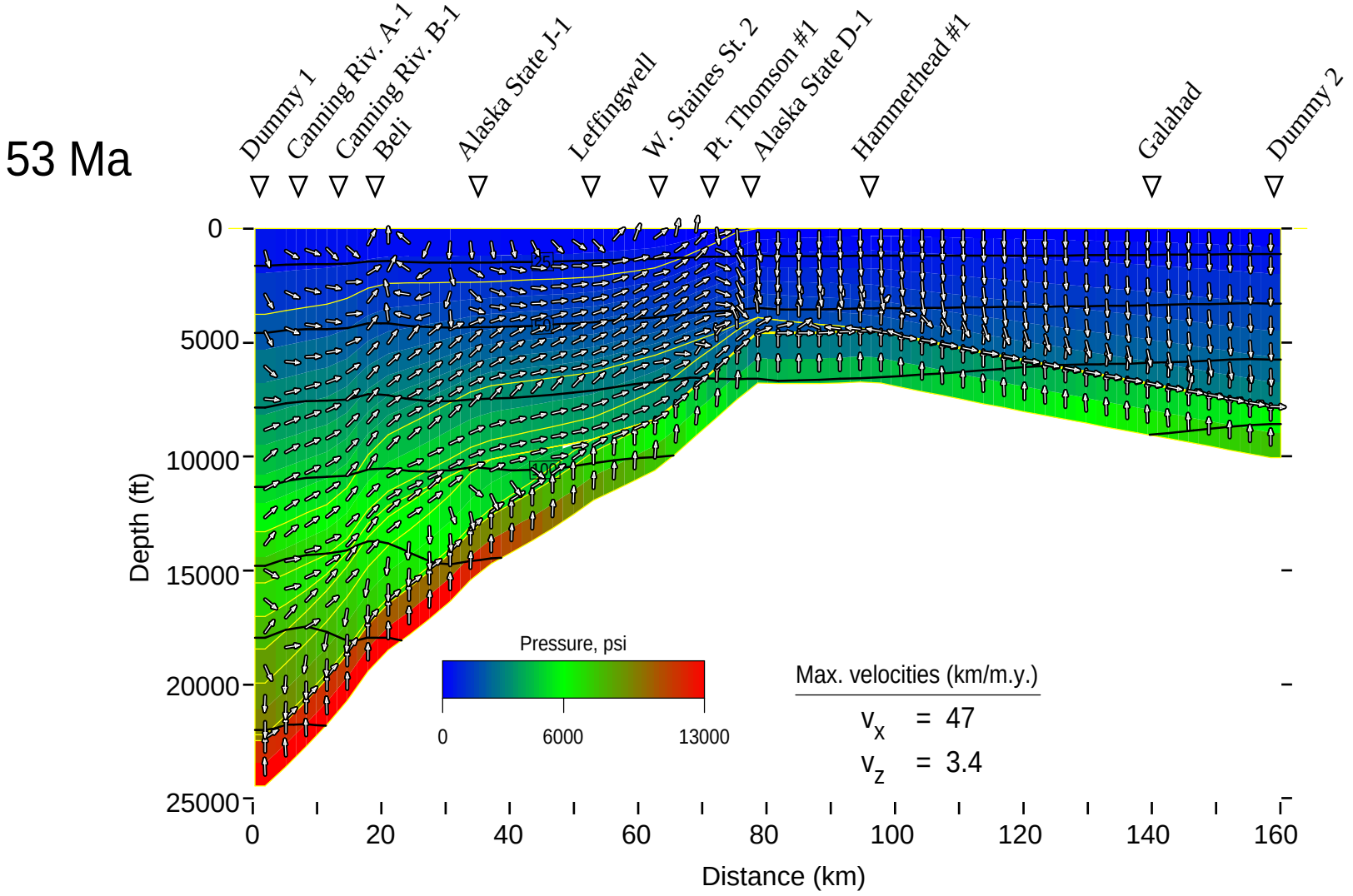

Figure FF11a. Simulation results at 53 Ma showing fluid flow directions, and pressure and temperature distributions. Flow vectors show direction only and do not imply magnitude. Maximum flow velocities are for comparison with other time slices. Pressure distribution is shown by color scale and temperatures are contoured at 25 °C intervals. Yellow lines show time-stratigraphic units (see Fig. FF2).

37 Ma

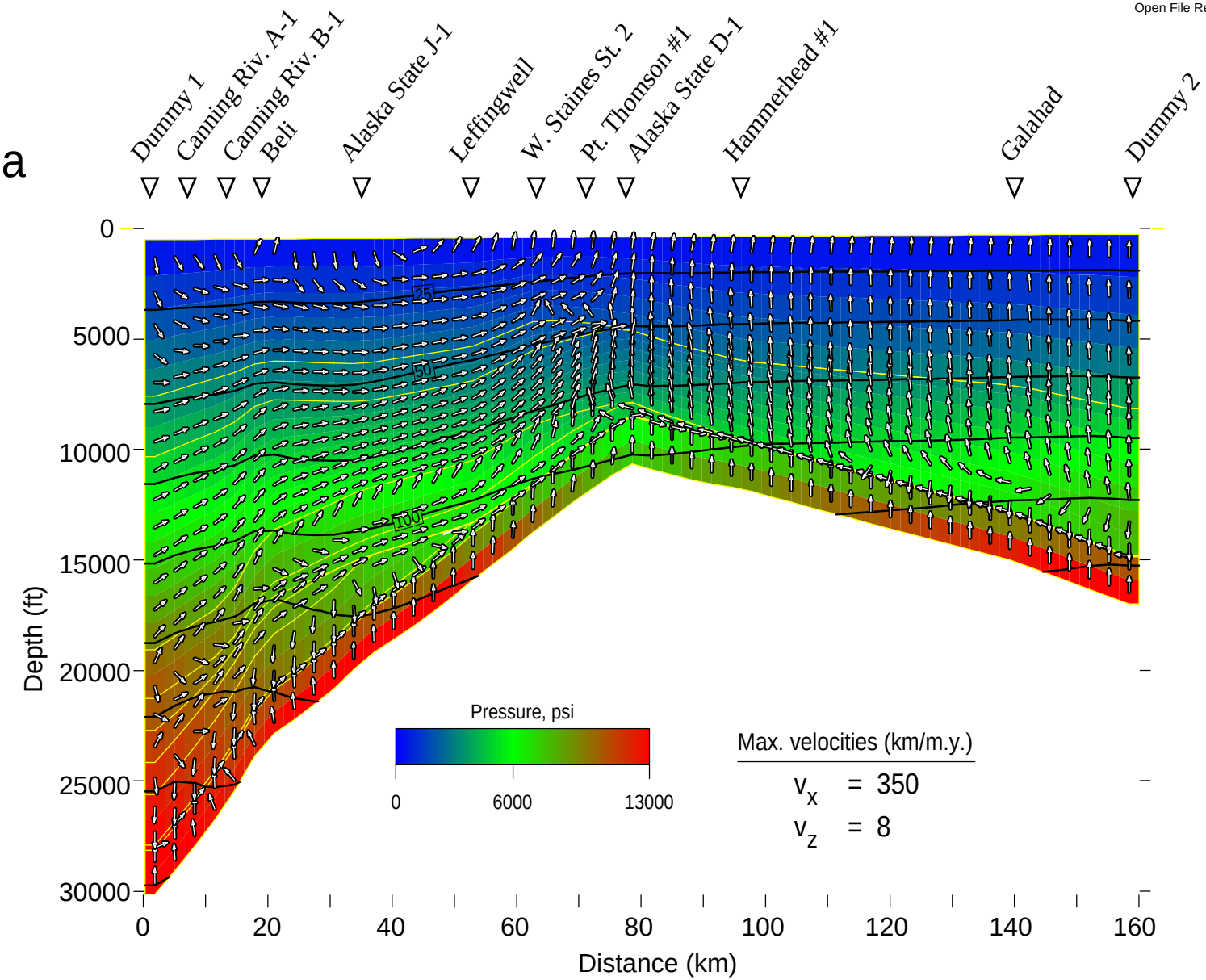

Figure FF11b. Simulation results at 37 Ma showing fluid flow directions, and pressure and temperature distributions. Flow vectors show direction only and do not imply magnitude. Maximum flow velocities are for comparison with other time slices. Pressure distribution is shown by color scale and temperatures are contoured at 25 °C intervals. Yellow lines show time-stratigraphic units (see Fig. FF2).

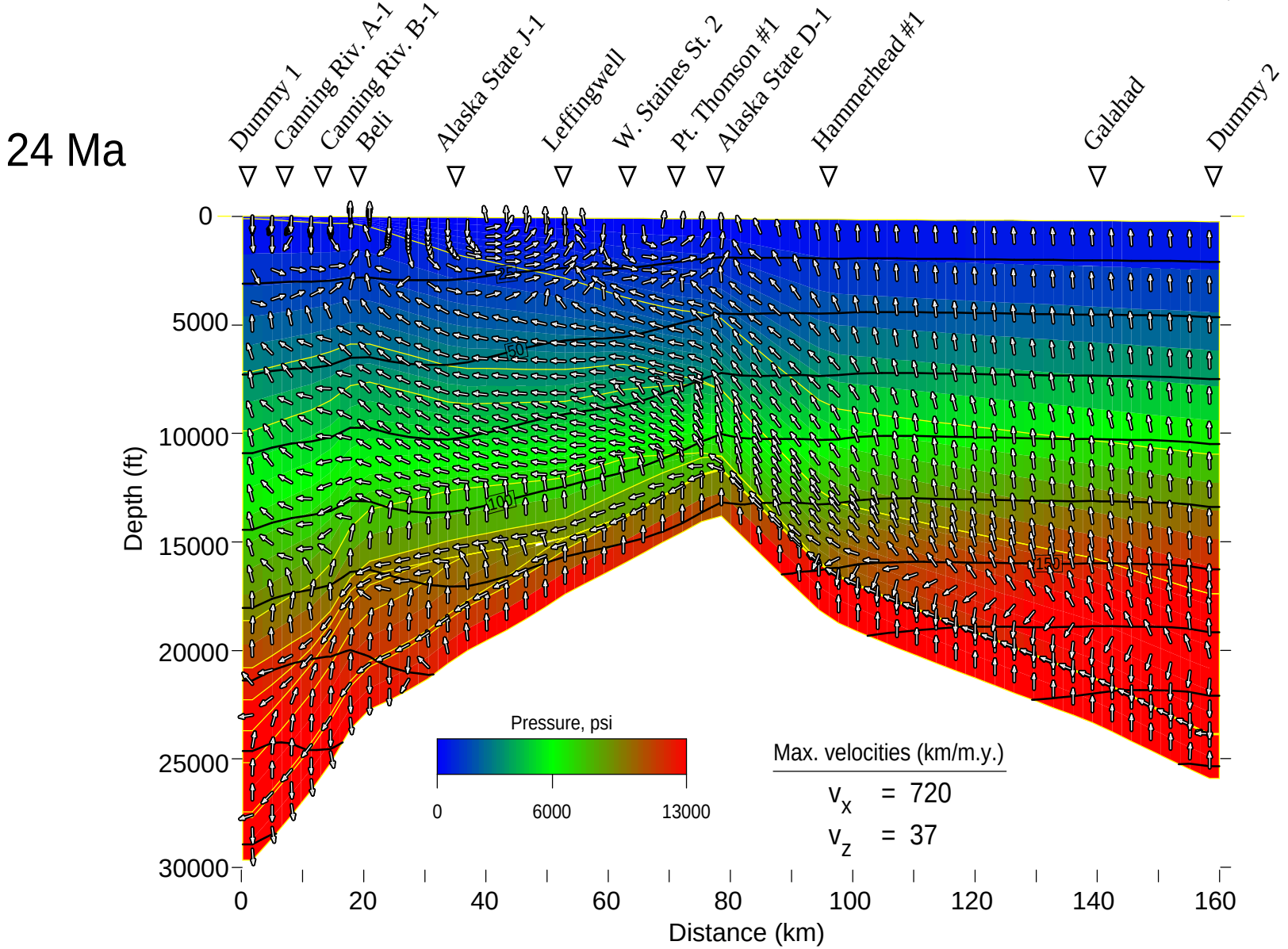

Figure FF11c. Simulation results at 24 Ma showing fluid flow directions, and pressure and temperature distributions. Flow vectors show direction only and do not imply magnitude. Maximum flow velocities are for comparison with other time slices. Pressure distribution is shown by color scale and temperatures are contoured at 25 ℃ intervals. Yellow lines show time-stratigraphic units (see Fig. FF2).

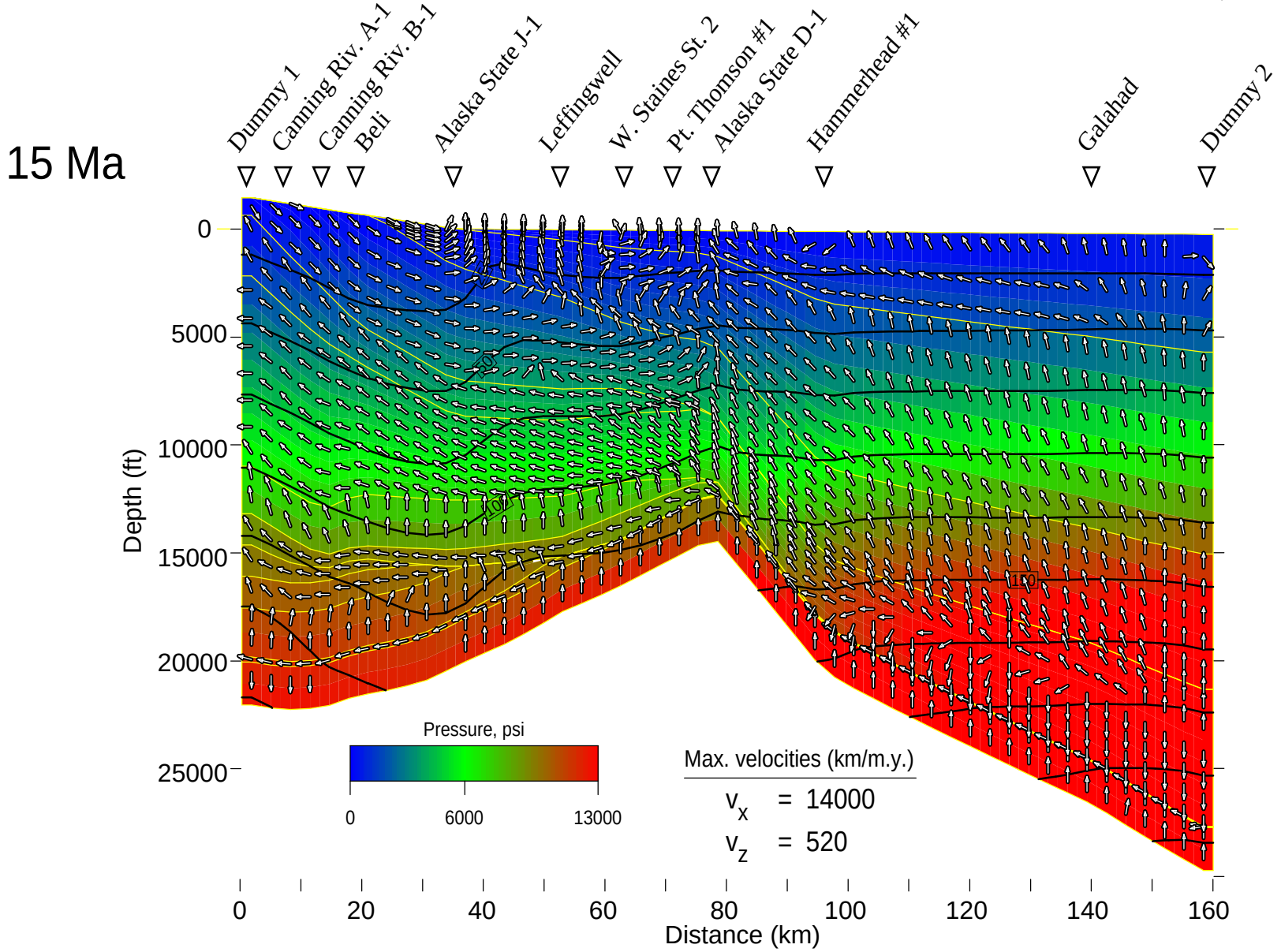

Figure FF11d. Simulation results at 15 Ma showing fluid flow directions, and pressure and temperature distributions. Flow vectors show direction only and do not imply magnitude. Maximum flow velocities are for comparison with other time slices. Pressure distribution is shown by color scale and temperatures are contoured at 25 °C intervals. Yellow lines show time-stratigraphic units (see Fig. FF2).

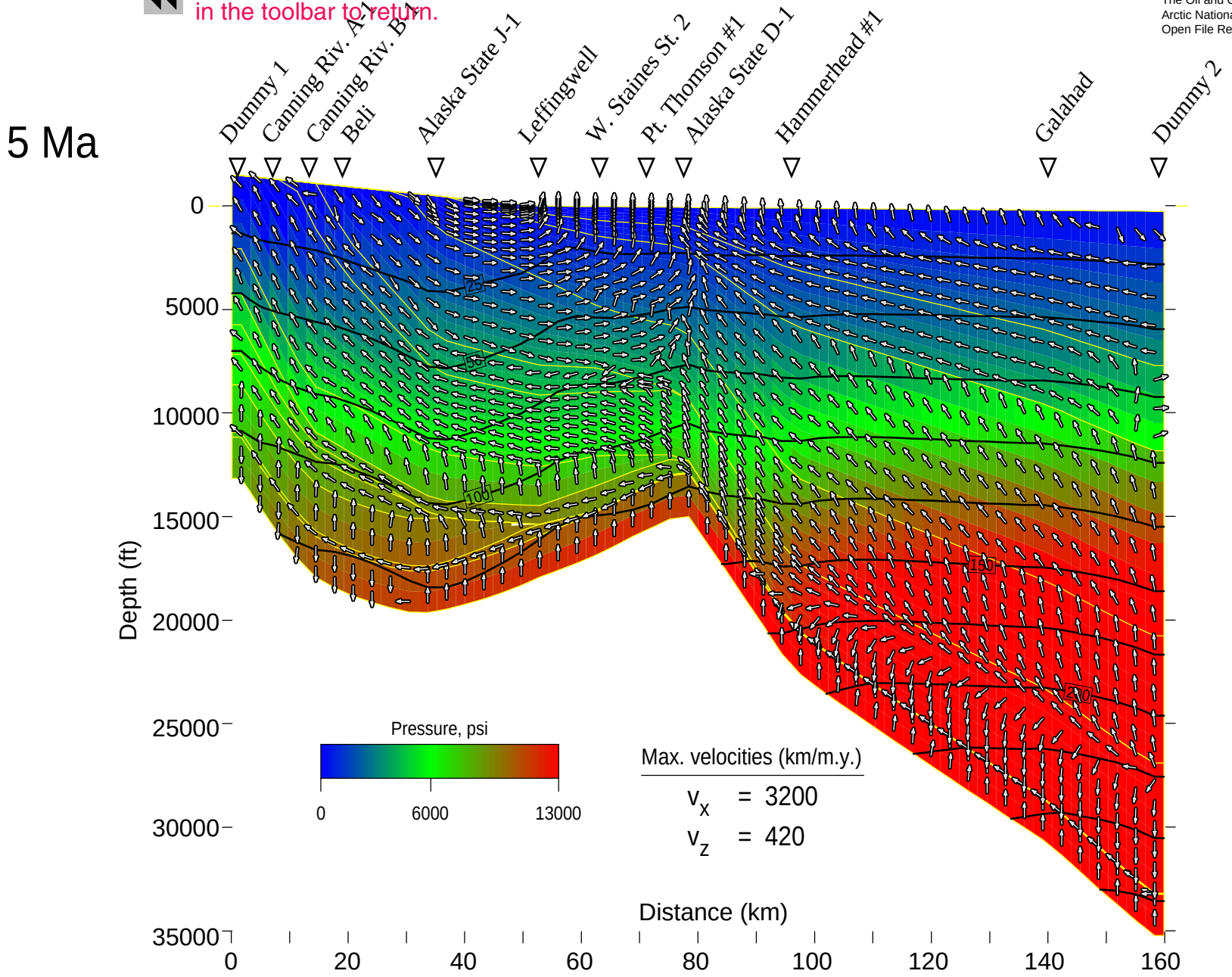

Figure FF11e. Simulation results at 5 Ma showing fluid flow directions, and pressure and temperature distributions. Flow vectors show direction only and do not imply magnitude. Maximum flow velocities are for comparison with other time slices. Pressure distribution is shown by color scale and temperatures are contoured at 25 °C intervals. Yellow lines show time-stratigraphic units (see Fig. FF2).

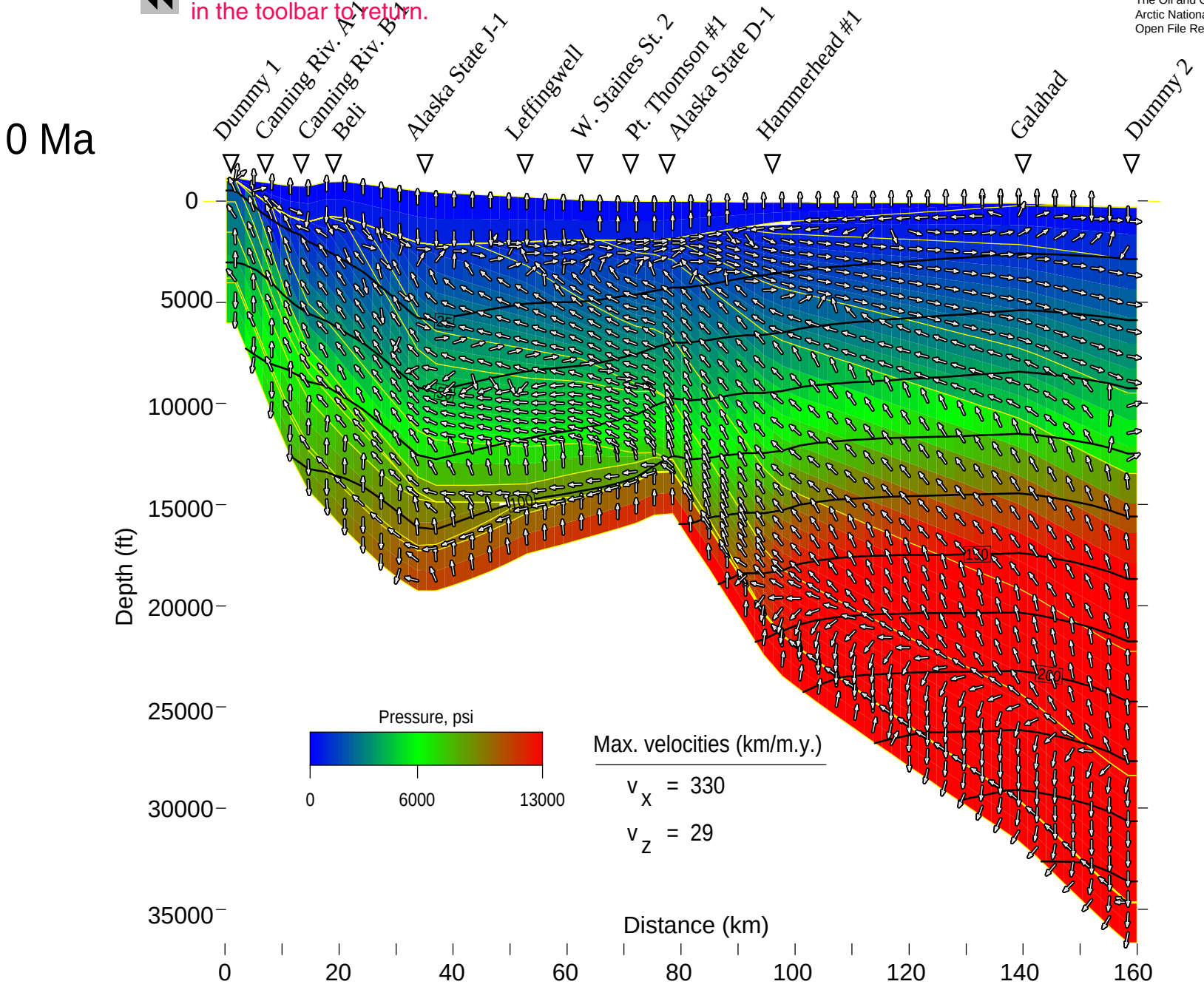

Figure FF11f. Simulation results at 0 Ma showing fluid flow directions, and pressure and temperature distributions. Flow vectors show direction only and do not imply magnitude. Maximum flow velocities are for comparison with other time slices. Pressure distribution is shown by color scale and temperatures are contoured at 25 °C intervals. Yellow lines show time-stratigraphic units (see Fig. FF2).

Click here or on this symbol
in the toolbar to return.

Table FF1. Correlations used in hydrologic models to calculate porosity, permeability, and thermal conductivity.

	Porosity[a] (ϕ)				Permeability[b] (k)				Thermal Conductivity[c] (K)	
	ϕ_0	ϕ_1	b	b_{ul}	A	B	k_x/k_z	max	A	B
Sandstone	0.49	0	0.35	0.07	23	-4.5	2.5	1	-1.8	3.3
Shale	0.50	0	0.80	0.16	18	-9	10	1	-1.46	1.76
Carbonate	0.35	0	0.55	0.06	22	-7	2.5	1	-2.64	3.05
Endicott	0.43	0	0.35	0.04	26	-4.5	10	1	-2.72	3.14
Basement	0.20	0	0.50	0.05	0	-9	10	-9	-1.88	2.3
Permafrost	0.46	0	0.0	0.0	0	-18	10	-18	0	2000

[a] $\phi = \phi_0 \exp(-bZ_E) + \phi_1$, expressed as a fraction; b is the compaction coefficient (km^{-1}); Z_E is effective burial depth (km); b_{ul} is the unloading coefficient which determines the rebound of porosity (see Bethke and others, 1993).

[b] $\log k_x = A\phi + B$, expressed as μm^2; 1 $\mu m^2 \approx 1$ darcy; k_x/k_z is lateral/vertical permeability ratio; max is maximum permeability (maximum value allowed for $\log k_x$).

[c] $K = A\phi + B$, expressed as W/m °C.

Table FF2. Formation Thicknesses. Depositional values (shown in black) refer to present-day thicknesses for existing formations. For sediments later removed by erosion, values refer to compacted thicknesses. Erosional values (shown in red) indicate thickness of sediments removed at time of erosion. Because sediment regains a portion of its porosity lost during compaction, the "eroded thickness" of a unit completely removed is greater than its depositional "compacted thickness". Thickness values for each well are in feet, ages are Ma at the end of the depositional/erosional period. "Seq." refers to the depositional sequences defined by Houseknecht and Schenk (Chap. BS). "Dum 1" and "Dum 2" are the dummy wells used to define the ends of the Basin2 model. The full names of the other wells are listed in the text and their locations are shown on Figure FF1.

#	Period/Formation	Seq.	Age	Dum 1	A-1	B-1	Beli	J-1	Leff	W.St.-2	Pt.T-1	D-1	Ham-1	Galahad	Dum 2
19	Present		0	0	1,000	1,805	1,680	2,670	2,218	2,008	1,955	1,900	1,000	100	0
18	Permafrost (begin.)		0.95	0	-1,000	-1,805	-1,680	-2,670	-2,218	-2,008	-1,955	-1,900	-1,000	-100	0
17	Pliocene		1	-7,600	-6,100	-4,300	-3,000	-100	-100	200	900	900	1,500	2,000	2,500
16	U. Miocene	A-up	5	-9,400	-7,000	-4,500	-2,900	-100	350	650	700	800	2,500	5,000	6,500
15	Mid. Miocene	A-low	15	-6,800	-4,800	-2,800	-700	0	450	750	800	900	2,500	3,300	4,000
14	Oligocene	B	24	100	200	300	300	1,700	2,500	3,200	3,500	3,600	7,000	8,000	8,500
13	Eocene	C	37	6,800	6,300	5,800	5,200	5,000	4,000	2,800	2,800	3,000	4,000	5,000	6,000
12	Eocene unconform.		53	0	0	0	0	-58	-122	-160	-600	-900	-1,000	-1,200	-1,200
11	U. Paleocene	D	54	2,700	2,500	2,300	1,700	1,650	1,500	1,200	800	600	200	0	0
10	L. Paleocene	E	59	8,800	8,300	7,800	6,000	3,800	3,400	3,000	3,000	3,000	3,600	6,000	7,000
9	BTU		65	0	0	-150	-200	-250	-300	-400	-500	-700	-800	-800	-800
8	U. Cretaceous	F	66	2,200	2,200	2,230	2,500	2,400	2,000	1,600	800	600	300	300	300
7	Hue, Pebble Kemik	G	74	1,500	1,255	620	601	791	892	1,170	885	600	500	500	500
6	LCU		130	0	0	-680	-720	-2,040	-4,700	-5,150	-5,150	-5,150	-5,150	-5,150	-5,150
5	Kingak		134	1,500	1,000	1,000	1,000	1,000	1,000	1,000	1,000	1,000	1,000	1,000	1,000
4	Sadl+Shublik+Sag		187	1,500	1,400	1,315	1,277	1,000	1,000	1,000	1,000	1,000	1,000	1,000	1,000
3	Lisburne		275	2,300	2,300	2,300	2,300	2,300	2,300	2,300	2,300	2,300	2,300	2,300	2,300
2	Endicott		333	250	250	250	250	250	700	700	700	700	700	700	700
1	pre-Miss		355	2,000	2,000	2,000	2,000	2,000	2,000	2,000	2,000	2,000	2,000	2,000	2,000

Table FF3. Surface Temperatures and Water Depths. Surface temperatures (in °C) indicate the temperature at the end of the time interval. Temperatures grade linearly from the end of one period to the end of the next. The asterix (*) indicates that surface temperatures for the first 3 wells is 20 °C and 10 °C for Beli, as described in text. For water depths, positive values indicate depth of water, negative values (red) indicate the elevation of topography. Water depth values for each well are in feet, ages are Ma at the end of the depositional/erosional period. Sequences (Seq.) refer to the depositional sequences defined by Houseknecht and Schenk (Chap. BS).

Period/Formation	Seq.	Age	°C	Dum 1	A-1	B-1	Beli	J-1	Leff	W.Stn-2	Pt.T-1	D-1	Ham-1	Galahad	Dum 2
Present		0	0.5*	-1,200	-925	-700	-1,052	-475	-205	-65	-5	0	50	100	300
Permafrost (begin.)		0.95	0.5*	-1,200	-925	-700	-1,052	-475	-205	-65	-5	0	50	100	300
Pliocene		1	0.5	-1,200	-1,084	-962	-852	-543	-203	0	21	37	86	200	250
U. Miocene	A-up	5	1	-1,500	-1,325	-1,142	-977	-511	0	25	43	58	102	205	250
Mid. Miocene	A-low	15	5	-1,500	-1,235	-957	-706	0	35	57	73	86	123	212	250
Oligocene	B	24	5	0	10	19	29	54	82	98	111	121	150	220	250
Eocene	C	37	5	500	490	481	471	446	418	402	389	379	350	280	250
Eocene unconform.		53	10	0	0	0	0	0	0	0	0	0	0	0	0
U. Paleocene	D	54	10	250	250	250	250	250	250	250	250	250	250	250	250
L. Paleocene	E	59	10	500	500	500	500	500	500	500	500	500	500	500	500
BTU		65	10	1,000	1,000	1,000	1,000	1,000	1,000	1,000	1,000	1,000	1,000	1,000	1,000
U. Cretaceous	F	66	10	1,800	1,721	1,639	1,565	1,356	1,125	988	884	800	800	800	800
Hue, Pebble Kemik	G	74	10	1,500	1,422	1,339	1,265	1,055	825	688	584	500	500	500	500
LCU		130	10	0	0	0	0	0	0	0	0	0	0	0	0
Kingak		134	12	500	500	500	500	500	500	500	500	500	500	500	500
Sadl+Shublik+Sag		187	20	100	100	100	100	100	100	100	100	100	100	100	100
Lisburne		275	20	100	100	100	100	100	100	100	100	100	100	100	100
Endicott		333	20	100	100	100	100	100	100	100	100	100	100	100	100
pre-Miss		355	20	0	0	0	0	0	0	0	0	0	0	0	0

Click here or on this symbol
in the toolbar to return.

Table FF4. Lithologic composition in terms of the proportions of the end-member rock-types, sandstone (ss), shale (sh) and carbonate (cn), present in each well for each formation. Values estimated from well logs (primarily by Huffman, written commun., 1997). Permafrost* and Basement* indicate special rock types defined for Basin2. Blanks indicate periods of erosion or non-deposition. Sequences (Seq.) refer to the depositional sequences defined by Houseknecht and Schenk (Chap. BS).

Period/Formation	Seq.	Dum 1			A-1			B-1			Beli			J-1			Leff			W.Stn-2			Pt.T-1			D-1			Hamhd-1			Galahad			Dum 2		
		ss	sh	cn	ss	sh	cn	ss	sh	cn	ss	sh	cn	ss	sh	cn	ss	sh	cn	ss	sh	cn	ss	sh	cn	ss	sh	cn	ss	sh	cn	ss	sh	cn	ss	sh	cn
Present					Permafrost*			Permafrost*			Permafrost*			Permafrost*			Permafrost*			Permafrost*			Permafrost*			Permafrost*			Permafrost*			Permafrost*					
Permafrost (begin.)																																					
Pliocene																				.50	.50		.50	.50		.40	.60		.40	.60		.40	.60		.40	.60	
U. Miocene	A-up																.75	.25		.60	.40		.45	.55		.50	.50		.40	.60		.40	.60		.40	.60	
Mid. Miocene	A-lw													.75	.25		.75	.25		.60	.40		.45	.55		.50	.50		.45	.55		.30	.70		.20	.80	
Oligocene	B	.95	.05		.95	.05		.95	.05		.95	.05		.90	.10		.65	.35		.70	.30		.50	.50		.40	.60		.20	.80		.20	.80		.15	.85	
Eocene	C	.90	.10		.90	.10		.90	.10		.90	.10		.90	.10		.65	.35		.55	.45		.35	.65		.25	.75		.15	.85		.10	.90		.05	.95	
Eocene unconform.																																					
U. Paleocene	D	.50	.50		.50	.50		.50	.50		.50	.50		.55	.45		.45	.55		.35	.65		.25	.75		.20	.80		.15	.85		.10	.90		.05	.95	
L. Paleocene	E	.40	.60		.40	.60		.40	.60		.50	.50		.55	.45		.45	.55		.35	.65		.25	.75		.20	.80		.15	.85		.10	.90		.05	.95	
BTU																																					
U. Cretaceous	F	.30	.70		.30	.70		.40	.60		.30	.70		.25	.75		.20	.80		.20	.80		.20	.80		.20	.80		.20	.80		.20	.80		.20	.80	
Hue, Pebble Kei	G	.05	.95		.05	.95		.05	.95		.10	.90		.17	.83		.25	.75		.40	.60		.60	.40		.40	.60		.20	.80		.20	.80		.20	.80	
LCU																																					
Kingak		.10	.90		.10	.90		.10	.90		.15	.85		.15	.85		.15	.85		.15	.85		.15	.85		.15	.85		.15	.85		.15	.85		.15	.85	
Sadl+Shublik+Sag		.35	.55	.10	.35	.55	.10	.40	.40	.20	.60	.40		.60	.40		.60	.40		.60	.40		.60	.40		.60	.40		.60	.40		.60	.40		.60	.40	
Lisburne			.05	.95		.05	.95		.05	.95		.05	.95		.05	.95		.05	.95		.05	.95		.05	.95		.05	.95		.05	.95		.05	.95		.05	.95
Endicott		.10	.85	.05	.10	.85	.05	.10	.85	.05	.10	.85	.05	.10	.85	.05	.10	.85	.05	.10	.85	.05	.10	.85	.05	.10	.85	.05	.10	.85	.05	.10	.85	.05	.10	.85	.05
pre-Miss		Basement*			Basement*			Basement*			Basement*			Basement*			Basement*			Basement*			Basement*			Basement*			Basement*			Basement*			Basement*		

Table FF5. Typical values of thermal conductivity for different lithologies and values for NPRA geologic units compared to calculated results from the Basin2 model. All values are in W / m K.

Lithology	*In Situ* Conductivity Typical Range of Values[1]		Basin2 values[2] as f(porosity)	
	20 °C	100 °C	40 %	5 %
claystone and siltstone	0.80 - 1.25	1.0 - 1.5		
shale	1.05 - 1.45	1.2 - 1.7	1.2	1.7
sandstone	2.50 - 4.20	2.0 - 3.2	2.58	3.2
limestone	2.50 - 3.10	2.2 - 2.8	2.1	2.8

Time-Strat. or Geologic Unit	NPRA Matrix Conductivities measured[3]	NPRA *In Situ* Conductivities estimated[3]	NPRA *In Situ* Conductivities approx.[4]	Basin2 values[5] min	Basin2 values[5] max
Brookian					
Pliocene				1.4	1.4
Miocene				1.6	2.0
Oligocene				1.6	2.0
Eocene				1.9	2.2
L. Paleocene				1.6	2.1
Paleocene				1.4	2.3
L. Cretaceous				1.8	2.0
Colville	2.31		2.1		
Nanushuk	1.75		1.7		
Torok	1.80	1.7			
Pebble shale[6]	1.62		1.6	1.7	2.0
Ellesmerian					
Kuparuk	2.50		2.2		
Kingak	2.17		2.0	1.8	1.9
Sag River[6]	4.13		3.1		
Shublik[6]	2.61		2.3	2.1	2.2
Sadlerochit[6]	2.95		2.5		
Lisburne	3.71	2.9		2.0	2.9
Endicott	4.55		3.2	3.0	3.1
Pre-Mississippian					
Basement (Argillite)	2.73		2.4	1.5	2.2

[1] *In situ* values reported by Blackwell and Steele (1989) for different lithologies at 20 °C. We modified these values for temperature effects (100 °C) as summarized by Robertson (1979).

[2] Basin2 values calculated directly from porosity-thermal conductivity functions listed in Table FF1.

See next page for more:

Click here or on this symbol in the toolbar to return.

[3] Measured matrix conductivities average values and *in situ* conductivities were estimated from equilibrium temperature logs and matrix conductivities (Deming and others, 1992).

[4] We calculated "approximate" *in situ* conductivities by decreasing measured matrix conductivities proportionally to the differences between measured matrix and estimated *in situ* conductivities reported by Deming and others (1992).

[5] Basin2 results at 0 Ma. Calculations use the depth-porosity and porosity-thermal conductivity functions listed in Table FF1 for the rock-types listed in Table FF4.

[6] The Hue, Pebble, and Kemik units are lumped together in the Basin2 model as are the Sag River, Shublik and Sadlerochit units.

Click here or on this symbol in the toolbar to return.

Table FF6. Summary of hydrocarbon generation kinetic constants for the 1002 area.

Unit	Oil Type	Petroleum System	E_A (kJ/mol)	A_o (1/m.y.)	Ref.
Mikkelsen Tongue	Manning	Canning-Sag.	230.0	3.974E+27	1
Hue Shale	Jago	Hue-Thomson	221.249	1.035E+27	2
Shubik Formation	Prudhoe	Ellesmerian	224.208	1.790E+27	2

1) Issler and Snowdon (1990), data on Beaufort-Mackenzie basin oils
2) Lillis and others (Chap. OA)

Click here or on this symbol in the toolbar to return.